Development of a laser Doppler velocimeter for plastic deformation monitoring

INEGI – Institute of Mechanical Engineering and Industrial Management

Ana Sofia de Freitas Alves

Final Project / MIEM Dissertation

FEUP Coordinator: Professora Doutora Ana Rosanete Lourenço Reis

INEGI Coordinator: Doutor Paulo José da Silva Tavares

INEGI Coordinator: Doutor Pedro Manuel Cardoso Teixeira

Faculdade de Engenharia da Universidade do Porto

Mestrado Integrado em Engenharia Mecânica

June 2014

ABSTRACT

With the emergence of new high speed forming techniques such as electromagnetic, electrohydraulic or explosive forming the need arose to characterize materials for high speed deformation in anticipation of an appreciable difference for properties in plastic deformation in such schemes. The theme for this thesis arose from the scope of a FCT project to study the velocity of high speed forming and trying to establish a relation between the velocity and the deformation capacity of material, enabling the characterization of the materials.

This thesis has as main objective the development of a Doppler Effect velocimeter to subsequently measure the deformation velocities on expansion test by magnetic impulse.

Throughout this work there was the need to study several interferometry techniques in order to better understand the equipment and mastering the field of optical metrology as it relates to the topic of thesis. As such two different interferometers were assembled: a Mach-Zehnder and a Michelson. It was developed a Laser Doppler Velocimeter (LDV) based on Michelson Interferometer and it was possible to measure velocities in the range of mm/s. It was also initiated the project to develop and implement a Photon Doppler Velocimeter (PDV) capable of measuring velocities of several km/s. This PDV was dimensioned in Optics and Experimental Mechanics Laboratory firstly to a Hopkinson bar because this is the only equipment available in LOME capable of reaching velocities of m/s, in this case 5 to 15 m/s approximately.

As a result of this work, a LDV was developed and it is being used in LOME to monitor the objects movement, a PDV that is partially complete but already utilized to measure velocities and a portable LDV with relatively adaptation and portability characteristics that the laboratory may now materialize.

Keywords: Doppler Effect, Photon Doppler Velocimeter, Laser Doppler Velocimeter, magnetic impulse, Split Hopkinson Pressure Bar, interferometry, optical metrology.

RESUMO

Com o aparecimento de novas técnicas de conformação plástica a altas velocidades, tais como conformação plástica por impulso magnético, *electro-hydraulic forming* ou por explosão, surgiu a necessidade de caracterizar os materiais para deformações a altas velocidades antecipando-se uma diferença apreciável nas propriedades de deformação plástica nesses regimes. O tema para esta tese surgiu do âmbito de um projeto FCT para estudar a velocidade da conformação plástica a alta velocidade e tentar estabelecer uma relação entre a velocidade e a capacidade de deformação do material, caracterizando deste modo os materiais.

Esta tese tem como objectivo principal o desenvolvimento de um velocímetro por efeito de Doppler para posteriormente medir as velocidades de deformação em ensaios de expansão por impulso magnético.

Ao longo deste trabalho houve a necessidade de estudar várias técnicas de interferometria de modo a conhecer o equipamento e o domínio da metrologia óptica tal como se relaciona com o tema da tese. Como tal foram montados dois interferómetros diferentes: um Mach-Zehnder e um Michelson. Foi desenvolvido um Velocímetro Doppler por laser (LDV) com base no interferómetro de Michelson e com ele foi possível medir velocidades da ordem dos mm/s. Foi igualmente iniciado o projeto de desenvolvimento e implementação de um *Photon Doppler Velocimeter* (PDV) capaz de medir velocidades de vários km/s. Este PDV foi dimensionado no Laboratório de Óptica e Mecânica Experimental inicialmente para uma barra de Hopkinson, pois é o único equipamento existente no LOME capaz de atingir velocidades na ordem dos m/s, no caso entre 5 e 15 m/s aproximadamente.

Como resultado deste trabalho, desenvolveu-se um LDV já utilizado no LOME para monitorizar o movimento de objetos, um PDV, apesar de que ainda parcialmente completo apenas e que foi já utilizado para medir velocidades e um protótipo para um LDV portátil com características de relativa adaptação e portabilidade que o laboratório poderá agora concretizar.

Palavras-chave: Efeito de Doppler, *Photon Doppler Velocimeter*, Velocímetro Doppler por laser, impulso magnético, *Split Hopkinson Pressure Bar*, interferometria, metrologia óptica.

ACKNOWLEDGEMENTS

In the first place I would like to thank to coordinator from Faculty of Engineering of the University of Porto, Professor Ana Rosanete Reis for the encouragement and the opportunity to make this thesis in INEGI – LOME.

A very special thank you to Doctor Paulo Tavares, my coordinator in LOME, for his support, valuable advices, highest professionalism and human qualities that have set a precious example, which I follow, and I aspire to attain someday.

Also to my coordinator Doctor Pedro Teixeira I would like to thank for the availability and useful advices.

To Professor Mário Vaz I would like to thank the opportunity to make this project in Optics and Experimental Mechanics Laboratory and for all the precious ideas throughout this work.

I would like to thank my colleague André Ferreira for all the help, availability and friendship throughout this thesis. To Nuno Viriato I am grateful for all its availability and the help given so much in the experimental part as in the project part and for all his sympathy and friendship. Finally I would also like to thank Professor Luis Morão for help in deciding the subject of the thesis, the guidance given during the thesis and throughout my academic career.

To Professor Geoffrey Taber, from Ohio State University, a special thanks for all the help on developing the PDV and for all the advice given during this thesis.

A special thanks for all my colleagues at LOME, who have indeed been very supportive. In particular to Ricardo Teixeira, Frederico Gomes and Paulo Pereira who have helped in different ways, and to all those weren't directly involved but had to withstand my enthusiasm doubts anyway.

Last, but in no way least important, my family and friends, always behind me and so supportive during this project, I thank you all for all the help, care and concern.

Contents

LIST OF FIGURES

LIST OF TABLES

LIST OF GRAPHICS

LIST OF ABBREVIATIONS

AOM	Acousto-Optic Modulator
BS	Beamsplitter
CSV	Common Separated Values
CW	Continuous wave
EDFA	Erbium Doped Fiber Amplifier
EMF	Electromagnetic Forming
FCT	Foundation for Science and Technology
FFT	Fast Fourier Transform;
FLC	Forming Limit Curve
LDV	Laser Doppler Velocimetry;
LLNL	Lawrence Livermore National Laboratory
LOME	Optics and Experimental Mechanics Laboratory;
M	Mirror
PD	Photo detector
PDV	Photon Doppler Velocimetry
SHPB	Split Hopkinson Pressure Bar
STFT	Short Time Fourier Transform
VISAR	Velocity Interferometer System for Any Reflector

1 INTRODUCTION

1.1 Motivation

Metal forming is a metalworking process of forming metal parts and objects through mechanical deformation. In these processes the workpiece is reshaped without adding or removing material. Forming operates on the principle of plastic deformation of each material where the physical shape of a material is permanently deformed. This process is used in various applications like automobiles, domestic appliances, aircraft, food and drink cans and also a host of other familiar products. The sheet metal parts have the advantage that the material has a high elastic modulus and high yield strength so that the parts produced can be stiff and have a good strength-to-weight ratio.

The conventional sheet metal forming process usually consists of a force that is applied into the sheet against a die, with a determinate shape. There are various different operations using sheet metal forming, such as, blanking and piercing, bending, stretching, hole extrusion, stamping or draw die forming, deep drawing, among others.

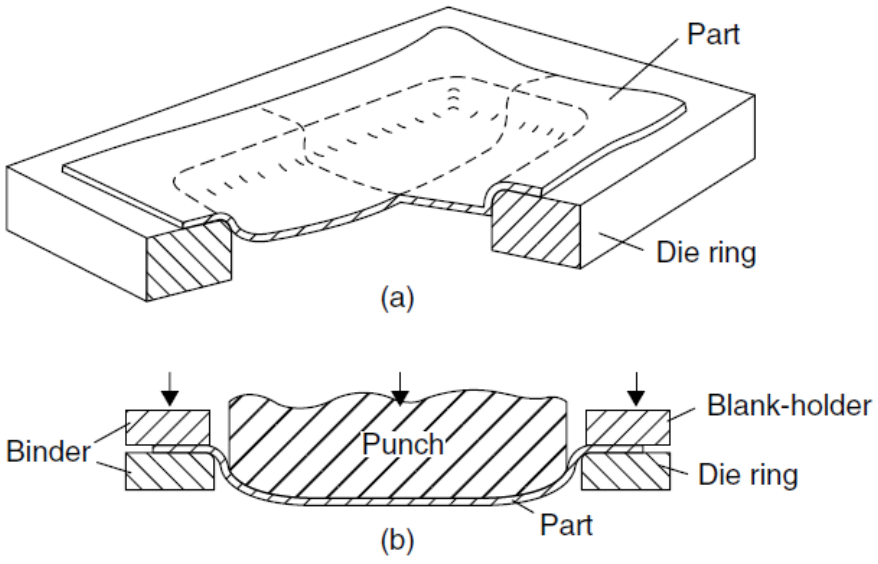

Figure 1.1 – (a) Typical part formed in a stamping or draw die with the die ring and without the punch; (b) Section of tooling in a draw die [1]

In sheet metal forming there are two regimes of interest, concerning the properties of the material: elastic and plastic deformation. For the conventional sheet metal forming, these mechanical characteristics are well known due to the characterization of the materials commonly used in metal forming.

The formability is limited, in most of the sheet metals, by the occurrence of localized necking. In order to better understand the formability of each sheet metal Keeler and Backofen [2] reported that during sheet stretching, the onset of localized necking required a critical combination of major and minor strains. Consequently this concept was extended to drawing deformations by Goodwin [2] and the resulting curve in principal strain space is known as the forming limit curve (FLC).

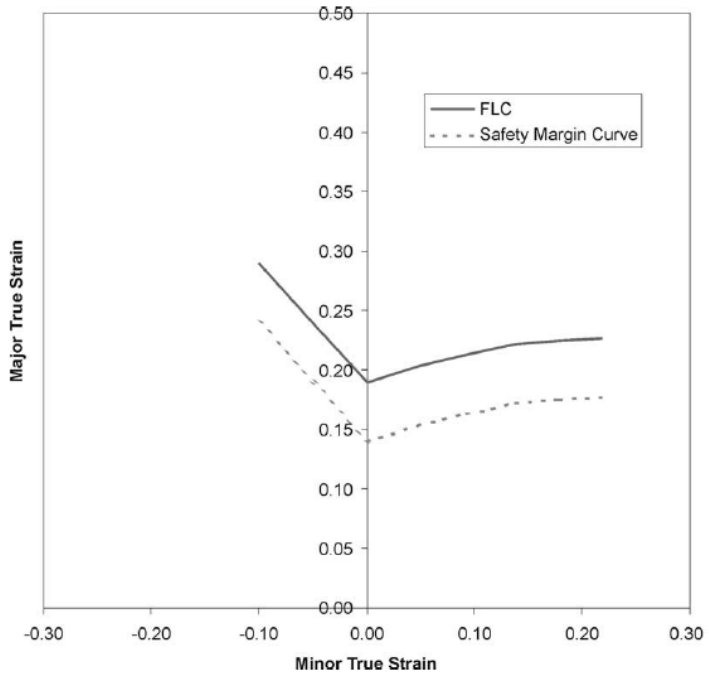

Figure 1.2 – Example of a FLC for aluminum [3]

These kinds of diagrams are usually obtained experimentally by stretching sheet metal samples over a hemispherical punch. The principal strains are measured with the help of a regular or circular grid that is electro-etched or printed onto the un-deformed blank, where the greater of the two principal strains it is always positive, while the minor strain can be either negative or positive depending on the mode of deformation. The left side of the FLC corresponds to a uniaxial tension and the right side of the FLC is referred to biaxial tension therefore, the usual tests made to obtain the FLC are tensile tests for uniaxial tension and Bulge-test or Nakajima for biaxial tension, among others.

In the automotive industry, environmental and economic matters have become some of the most significant topics. The need of pollution reduction and costs saving, along with the increase of the demands in performance, luxury and safety, is leading to the development of lightweight and more energy efficient vehicles.

Due to the application of new materials in the production of high performance complex shapes and also the requirement of high production rates and more efficient manufacturing, new technological processes have been developed. These new manufacturing methods are characterized by high speed forming techniques such as explosive, electromagnetic or electrohydraulic forming with a range of strain rates 10^2 to 10^4 s^{-1}. As a result, along with the change of the behavior of materials at high strain rates, the need has emerged to once more characterize new features of the materials.

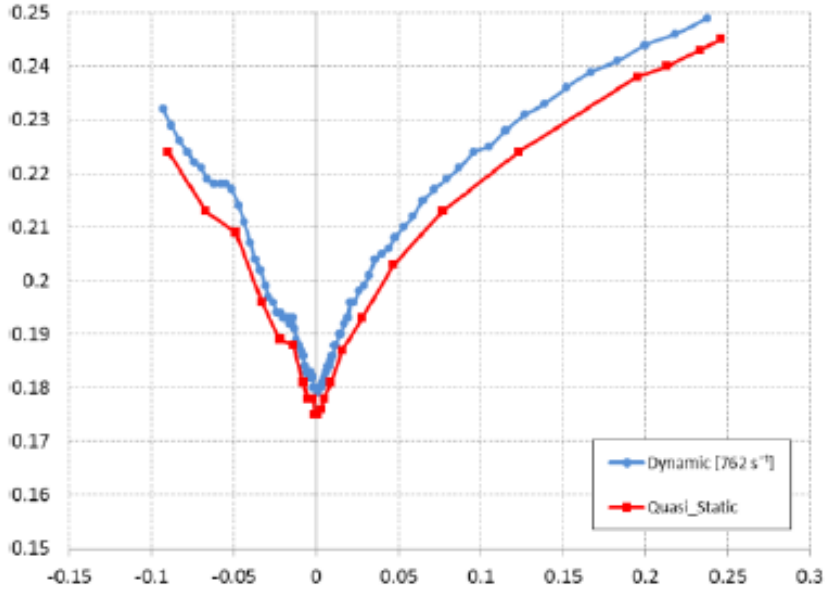

Figure 1.3 – Quasi-static and dynamic forming limit curves [4]

In order to characterize the materials for high speed forming usually two kinds of tensile tests can be done, tensile test in the Split Hopkinson Pressure Bar (SHPB) where the velocity of the test can go up to 15 ms^{-1} and expansion ring test in the electromagnetic forming (EMF) machine, where velocities can go up to 300 ms^{-1}. Since these tests can reach high velocities comparing to the quasi-static tests, usually under 1 ms^{-1}, it is difficult to observe the deformation along the test. As such, the alternative is to measure the velocity that the specimen is subjected to during the test. Therefore, the most influent laboratories in this field started to use a new equipment known as Photon Doppler Velocimeter (PDV), to measure such high deformation velocities during the tests.

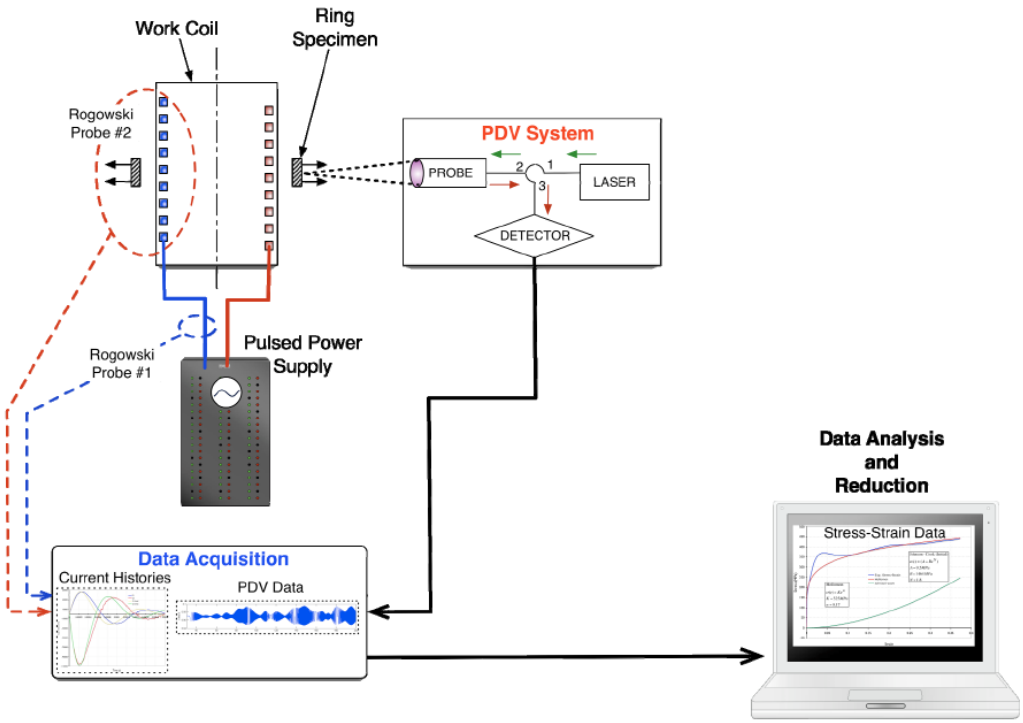

Figure 1.4 – Scheme of dynamic ring expansion test to measure tensile stress-strain relations at high strain rate [5]

Although the Hopkinson bar method is the dominant approach to characterize materials, it is a difficult method to run in true uniaxial tension and the process of testing and data analysis is rather time consuming. Moreover, as there are no standards in Hopkinson bar testing, it is difficult to obtain data that is reproducible in detail from one lab to another. Therefore, the electromagnetically driven expanding ring has been proposed as a test for high strain rate tensile testing by Niordson [5]. The basic approach for the experiment is shown in Figure 1.4.

As a result, the need for measuring the velocity during the expanding ring tensile test is a consequence from the necessity to prove the existing relation between the velocity or acceleration and the deformation suffered during the tensile test of the ring.

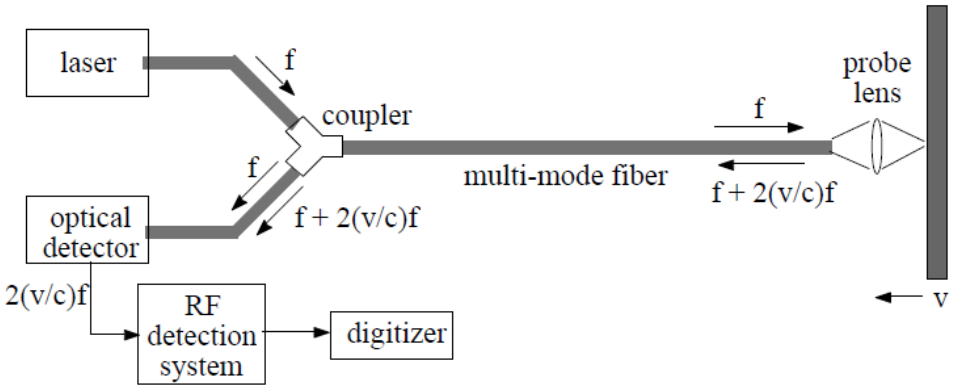

Figure 1.5 – Basic block diagram of the photonic Doppler velocimetry system [6]

PDV was developed in Lawrence Livermore National Laboratory (LLNL) by O. T. Strand [6]. This velocimeter is based in a Laser Doppler Velocimeter (LDV) and along with the development of the telecommunications industry, it was possible to create a relatively cheap velocimeter which is also easy to operate, that can measure from mms^{-1} to kms^{-1}. PDV uses fiber optics technologies and is limited only by the bandwidth of the electrical test components.

As part of a new project by INEGI – CETECOP / LOME, the need arose to develop a PDV to measure velocities of expanding ring tests made in the electromagnetic forming machine in order to characterize the materials AL 6082 T6 and AZ 31 B – H24, aluminum and magnesium alloys respectively. The need to develop the PDV instrument is mostly due to the fact that this is a relatively new technology and therefore only a few laboratories in the world have it. None of these are located in Portugal or anywhere near, therefore preventing the possibility of partnerships between nearby laboratories. This project arises from a FCT project grant: EXPL/EMS-TEC/2419/2013. [1, 2, 4-8]

1.2 INEGI

INEGI (Institute of Mechanical Engineering and Industrial Management) was started in 1986, from the Department of Mechanical Engineering and Industrial Management (DEMEGI) of the Faculty of Engineering of University of Porto and is an interface Institute between University and Industry, oriented to the activities of research and development, innovation and technology transfer. It is considered an active agent playing a significant role in the development of the Portuguese industry, and in the transformation of its competitive model.

The Optics and Experimental Mechanics Laboratory (LOME) is an operational division of INEGI focused on research activities for design, validation and inspection of structures and mechanical components. It is composed by an interdisciplinary group of researchers with expertise in multiple

sensing technologies for structural monitoring, advanced manufacturing processes for metallic structures, structural integrity, multi-body modeling, optics and laser metrology, experimental mechanics, biomechanics, among others. These activities have been conveniently grouped into four distinctive areas: Non-destructive Testive or Inspection (NDT / NDI), experimental Mechanics and New Technologies, Structural Health Monitoring, and, Biomechanics.

1.3 Objectives

The objective of this work was the development and implementation of Laser Doppler Velocimeters and the Photon Doppler Velocimeter and also to develop a LDV to measure low velocities and make a portable prototype to be used in LOME for innumerous applications requiring velocities measurements.

A second objective of the current work was the start of the development of a PDV to be applied in the electromagnetic forming machine, to measure velocities in the expanding ring tests. Since the fastest tensile test machine existing in LOME is the SHPB, it was deemed appropriate to study a way to apply the LDV and the PDV in the SHPB.

1.4 Structure of the thesis

In a way to complete all the proposed objectives, this thesis was divided in 6 chapters. This is the first chapter, the introduction and motivation for this thesis. Chapter 2 presents the theoretical background for the development of PDV. This chapter contains some basic background on Optics and Optical Metrology, all the concepts that made possible the PDV and how the processing data is made. It also presents the diverse applications and also the advantages and disadvantages of the technology.

Chapter 3 and Chapter 4 describe all the work done during the development of a PDV. In Chapter 3 all the experimental work from the development of a LDV through to the first low-velocity measurements with a different LDV setup and to the setup and deployment of a PDV and its application to measurements in the Hopkinson Bar, is described. In Chapter 4 all the performed data analysis is presented both for the LDV and for the PDV and a brief explanation of how the developed Matlab ® program for data analysis works.

Chapter 5 is divided in two sections. The first section refers the foreseen future work, where the work that is likely to be done in the future is described. In the second section, a proposal for a portable LDV prototype is presented.

Finally in Chapter 6, all the conclusions reached throughout the thesis are written.

2 THEORETICAL BACKGROUND

Since the LDV is based in optics and interferometric techniques, there has been the need to study some basics of Optics and Optical Metrology. This chapter explains all the theoretical background needed to understand and develop a LDV and later on, a PDV.

In this chapter, the phenomenon behind the measurement of velocity with these technologies, known as the Doppler Effect, is first explained. Afterwards, there is a summary about the basics of optics, the most commonly used components, some interferometry techniques and the different interferometers used in most optical laboratories. Another technique used in the measurement of velocities is the heterodyne technique, also explained therein.

Finally, the LDV and PDV techniques are covered as well as the data analysis is made and all the mathematics behind the data analysis of the results, such as the Fast Fourier Transform (FFT), an algorithm used in the most daily electronic equipment.

2.1 The Doppler Effect

Although there seems to be no historical account of the popular perception of the effect, it is easy to assume the Doppler Effect had been notice before, probably since antiquity. Johann Christian Doppler proposed in 1846 an explanation to an observable effect where the frequency of waves emitted from a moving object is shifted from the original frequency. Since then, the Doppler shift phenomenon has been realized in many applications extending from weather and aircraft radar systems to the measurement of blood flow in unborn fetal vessels. The Doppler Effect became central to most of the interferometric techniques for measuring velocities.

According to the description of the effect, light shone by an observer against an object moving toward him will be reflected with a higher frequency.

The effect is readily observable irrespective of the movement of either the transmitter or the receiver of the electromagnetic radiation.

Figure 2.1 illustrates the principle of the Doppler Effect.

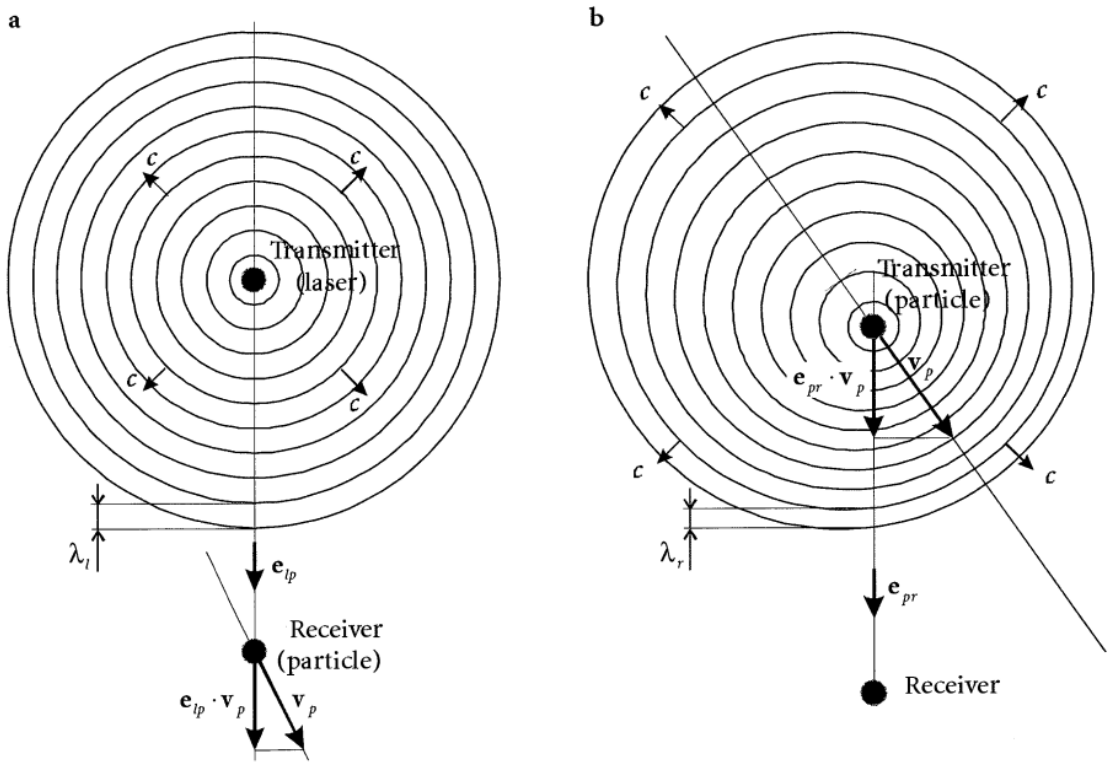

Figure 2.1 – The Doppler effect [9]

An electromagnetic wave originating from a moving transmitter with a velocity v_p and a frequency f_p is apparently compressed for an observer standing in the direction of the movement and apparently expanded in the opposite direction. This results in a change of wavelength or frequency described as,

$$\lambda_r = \lambda_p - \frac{v_p \cdot e_{pr}}{c}\lambda_p, \qquad f_r = \frac{c}{\lambda_r} = \frac{f_p}{1 - \frac{v_p \cdot e_{pr}}{c}} \tag{2.1}$$

The noticed wavelength λ_p and the frequency f_p of a moving receiver with relative velocity v_p with respect to the stationary transmitter is given by

$$\lambda_p = \frac{\lambda_l}{1 - \frac{v_p \cdot e_{lp}}{c}}, \qquad f_p = f_1 - \frac{v_p \cdot e_{lp}}{\lambda_l} \tag{2.2}$$

If the transmitter and the receiver are moving, then the Doppler Effect is invoked twice and the noticed frequency at a stationary receiver for a stationary laser and for light scattered from a moving particle becomes ($|v_p| \ll c$)

$$f_r \approx f_l\left(1-\frac{v_p\cdot(e_{lp}-e_{pr})}{c}\right) \quad \textbf{(2.3)}$$

In other words, the Doppler Effect occurs when a source *S* emits waves at a frequency *v* and wavelength λ to an observer O, the frequency being observed as *f'* and the wavelength as λ' if the source *S'* moves during the transmission.

It is possible to say that the Doppler Effect consists of a change of the observed frequency, although it is, in essence, a relativistic effect, observed by the receiver and not by the source. [9-12]

2.2 Optical Metrology

Optical Metrology is the subject which covers all sort of measurements made with light, regardless of the wavelength. Optical Metrology is usually separated into Radiometry and Photometry, depending on the fact the wavelength being used falls inside the 360 – 830nm limit of the visible part of the electromagnetic spectrum, as established by the International Commission on Illumination .(CIE; Commission Internationale de l'Éclairage).

In the following, a brief introduction to Optics and interferometers is exposed, that enables the readers less acquainted with the subject to follow the work in this thesis, on Laser and Photon Doppler Velocimeters

2.2.1 Optics

Light is one form of electromagnetic radiation, the many categories of which make up the electromagnetic spectrum. Electromagnetic radiation, which transports energy from point to point at the velocity of light, can be described in terms of both *wave* and *particle* "pictures" or "models". This is the famous "wave-particle" duality of all fields or particles in our model of the universe. In the electromagnetic-wave picture, waves are characterized by their frequency *v*, wavelength λ, and the velocity of light *c*, which are related by $c = v\lambda$.

A propagating electromagnetic wave is characterized by a number of field vectors, which vary in time and space.

For a complete description the polarization state of the wave must also be specified. Linearly polarized waves have fixed directions for their field vectors, which do not re-orient themselves as the wave propagates. Circular or elliptically polarized waves have field vectors that trace out circular or elliptic

helical paths as the wave travels along. In the particle counterpart picture, electromagnetic energy is carried from point to point as quantized packets of energy called photons.

Optical materials have refractive indices that vary with wavelength. This phenomenon is called dispersion. It causes a wavelength dependence of the properties of an optical system containing transmissive components. The change of index with wavelength is very gradual, and often negligible, unless the wavelength approaches a region where the material is not transparent. A description of the performance of an optical system is often simplified by assuming that the light is approximately monochromatic, i.e., contains only a small spread of wavelength components. [13]

Reflection and Refraction

The phenomena of reflection and refraction are most easily understood in terms of plane electromagnetic waves – those in which the direction of energy flow is unique.

When light is reflected from a plane mirror, or the planar boundary between two media of different refractive index, the angle of incidence is always equal to the angle of reflection, as shown in Figure 2.2. This is the fundamental law of reflection.

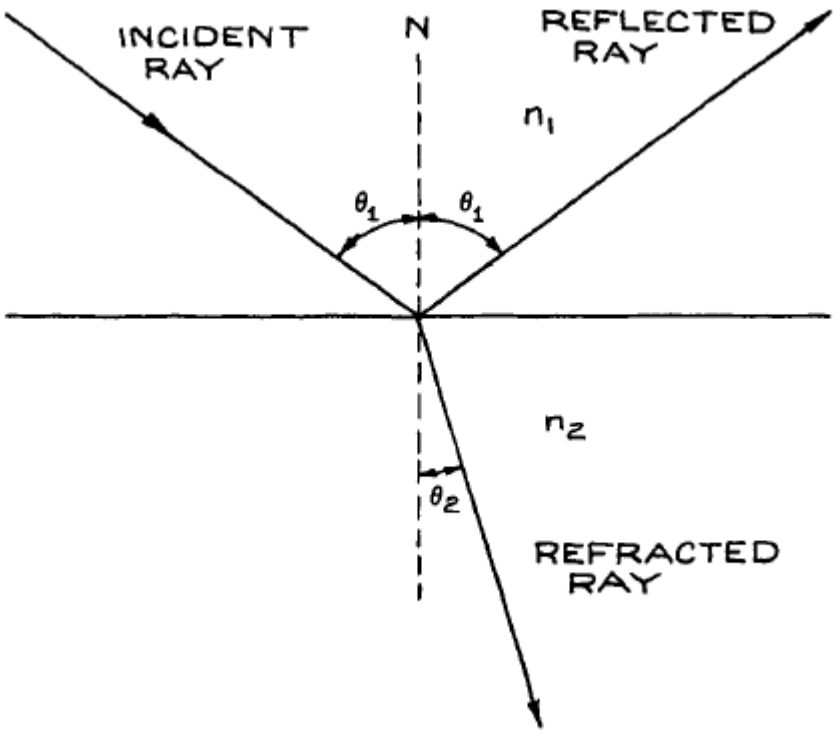

Figure 2.2 – Reflection and refraction of a light ray [13]

For the light ray that crosses the boundary between two media of different refractive indices, the angle of refraction θ_2 is related to the angle of incidence θ_1 by Snell's law:

$$\frac{\sin\theta_1}{\sin\theta_2} = \frac{n_2}{n_1} \tag{2.4}$$

This result is further modified if one or both of the media is anisotropic. [13]

Optical Components

A few of the most common components are described in what follows in simple grounds, because these components were used most often during the experimental work. The reader is referred to conventional Optics literature for further details about each of this element.

Mirrors – When light passes from one medium to another of different refractive index, there is always some reflection, so the interface acts as a partially reflecting mirror. By applying an appropriate single-layer or multilayer coating to the interface between the two media, the reflection can be controlled so that the reflectance has any desired value between 0 and 1. If no transmitted light is required, high-reflectance mirrors can be made from metal-coated substrates or from metals themselves.

Flat mirrors are used to deviate the path of light rays without any focusing. These mirrors can have their reflective surface on the front face of any suitable substrate, or on the rear face of a transparent substrate. Front-surface, totally reflecting mirrors have the advantage of producing no unwanted additional or ghost reflections, however, their reflective surface is exposed. Rear-surface mirrors produce ghost reflections, as illustrated in Figure 2.3, unless their front surface is antireflection coated; but the reflective surface is protected. [13]

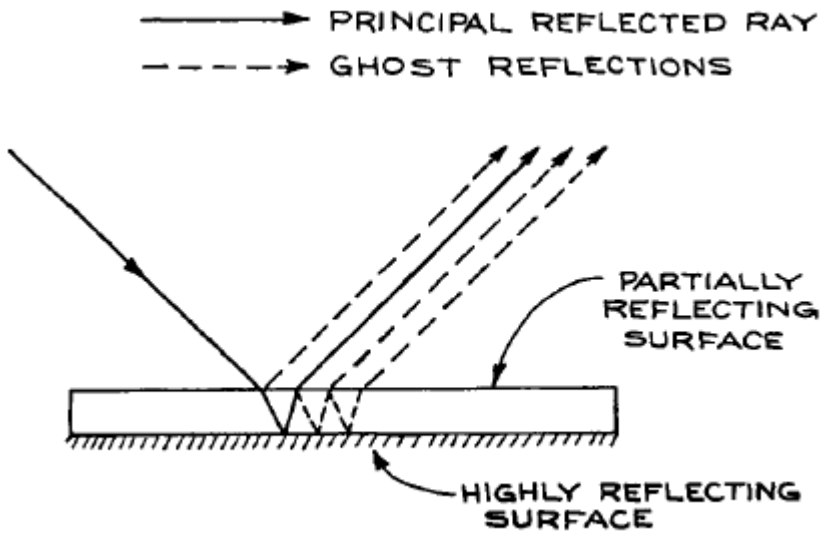

Figure 2.3 – Flat mirror producing ghost reflections [13]

Beamsplitters – are semitransparent mirrors that both reflect and transmit light over a range of wavelengths. A good beamsplitter has a multilayer dielectric coating on a substrate that is slightly wedge-shaped to eliminate interference effects, and antireflection-coated on its back surface to minimize ghost images. The ratio of reflectance to transmittance of a beamsplitter depends on the polarization state of the light.

Cube beamsplitters are pairs of identical right-angle prisms cemented together on their hypotenuse faces. Before cementing, a metal or dielectric semi reflecting layer is placed on one of the hypotenuse faces. Antireflection-coated cube prisms have virtually no ghost image problems and are more rigid than plate type beamsplitters. [13]

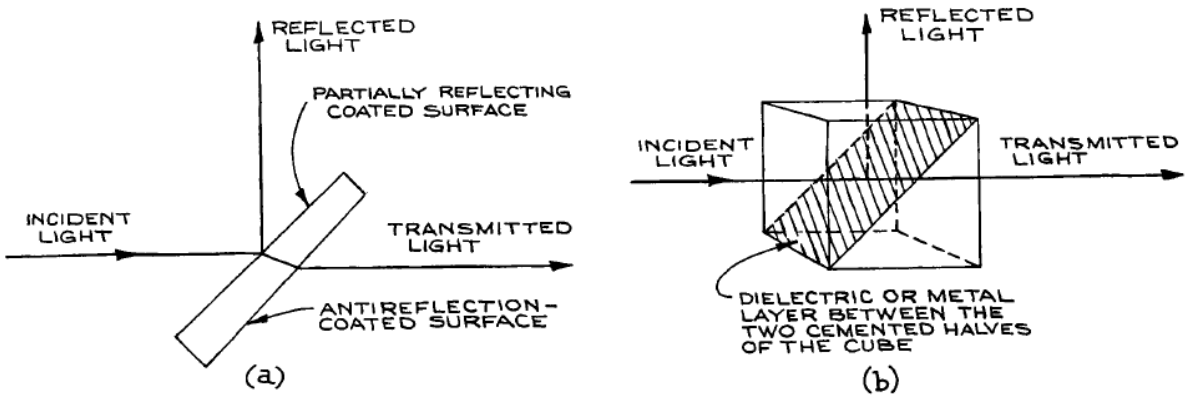

Figure 2.4 – (a) Conventional planar beamsplitter; (b) Cube beamsplitter [13]

Lenses – The lens is specified by the material of which it is made, the curvatures R1 and R2 of its two faces, the thickness d of the lens at its mid-point, and its aperture diameter D, which also indirectly specifies its thickness at the edge. The lens has an effective focal length (EFL), *f* measured from its principal planes, and front and back focal lengths, which specify the distances of the focal points from the front and back surfaces of the lens. [13]

Acousto-optic Modulator (AOM) – The AOM is a device that modulates the amplitude of an incoming light beam such that the output beam bears a frequency deviation which is equal to the sound wave that travels inside this component. It is based on the acousto-optic effect, i.e. the modification of the refractive index by the oscillating mechanical pressure of a sound wave. A schematic diagram of how an AOM works is given by the Figure 2.5. The key element of an AOM is a transparent crystal (or piece of glass) through which the light propagates. A piezoelectric transducer attached to the crystal is used to excite a sound wave with a frequency of the order of 100 MHz. Light can then experience Bragg diffraction at the traveling periodic refractive index grating generated by sound wave, therefore, AOMs are sometimes called Bragg cells. The incident light with an appropriate angle θ_B to the sound wavefronts, will be diffracted if it simultaneously satisfies the condition for constructive interference and reflection from the sound wavefronts. This condition is $\sin\theta_B = \lambda/\lambda_s$, where λ is the laser wavelength in the acousto-optic material, and λ_s is the sound wavelength.

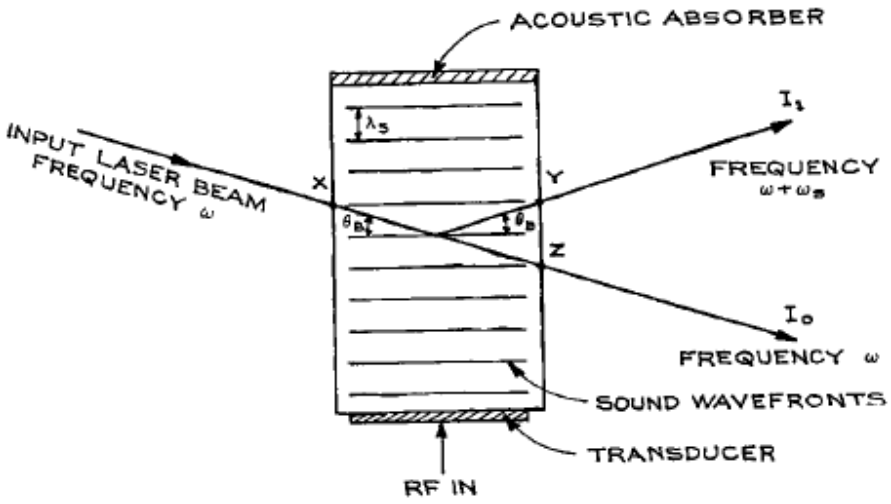

Figure 2.5 – Schematic diagram showing the operation of an acousto-optic device [13]

The AOM is used as an amplitude modulator by amplitude-modulating the input, which will be set to a specific optimum frequency for the device being used. Increase of drive power increases the diffracted power I_1 and reduces the power of the undeviated beam I_0 and vice versa. It also functions as a frequency shifter. In Figure 2.5 the laser beam reflects off a moving sound wave and is Doppler shifted so that the beam I_1 is at frequency $\omega + \omega_s$, where ω_s is the frequency of the sound wave.

AOMs are used in lasers for Q-switching, in telecommunications for signal modulating, and in spectroscopy for frequency control. [13]

Collimator – A laser collimator is an optical component that collimates and low-pass filters a laser beam. Laser beams are very collimated, i.e. low divergence light beams. The divergence of high-quality laser beams is commonly less than 1 milliradian, and can be much less for large-diameter beams. In spite of that, it is sometimes necessary to further ensure the light beam will propagate without diverging for very large distances and that is where the collimators come into action. A collimator is a telescope kind of optics assembly built in such way that the focus of the first lens is the back-focus of the exit lens. When the input beam is already a plane wave, the field at the focus of the first lens can be shown to be the Fourier Transform of the input field and therefore, a small pinhole positioned at this exact location will filter high frequencies in the laser beam, usually originating at diffraction sites along the beam propagation path.

Lasers

Lasers are now so widely used in physics, chemistry and engineering that they must be regarded as the experimentalist's most important type of optical source.

The lasers fall into two categories: pulsed and continuous wave (CW). For pulsed lasers, the available energy outputs per pulse can be classified as low < 10 mJ) medium (10 mJ–1 J), high (1 J–100 J), and very high (> 100 J). Pulse lengths depend on the type of laser and its mode of operation. Almost all pulsed solid-state lasers operate in a Q-switched mode. NonQ-switched long-pulse (LP) solid-state lasers have pulse lengths > 0.1 ms. Solid-state and dye lasers are frequently operated in a mode-locked (ML) configuration, which provides pulse lengths in the 0.1–10 ps range. A given laser can often be operated in ML, Q, and LP modes. The energy output per pulse will decrease as LP > Q > ML.

Continuous wave lasers can be classified by output power as low (< 10 mW), medium (10 mW–1 W), high (1–10 W), very high (10–100 W), and industrial (> 100 W). Continuous wave gas lasers, in particular, provide power outputs at many different wavelengths, and the available power varies from line to line. Ultraviolet gas lasers, for example, are equipped with special optics, so do not generally operate in the visible range as well.

A laser is an optical-frequency oscillator: in common with electronic circuit oscillators, it consists of an amplifier with feedback. The optical-frequency amplifying part of a laser can be a gas, a crystalline or glassy solid, a liquid, or a semiconductor. This medium is maintained in an amplifying state, either continuously or on a pulsed basis, by pumping energy into it appropriately.

Continuous wave Solid-State lasers – The most important laser in this category is the Nd:YAG laser, where YAG (yttrium aluminum garnet $Y_3Al_sO_{12}$ is the host material for the actual lasing species – neodymium ions, Nd^{3+}. The 1.06 μm can be efficiently doubled to yield a CW source of green radiation. This source of green radiation has replaced the argon-ion laser in many applications, especially since the neodymium laser itself can be pumped so conveniently with appropriate semiconductor lasers.

2.2.2 Propagation of light

The processes of transmission, reflection, and refraction are macroscopic manifestations of scattering occurring on a submicroscopic level.

The transmission of light through a homogeneous medium is an ongoing repetitive process of scattering and rescattering. Each such event introduces a phase shift into the light field, which ultimately shows up as shift in the apparent phase velocity of the transmitted beam from its nominal value of c. That corresponds to an index of refraction for the medium ($n = c/v$) which is other than one.

The scattered wavelets all combine in-phase in the forward direction to from what might best be called the secondary wave. For empirical reasons the secondary wave will combine with what is left of the primary wave to yield the only observed disturbance within the medium, namely, the transmitted wave. The refracted wave may appear to have a phase velocity less than, equal to, or even greater than c. The key to this apparent contradiction resides in the phase relationship between the secondary and primary waves.

Henceforth is possible to simply assume that a lightwave propagating through any substantive medium travels at a speed $v \neq c$. [14]

2.2.3 The Superposition of waves

The *Principle of Superposition* suggests that the resultant disturbance at any point in a medium is the algebraic sum of the separate constituent waves. There is a great interest on linear systems where the superposition principle is applicable. [14], for these systems exhibit the great advantage which is the ability to express the response of a system to an arbitrary input in terms of the responses to certain "elementary" functions into which the input has been decomposed.

Suppose that there are two waves, each with the same frequency and speed, coexisting in space.

$$E_1 = E_{01}\sin(\omega t + \alpha_1) \tag{2.5}$$

and

$$E_2 = E_{02}\sin(\omega t + \alpha_2) \tag{2.6}$$

In which E_0 is the amplitude of the harmonic disturbance propagating along the positive *x*-axis. The resultant disturbance is the linear superposition of these waves:

$$E = E_1 + E_2$$

The sum should resemble equations (2.5) and (2.6). Is not possible to add two signals of the same frequency and get a resultant with a different frequency.

Forming the sum, expanding equations (2.5) and (2.6), and separating out the time-dependent terms, the total disturbance then becomes

$$E = E_0\sin(\omega t + \alpha) \tag{2.7}$$

with

$$E = \sqrt{E_{01}^2 + E_{02}^2 + 2E_{01}E_{02}\cos(\alpha_2 - \alpha_1)} \quad and \quad \tan(\alpha) = \frac{E_{01}\sin(\alpha_1) + E_{02}\sin(\alpha_2)}{E_{01}\cos(\alpha_1) + E_{02}\cos(\alpha_2)} \tag{2.8}$$

The composite wave is harmonic and of the same frequency as the constituents, although its amplitude and phase are different. [14]

2.2.4 Two-beam Interference

Optical interference corresponds to the interaction of two or more lightwaves yielding a resultant intensity that deviates from the sum of the component intensities.

The physical consequence of the superposition principle is the observation of bright and dark bands of light called fringes when a number of waves coexist in a region in space. The bright regions occur when a number of waves add together to produce an intensity maximum of the resultant wave, this is called constructive interference. Destructive interference occurs when a number of waves add together to produce an intensity minimum of the resultant wave.

Collectively, the distribution of fringes is called an interference pattern.

In accordance with the Principle of Superposition, the electric field intensity, $\vec{E}$, at a point in space, arising from the separate fields $\overrightarrow{E_1}$, $\overrightarrow{E_2}$, … of various contributing sources is given by

$$\vec{E} = \overrightarrow{E_1} + \overrightarrow{E_2} + ... \tag{2.9}$$

The optical disturbance, or light field $\vec{E}$, varies in time at an exceedingly rapid rate making the actual field an impractical quantity to detect. On the other hand, the intensity *I* can be measured directly with a wide variety of sensors. The study of interference is therefore best approached by way of the intensity.

The intensity is given by

$$I = I_1 + I_2 + I_{12} \tag{2.10}$$

The interference term becomes

$$I_{12} = 2\sqrt{I_1 I_2}\cos\delta \tag{2.11}$$

Whereupon the total intensity is

$$I = I_1 + I_2 + 2\sqrt{I_1 I_2}\cos\delta \tag{2.12}$$

Where δ, equal to $(\phi_1 - \phi_2)$, is the phase difference arising from a combined path length and initial phase angle difference as can be seen in Eq. (2.8) above.

The wavelength of light depends on the propagation velocity in the medium. In order to allow the light to propagate along paths in media with different indices of refraction and still evaluate their phase differences, all path lengths are converted to an equivalent path length within a vacuum. The equivalent path length or the optical path length between points A and B in a medium with an index of refraction *n* is defined as the distance a wave in a vacuum would travel during the time it took a light to travel from A to B in the actual medium. If the distance between A and B is *r* and the velocity of propagation in the medium is *v*, then the time to travel from A to B is $\tau = r/v$. The distance light would travel in a vacuum in the time *τ*, that is, the optical path length, is given by

$$c\tau = \frac{cr}{v} = nr \tag{2.13}$$

The phase difference δ can be expressed in terms of the optical path length. Both waves were assumed to have the same frequency; therefore, the propagation constant of wave *i* is

$$|k_i| = \frac{n_i 2\pi}{\lambda_0} \tag{2.14}$$

Where λ_0 is the wavelength of the waves in a vacuum and n_i is the index of refraction associated with the path of the *i*th wave.

At various points in space, the resultant intensity can be greater, less than, or equal to $I_1 + I_2$, depending on the value of I_{12} that is, depending on δ. A maximum intensity is obtained when cos δ = 1, so that

$$I_{\max} = I_1 + I_2 + 2\sqrt{I_1 I_2} \tag{2.15}$$

When $\delta = 0, \pm 2\pi, \pm 4\pi, \ldots$ In this case of total constructive interference, the phase difference between the two waves is an integer multiple of 2π, and the disturbances are in-phase. When 0 < cos δ < 1 the waves are out-of-phase, $I_1 + I_2 < I < I_{max}$, and the result is constructive interference. At $\delta = \pi/2, cos\delta = 0$, the optical disturbances are 90º out-of-phase, and $I = I_1 + I_2$. For 0 > cos δ > -1 we have the condition of destructive interference, $I_1 + I_2 > I > I_{min}$. A minimum intensity results when the waves are 180º out-of-phase, troughs overlap crests, cos δ=-1 and

$$I_{\min} = I_1 + I_2 - 2\sqrt{I_1 I_2} \tag{2.16}$$

This occurs when $\delta = \pm\pi, \pm 3\pi, \pm 5\pi, \ldots$, and it is referred to as total destructive interference.

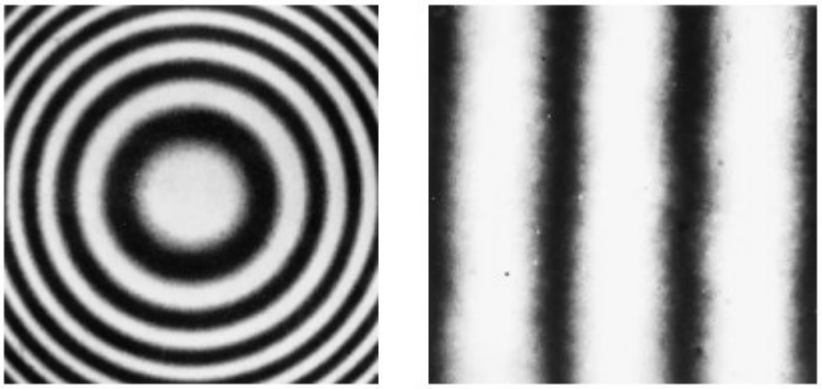

Figure 2.6 – Interference fringes [15]

If two beams are to interfere to produce a stable pattern, they must have very nearly the same frequency. A significant frequency difference would result in a rapidly varying, time dependent phase difference, which in turn would cause I_{12} to average to zero during the detection interval. Still, if the sources both emit white light, the component reds will interfere with reds and the blues with blues. A great many fairly similar slightly displaced overlapping monochromatic patterns will produce one total

white-light pattern. It will not be as sharp or as extensive as a quasi-monochromatic pattern, but white light will produce observable interference. The clearest patterns exist when the interfering waves have equal or nearly equal amplitudes. The central regions of the dark and light fringes then correspond to complete destructive and constructive interference, respectively yielding maximum contrast. For a fringe pattern to be observed the two sources need not be in-phase with each other. A somewhat shifted but otherwise identical interference pattern will occur if there is some initial phase difference between the sources, as long as it remains constant. Such sources are coherent. [14, 16]

Any conventional extended light source is an incoherent source of light because different portions of the source are mutually incoherent. Atoms and molecules in a conventional source emit light randomly through the process of spontaneous emission. The situation in a laser is qualitatively different. A laser is also an extended source but the dominant process of light emission is the stimulated emission which forces the atoms and molecules to emit light in unison. Laser light therefore possesses a high degree of monochromaticity and coherence. Interference effects are best illustrated with laser sources. With incoherent light sources, one must devise ways to produce mutually coherence waves. Extended sources can be used to observe two-wave interference but it can be considered as a sufficiently small source which can be treated as a point source. Such a source can be constructed by placing an extended quasi-monochromatic light source inside a dark enclosure with a small hole. This tiny hole, through which light escapes from the enclosure, acts as a point source if its dimensions are sufficiently small.

Mutually coherent quasi-monochromatic waves can be obtained from a ‘point source’ in two ways. In the wavefront division approach, the spherical wavefront emanating from the point source is split and then recombined after introducing an appropriate path difference. Alternatively, the amplitude of the incident wave is split at an interface between two media in a process denominated “division of amplitude”, as in Michelson interferometer, to generate two waves which interference upon recombination. [17]

Wavefront Division

As an example of a wavefront-dividing interferometer, consider the oldest of all interference experiments due to Thomas Young (1980), that finally demonstrated the wave nature of light. The incident wavefront is divided by passing through two small holes at P_1 and P_2 in a screen S_1. The emerging spherical wavefronts from P_1 and P_2 will interfere, and the resulting interference pattern is observed on the screen S_2.

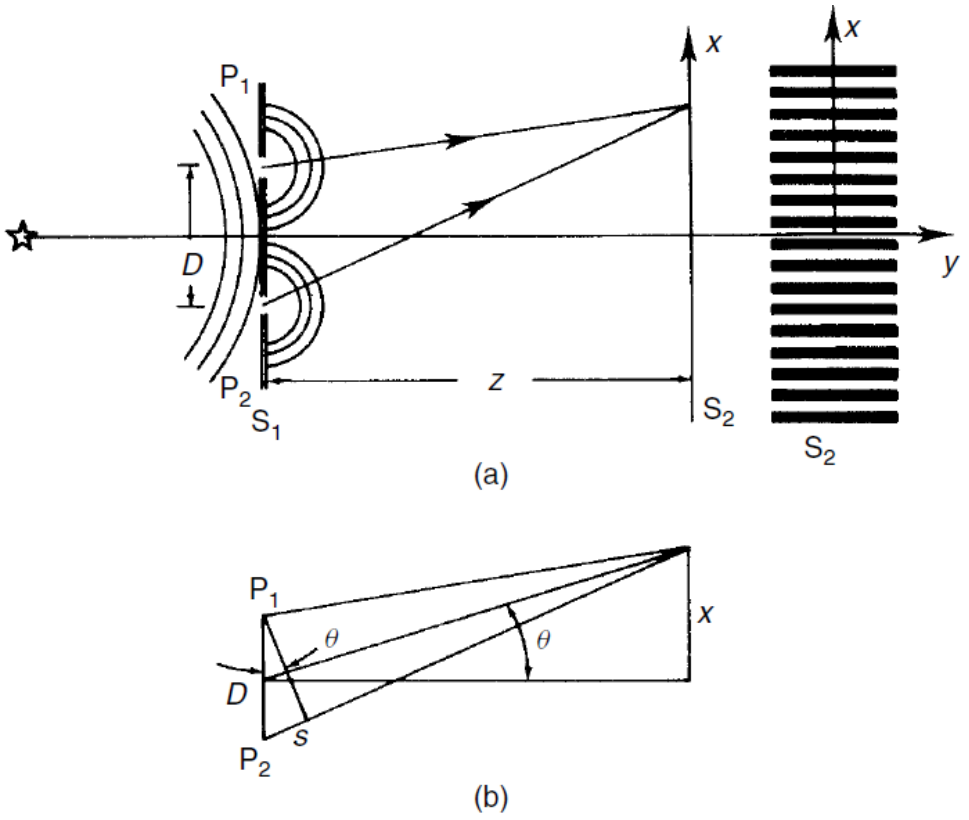

Figure 2.7 – Young's Interferometer [18]

The geometric path length difference s of the light reaching an arbitrary point x on S_2 from P_1 and P_2 is found from Figure 2.7(b). When the distance z between S_1 and S_2 is much greater than the distance D between P_1 and P_2

$$s = \frac{D}{z}x \tag{2.17}$$

The phase difference therefore becomes

$$\delta = \frac{2\pi}{\lambda}s = \frac{2\pi D}{\lambda z}x \tag{2.18}$$

Which, inserted into the general expression for the total intensity, equation (2.12), gives

$$I(x) = 2I\left(1+\cos\left(2\pi\frac{D}{\lambda z}x\right)\right) \tag{2.19}$$

The interference fringes are parallel to the y-axis with a spatial period $\lambda z/D$ which decreases as the distance between P_1 and P_2 increases.

It is assumed that the waves from P_1 and P_2 are fully coherent. This is an ideal case and becomes more and more difficult to fulfill as the distance D between P_1 and P_2 is increased. The contrast of the interference fringes on S_2 is a measure of the degree of coherence. There is a Fourier transform

relationship between the degree of coherence and the intensity distribution of the light source. By assuming the source to be as incoherent circular disc of uniform intensity, one can find the diameter of the source to by increasing the separation between P_1 and P_2 until the contrast of the central interference fringe on S_2 vanishes. This is utilized in Michelson's stellar interferometer (Figure 2.8(c)) to measure the diameter of distant stars. This is an extension of Young's interferometer, where a mirror arrangement is used to make the effective distance *D* sufficiently long. [18]

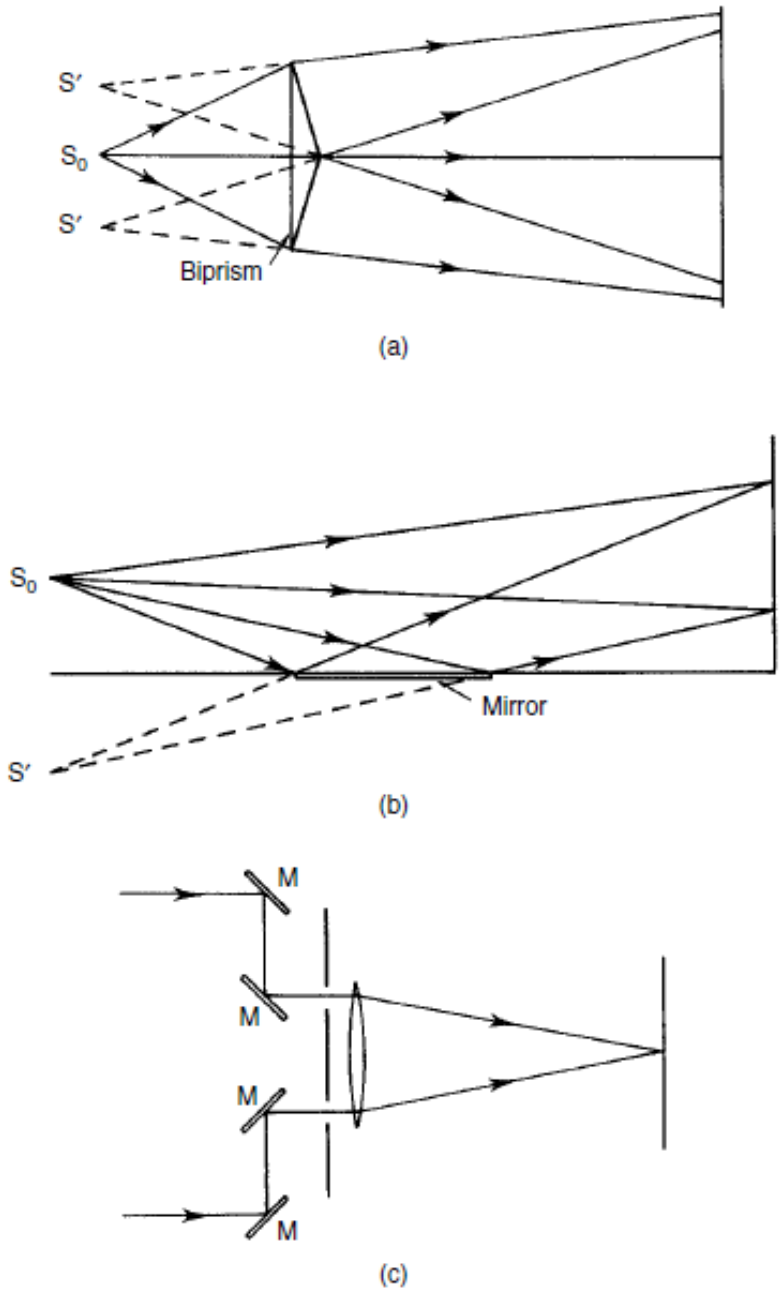

Figure 2.8 – Examples of wavefront-dividing interferometers: (a) Fresnel biprism; (b) Lloyd's mirror; (c) Michelson's stellar interferometer [18]

Amplitude Division

The most well-known amplitude-dividing interferometer is the Michelson interferometer, which can be seen in Figure 2.9. Here the amplitude of the incident light field is divided by the beamsplitter BS which is partly reflecting. The reflected and the transmitted partial waves propagate to the mirrors M_1 and M_2 respectively, from where they are reflected back and recombine to form the interference distribution on the detector D.

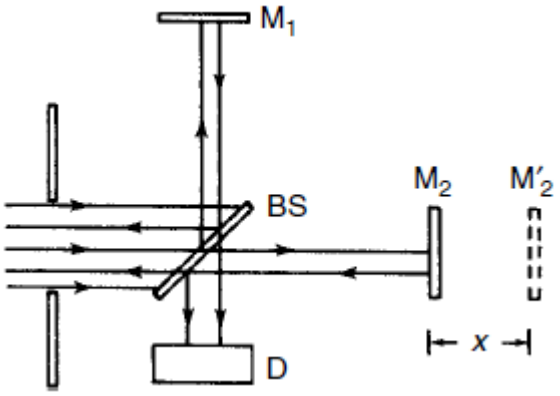

Figure 2.9 – Michelson's interferometer [18]

The path-length difference between the two partial waves can be varied by moving one of the mirrors. A displacement x of M_2 gives a path length difference $2x$ and a phase equal to $\delta = (2\pi/\lambda)2x$. This results in a total intensity given by

$$I(x) = 2I\left(1+\cos\frac{4\pi x}{\lambda}\right) \tag{2.20}$$

As M2 moves, its displacement is measured by counting the number of light maxima registered by the detector. By counting the numbers of maxima per unit time, one can find the speed of the object.[18]

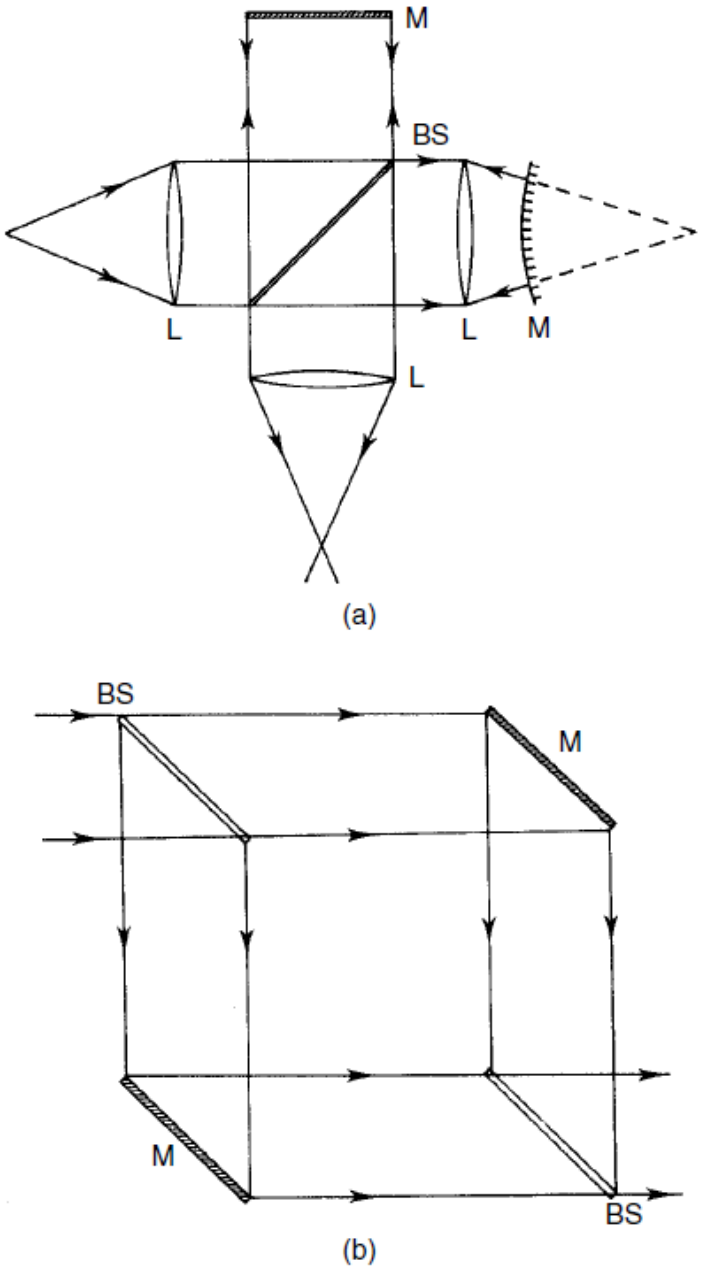

Figure 2.10 – Further examples of amplitude-dividing interferometers: (a) Twyman-Green interferometer; (b) Mach-Zehnder interferometer [18]

2.2.5 Coherence

Coherence can be broadly described as the property that enables two electromagnetic fields to interfere. In order to fully grasp the concept, and although the properties of *spatial* and *temporal* coherence are not tantamount to the description of coherent light, they are helpful for an intuitive understanding of the nature of partially coherent light and will, as such, be briefly described in what follows.

In as much as temporal coherence can be described as a measure of the degree of the spectral purity of a wave, i.e., how monochromatic the radiation is, spatial coherence is a measure of the spatial extent of the source, an ideal source being confined to a point in space.

Temporal coherence is intimately related to the frequency bandwidth of a truncated wave train. It determines how far two points along the direction of propagation of a wave can be, and still possess a definite phase relationship. For that reason, temporal coherence is also called longitudinal coherence. The Michelson interferometer, which senses longitudinal path differences between the interfering waves, is ideally suited for investigating temporal coherence of light fields.

Spatial coherence of light fields depends on the physical size of the light source. Light coming from a point source, which may be taken as a source with dimensions not exceeding the mean wavelength of the emitted light, possesses a high degree of spatial coherence, irrespective of the frequency bandwidth of the source.

Commonly observed speckles with laser light reflect a high degree of spatial coherence of laser light, despite the laser not being a point source. Light from a conventional extended source, on the other hand, has considerably reduced spatial coherence because different points on an extended source radiate independently and therefore are mutually incoherent. Light emanating from an extended source cannot be characterized by a definite state of spatial coherence. Also, the spatial coherence of light from an extended source changes as light propagates.

Spatial coherence of light determines how far two points can lie in a plane transverse to the direction of propagation of light and still be correlated in phase. Spatial coherence of light can be investigated by interferometers of the type used by Young in is famous two-slit interference experiment. [17]

Detection of light is an averaging process in space and time. In developing equation (2.12) no averaging was made because it was assumed the phase difference to be constant in time. Ideally, a light wave with a single frequency must have an infinite length. Therefore, sources emitting light of a single frequency do not exist.

One way of illustrating the light emitted by real sources is to picture it as sinusoidal wave trains of finite length with randomly distributed phase differences between the individual trains.

In Figure 2.11 two successive wave trains of the partial waves are sketched. The two wave trains have equal amplitude and length L_c, with an abrupt, arbitrary phase difference. Figure 2.11 (a) shows the situation when the two partial waves have travelled equal path lengths. Although the phase of the original wave fluctuates randomly, the phase difference between the partial waves 1 and 2 remains constant in time. The resulting intensity is therefore given by equation (2.12). Figure 2.11 (c) shows the situation when partial wave 2 has travelled a path length L_c longer than partial wave 1. The head of the wave trains in partial wave 2 then coincide with the tail of the corresponding wave trains in partial wave 1. The resulting instantaneous intensity is still given by equation (2.12), but now the phase

difference fluctuates randomly as the successive wave trains pass by. As a result, $\cos\delta$ varies randomly between +1 and -1. When averaged over many wave trains, $\cos\delta$ therefore becomes zero and the resulting, observable intensity will be

$$I = I_1 + I_2 \tag{2.21}$$

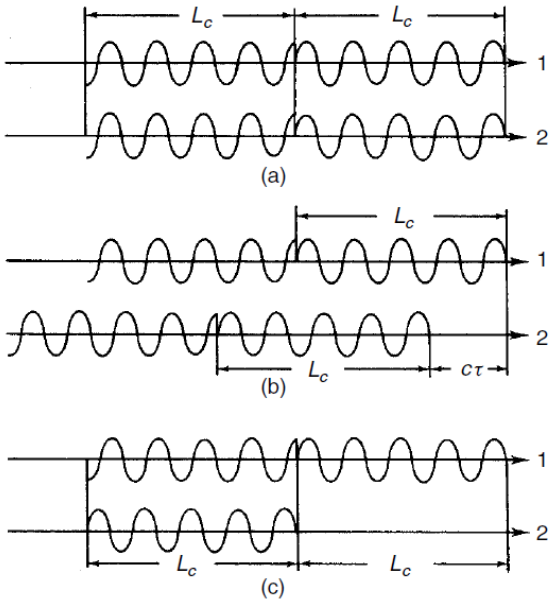

Figure 2.11 – Wave trains of the partial waves [18]

Figure 2.11 (b) shows an intermediate case where partial wave 2 has travelled a path length l longer than partial wave 1, where $0 < l < L_c$. Averaged over many wave trains, the phase difference now varies randomly in a time period proportional to $\tau = l/c$ and remains constant in a time period proportional to $\tau_c - \tau$ where $\tau_c = L_c/c$. The result is that is still possible to observe an interference pattern according to equation (2.12), but with a reduced contrast. To account for this loss of contrast, equation (2.12) can be written as

$$I = I_1 + I_2 + 2\sqrt{I_1 I_2}\,|\gamma(\tau)\cos\delta| \tag{2.22}$$

Where $|\gamma(\tau)|$ means the absolute value of $\gamma(\tau)$.

The definition of contrast or visibility is now introduced,

$$V = \frac{I_{\max} - I_{\min}}{I_{\max} + I_{\min}} \tag{2.23}$$

Where $I_{\max}$ and $I_{\min}$ are two neighboring maxima and minima of the interference pattern described by equation (2.22). Since $\cos\delta$ varies between +1 and – 1:

$$I_{\max} = I_1 + I_2 + 2\sqrt{I_1 I_2}\,|\gamma(\delta)| \tag{2.24}$$

$$I_{\min} = I_1 + I_2 - 2\sqrt{I_1 I_2}\,|\gamma(\delta)| \tag{2.25}$$

Which, inserting on equation (2.23) gives:

$$V = \frac{2\sqrt{I_1 I_2}\,|\gamma(\tau)|}{I_1 + I_2} \tag{2.26}$$

For two waves of equal intensity, $I_1 = I_2$, equation (2.26) becomes,

$$V = |\gamma(\tau)| \tag{2.27}$$

which shows that in this case $|\gamma(\tau)|$ is exactly equal to the visibility. $\gamma(\tau)$ is termed the complex degree of coherence and is a measure of the ability of the two wave fields to interfere. [18]

2.2.6 Two-beam Interferometers

A number of two-wave interferometers exist with countless applications in optics, metrology, plasma diagnostics, and other related fields. Most of these interferometers are variants of the historic Michelson interferometer. This will be followed by a brief discussion on other commonly used interferometers like Mach-Zehnder interferometer and VISAR. All of these interferometers are amplitude-dividing interferometers.

Michelson interferometer

In the Michelson interferometer a beam splitter (a semitransparent mirror) is used to divide the light into two beams as shown in Figure 2.12.

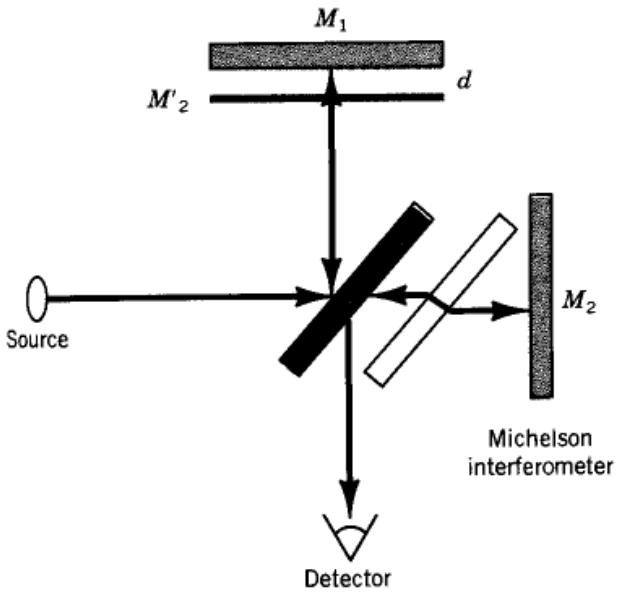

Figure 2.12 – Michelson Interferometer [16]

The two beams are directed along orthogonal paths, usually called the arms of the interferometer, where they strike two mirrors, M_1 and M_2, and then return to the beam splitter where they interfere. Looking at the beam splitter from the detector is possible to see an image of mirror M_2 near mirror M_1. The image M_2' and the mirror M_1 form a dielectric layer of thickness *d*. The interferometer is assumed to be in the air so that the dielectric layer has an index of refraction n_2=1. Also, light reflected from M1 and M2 experiences the same phase change upon reflection, thus, no additional phase shift needs to be added to Δ in calculating the phase difference between the two waves. The total phase difference for a bright band is

$$\delta = 2\pi m = \frac{2d \cdot 2\pi \cos\theta_t}{\lambda_0} \tag{2.28}$$

The source shown in Figure 2.12 is nearly a point source, generating spherical waves that produce fringes of constant inclination. The fringes are circularly symmetric if *d* is a constant across the aperture. The maximum value of *m*, the order of the fringe, occurs at the center of the set of fringe rings where θ_t=0

$$m_{\max} = \frac{2d}{\lambda_0} \tag{2.29}$$

The order of the fringes is shown by equation (2.29) to be equal to the difference in lengths of the two interferometer arms expressed in the number of wavelengths of light contained in *d*.

As *d* increases, a bright band will move out from the center of the aperture and a new bright band of higher order will take its place at the center. If the detector is placed at the position of the center fringe and monitored the intensity as we moved one of the mirrors, and thereby changed *d*, we should see

$$I = I_1 + I_2 + 2\sqrt{I_1 I_2}\cos\left(\frac{2\omega d}{c}\right) \tag{2.30}$$

Where

$$\frac{\omega}{c} = \frac{2\pi}{\lambda_0} \tag{2.31}$$

If the beam splitter is a 50:50 splitter, then the intensity of the light in the two arms will be the same:

$$I = I_0\left[1 + \cos\left(\frac{2\omega d}{c}\right)\right] \tag{2.32}$$

If we use the physical arrangement shown in Figure 2.12, the light in the M_1 arm of the interferometer travels an extra distance *2d* to reach the detector. This means that two waves are added together that originated at different times; the difference in time between the origination of two waves is:

$$\tau = \frac{2d}{c} \tag{2.33}$$

Which is called the *retardation time* (the wave in arm M1 has been delayed or retarded). Using the equation (2.33),

$$I = I_0\left[1 + \cos\omega\tau\right] \tag{2.34}$$

The signal is made up of a constant term plus an oscillatory term. The oscillatory term will provide information about the coherence properties of the light. [16]

Mach-Zehnder Interferometer

The Mach-Zehnder interferometer is another amplitude splitting device. As shown in Figure 2.13, is consists of two beam splitters and two totally reflecting mirrors. The two waves within the apparatus travel along separate paths. A difference between the optical paths can be introduced by a slight tilt of one of the beam splitters. Since the two paths are separated, the interferometer is relatively difficult to align. For the same reason, however, the interferometer finds myriad applications. It has even been used, in a somewhat altered yet conceptually similar from, to obtain electron interference fringes.

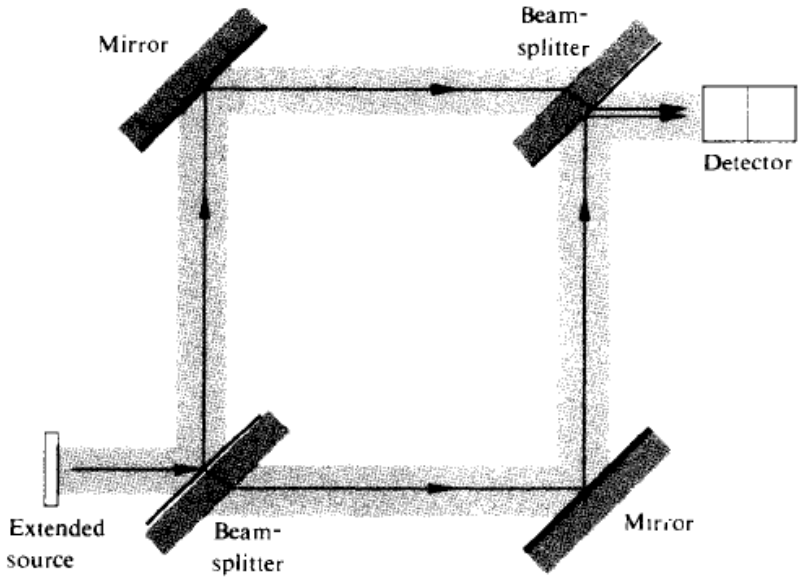

Figure 2.13 – Mach-Zehnder interferometer [14]

An object interposed in one beam will alter the optical path length difference, thereby changing the fringe pattern. A common application of the device is to observe the density variations in gas-flow patterns within research chambers. One beam passes through the optically flat windows of the test chamber, while the other beam transverses appropriate compensator plates. The beam within the chamber will propagate through regions having a spatially varying index of refraction. [14]

VISAR system

The VISAR (Velocity Interferometer System for Any Reflector) is a robust tool widely used to measure surface velocities optically. This technique was developed by Barker and Hollenbach based in two previous techniques, the Wide Angle Michelson Interferometer (WAMI) and the Lockheed Laser Velocimeter.

VISAR is a homodyne technique, this means that, the Doppler-shifted light is divided in two optical ways of differing length and recombined at the photo detector. In short, VISAR does not truly measure the Doppler shift, it measures the difference in the Doppler shift between two relatively Doppler shifted reflected light beams. Since the introduction of VISAR, it has gone through several evolutions like the multipoint VISAR, fixed cavity VISAR, among others.

As referred before, VISAR consists in an unequal leg Michelson interferometer where monochromatic light reflected from a target is divided and transverses two legs. One of those legs, despite the distance along both tracks appears to be the same, has a longer delay time, so that when the beams recombined at the beam splitter mirror, is produced the interference that contains the Doppler-shift changes of the moving target. [19]

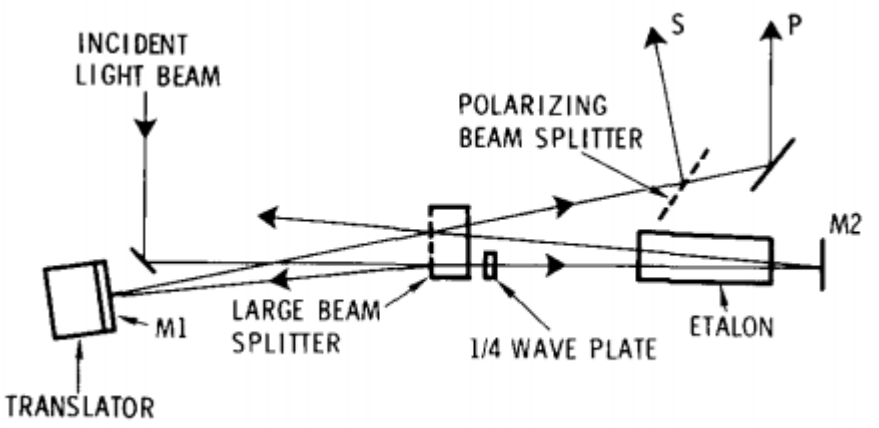

Figure 2.14 – VISAR Interferometer [20]

Figure 2.14 shows a schematic of the VISAR. The incident light beam is the light reflected from the surface of the specimen that already contains the Doppler shift resulting from the movement of the surface. The beam then insides the large beam splitter. The reflected part of the beam is returned by the M1 to the large beam splitter, where it is recombined with the originally transmitted part of the incident beam. Because of the recombination, the transmitted part of the beam has some delay with respect to the reflected beam from the etalon. The delay time is given by

$$\tau = \frac{2h}{c} \cdot \frac{n-1}{n} \tag{2.35}$$

Where h is the effective length of the etalon, c is the velocity of light in free space and n is its index of refraction.

Both the orientation and the distance from the mirror 2 are adjustable to simplify the alignment of the interferometer and to accommodate the various etalon lengths.

The velocity in VISAR is related to the fringes in the recombined beam, therefore, the velocity change corresponding to per fringe increase is defined as the fringe constant F_v

$$F_v = \frac{\lambda_0}{2\tau} \tag{2.36}$$

The velocity of the moving surface as time t, $u(t)$, is related to the total fringe number $N(t)$,

$$u\left(t - \frac{1}{2}\tau\right) = N(t)\frac{F_v}{(1+\delta)} \tag{2.37}$$

Where Δ is a correction parameter due to the frequency dispersion of the laser beam propagating in the etalon.

In summary, the VISAR system compared to similar velocity measurement interferometers is more compact and less expensive; and it can be obtained from commercial vendors, this system is vulnerable to abrupt changes in velocity and depends on having a second etalon to resolve fringe jump

ambiguities. For data analysis, VISAR uses absolute intensities to obtain the velocity information. This system, like other laser interferometers, requires very precise alignment and adjustment of the optical elements. It can measure the material velocity with 1% accuracy and a resolution better than 1 ns. By changing the etalon, it is possible to increase the range of measurable velocities [19-28]

2.2.7 Multiple-beam Interference

A number of situations in which two coherent beams are combined under diverse conditions to produce interference patterns have been scrutinized. There are, however, circumstances under which a much larger number of mutually coherent waves are made to interfere. In fact, whenever the amplitude-reflection coefficients, the *r*'s, for the parallel plate illustrated in Figure 2.15 are not small, the higher-order reflected waves $\overrightarrow{E_{3r}}, \overrightarrow{E_{4r}}$,… become quite significant. A glass plate, slightly silvered on both sides so that the *r*'s approach unity, will generate a large number of multiply internally reflected rays.

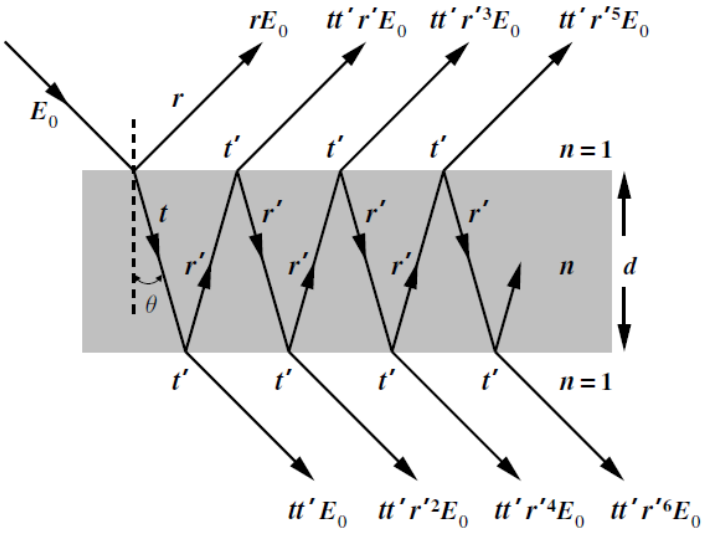

Figure 2.15 – Multiple-beam interference from a parallel film [17]

To begin the analysis as simple as possible, let the film be non-absorbing and $n_1 = n_2$. The amplitude-transmission coefficients are represented by *t*, the fraction of the amplitude of a wave transmitted on entering into the film, and *t'*, the fraction transmitted when a wave leaves the film.

As shown in Figure 2.15 – Multiple-beam interference from a parallel film [17], the scalar amplitudes of the reflected waves $\overrightarrow{E_{1r}}, \overrightarrow{E_{2r}}, \overrightarrow{E_{3r}}$, …, are respectively rE_0, $tt'r'E_0, tt'r'^3E_0$, …, where E_0 is the amplitude of the initial incoming wave and $r = -r'$. The minus sign indicates a phase shift. Similarly, the transmitted waves $\overrightarrow{E_{1t}}, \overrightarrow{E_{2t}}, \overrightarrow{E_{3t}}$, … will have amplitudes $tt'^{E_0}, tt'r'^2E_0, tt'r'^4E_0$, …. [14]

Each transmitted wave will have a constant phase difference, relative to its neighbor,

$$\delta = \frac{4\pi d n_2 \cos\theta_t}{\lambda_0} \tag{2.38}$$

Where $n = 0, 1, 2, ...$

The intensity of the transmitted light is,

$$I \propto \frac{E^2}{\left(1-r^2\right)^2 + 4r^2 \sin^2 \frac{\delta}{2}} \tag{2.39}$$

When $\delta = 0, 2\pi, 4\pi, ...$

$$I_{\max} \propto \frac{E^2}{\left(1-r^2\right)^2} \tag{2.40}$$

When $\delta = \pi, 3\pi, 5\pi, ...$

$$I_{\min} \propto \frac{E^2}{\left(1+r^2\right)^2} \tag{2.41}$$

The fringe visibility is a useful characterization of interference; the larger the value of this parameter, the easier it is to observe the fringe pattern. The maximum value of fringe visibility is 1 and occurs when $I_{min} = 0$; the minimum value is zero and occurs when $I_{max} = I_{min}$. Using equation (2.40) and (2.41) in (2.10), it is obtained the fringe visibility in terms of the reflectivity of the film surface

$$v = \frac{2r^2}{1+r^4}$$

As the reflectivity r^2 approaches 1, the fringe visibility approaches its maximum value of 1.

The intensity transmitted through the dielectric layer in terms of I_{max} is,

$$I = \frac{I_{\max}}{1 + \frac{4r^2}{\left(1-r^2\right)^2} \sin^2 \frac{\delta}{2}} \tag{2.42}$$

The factor

$$\frac{4r^2}{\left(1-r^2\right)^2} = F \tag{2.43}$$

Is called the *contrast F* and its use allows the relative transmission of the dielectric layer to be expressed in a format called the *Airy function*.

$$\frac{I}{I_{\max}} = \frac{1}{1 + F\sin^2\frac{\delta}{2}} \tag{2.44}$$

Plotting the Airy function for different values of the reflectivity r^2 is possible to obtain the Figure 2.16 which displays a periodic maximum in the transmission of the dielectric layer as δ is varied. The peak in transmission occurs when d is equal to a multiple of $\lambda/2$, where λ is the illuminating wavelength. Thus, the maximum transmission of the film thickness will support standing waves in the layer, that is, the transmission maxima occurs for eigenvalues of the layer. [16]

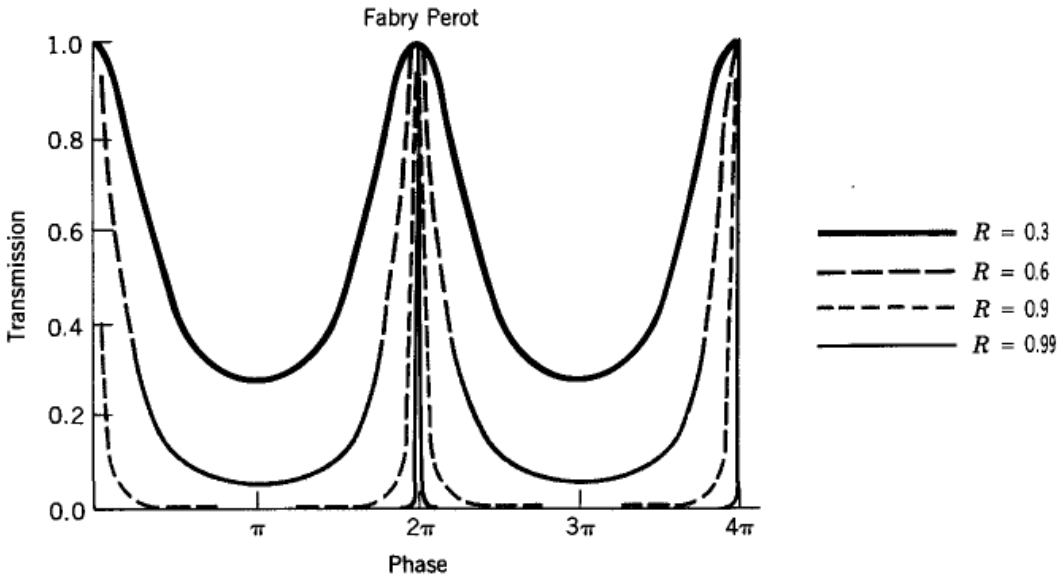

Figure 2.16 – Plot of the fraction of transmitted light as a function of the optical path length [16]

The peak transmission in Figure 2.16 narrows as the reflectivity r^2 increases. The value of δ over which I goes from $I_{\max}$ to $I_{\max}/2$ is a measure of the fringe sharpness and can be obtained by noting $I = I_{max}$ when δ=0. When $I = I_{max}/2$,

$$\frac{4r^2 sin^2\frac{\delta}{2}}{(1-r^2)^2} = 1$$

The fringe sharpness is given by

$$\delta_{1/2} = 2\sin^{-1}\left(\frac{1-r^2}{2r}\right) = 2\sin^{-1}\left(\frac{1}{\sqrt{F}}\right) \tag{2.45}$$

The sharpness of the fringes increases and $\delta_{1/2}$ decreases with increasing reflectivity.

Fabry-Perot interferometer

Fabry Perot interferometer, Figure 2.17, consists of two plane, parallel, highly reflecting surfaces separated by a distance d. This is the simplest configuration. and other forms are also widely used. In practice, two semi-silvered or aluminized glass optical flats form the reflecting boundary surfaces. The enclosed air gap generally ranges from several millimetres to several centimeters when the apparatus is used interferometrically, and often to considerably greater lengths when it serves as a laser resonant cavity.

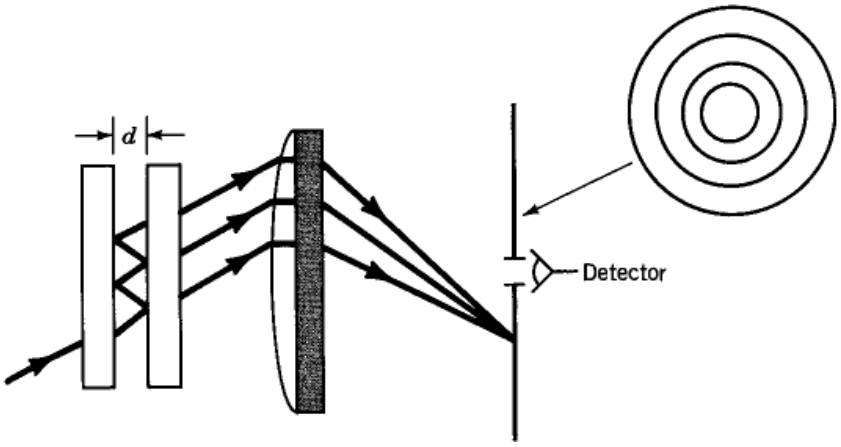

Figure 2.17 – Experimental arrangement of a Fabry-Perot interferometer [16]

The waves in the plates, after multiple reflections, are collected by the lens and imaged on an observation screen. Only one propagation vector, incident at an angle θ, is followed through the system in Figure 2.17. Other incident propagation vectors will result in a bright band if $\delta = 2\pi m$. The incident angle of propagation vectors forming the bright bands must satisfy the equation

$$m\lambda = 2nd\cos\theta \tag{2.46}$$

The observed fringes, such as those in Figure 2.18 – Output fringes from a Fabry-Perot interferometer [16]are circularly symmetric if the illumination is symmetric about the symmetry axis of the optical system.

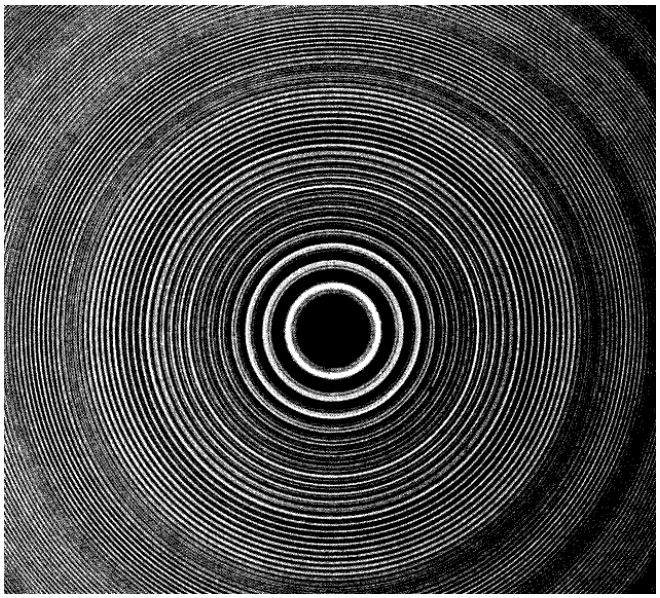

Figure 2.18 – Output fringes from a Fabry-Perot interferometer [16]

The accuracy with which an interferometer can measure the wavelength of its illumination is called *chromatic resolving power*, $\mathcal{R}$, and is defined as $\lambda/\Delta\lambda$, where λ is the mean wavelength of the illumination and $\Delta\lambda$ is the wavelength difference that can be resolved. The criterion for resolution assumes that two wavelengths λ_1 and λ_2 of equal intensity are present. The criterion for resolution of the two wavelengths states that the two wavelengths are just resolved if the half-maximum intensity of a fringe produced by λ_1 falls on the half-maximum intensity of a fringe produced by λ_2. When this occurs, the transmitted intensity is a constant as d is varied from the resonant condition of λ_1 to the resonant condition of λ_2. The phase shift in going from the intensity maximum for λ_1 to the intensity maximum for λ_2 is then $\Delta\delta=2\delta_{1/2}$. The fringes are assumed to be narrow so that this is a small value with the approximation

$$\sin\delta_{1/2} = \sin\frac{\Delta\delta}{2} \approx \frac{\Delta\delta}{2}$$

And

$$\sin\left(\frac{\delta_{1/2}}{2}\right) = \frac{\Delta\delta}{4}$$

A bright band will occur whenever

$$2n_2 d\cos\theta_t = m\lambda \tag{2.47}$$

The relationship between $\Delta\theta$ and $\Delta\lambda$ is

$$-\sin\theta_t\Delta\theta_t = \frac{m\Delta\lambda}{2n_2 d} \tag{2.48}$$

The resolving power is thus

$$\mathcal{R} = \frac{\lambda}{\Delta\lambda} = \frac{m\pi r}{1-r^2} = \frac{m\pi}{2}\sqrt{F} \qquad \textbf{(2.49)}$$

From equation (2.47) is possible to see that the order number *m* has a maximum value whenever $cos\ \theta_t = 1$, that is, m is a maximum at the center of the Fabry-Perot fringe pattern and this maximum is given by

$$m_{\max} = \frac{2n_2 d}{\lambda_0} \qquad \textbf{(2.50)}$$

2.3 Heterodyne technique

Heterodyne interferometry is on of the most flexible and accurate interferometric surface profile or displacement measurement techniques available today, there being current commercial systems available for the measurement of *nm* ranges with sub-Angstrom accuracy to 60 *m* ranges or 100 *mm* ranges to 1 part in 10^8 accuracy. An elegant exposé of a full-field, real time measurement system to λ/100 accuracy tested on 5 *cm* mirrors was made by Massie in 1979. Remarkable 0.1 *mm* resolution for 100 *m* ranges have also been reported and a Super Heterodyne interferometer using two laser wavelengths and two heterodyning frequencies simultaneously was described by Tiziani with a striking 50 μm resolution for 100 *m* ranges.

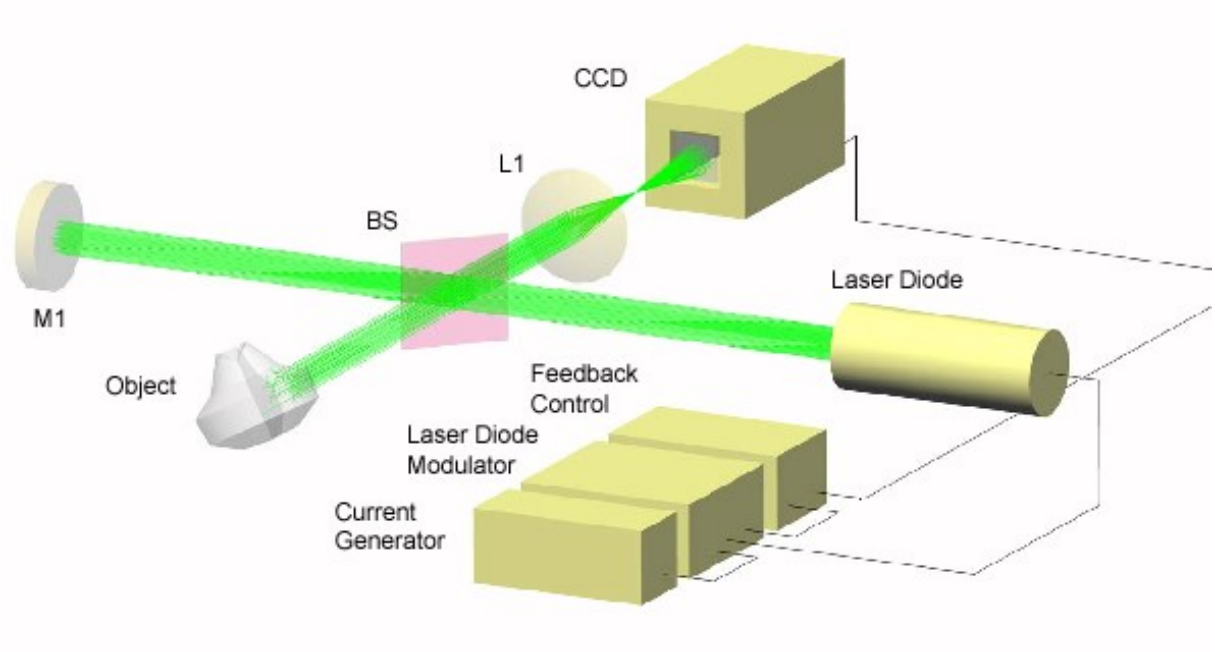

Figure 2.19 – Phase locked laser diode interferometer [29]

Heterodyning, or better still Homodyning since two light beams of different frequencies are derived by a frequency offset process from a single, parent laser beam source in this case, is the use of frequency beats from these two very similar frequencies to determine the phase difference introduced by an object onto one of them. [29]

Therefore, if a frequency difference is introduced between the two beams in an interferometer, the electric fields due to them at any point *P* can be represented by the relations

$$E_1(t) = a_1 \cos(2\pi\nu_1 t + \phi_1) \tag{2.51}$$

And

$$E_2(t) = a_2 \cos(2\pi\nu_2 t + \phi_2) \tag{2.52}$$

Where a_1 and a_2 are the amplitudes, v_1 and v_2 the frequencies, and ϕ_1 and ϕ_2 the phases, relative to the origin, of the two waves at the point *P*. The resultant intensity at *P* is then

$$\begin{aligned} I(t) &= \left[E_1(t) + E_2(t)\right]^2 \\ &= (a_1^2/2) + (a_2^2/2) + (1/2)\left[a_1^2\cos(4\pi\nu_1 t + \phi_1) + a_2^2\cos(4\pi\nu_2 t + \phi_2)\right] \\ &\quad + a_1 a_2\cos\left[2\pi(\nu_1+\nu_2)t + (\phi_1+\phi_2)\right] + a_1 a_2\cos\left[2\pi(\nu_1+\nu_2)t + (\phi_1-\phi_2)\right] \end{aligned} \tag{2.53}$$

The output from a photo detector, which cannot respond to the components at frequencies of $2v_1$, $2v_2$, and $(v_1+ v_2)$ is, therefore,

$$I(t) = I_1 + I_2 + 2(I_1 I_2)^{1/2}\cos\left[2\pi(\nu_1-\nu_2)t + (\phi_1-\phi_2)\right] \tag{2.54}$$

Where $I_1 = (a_1^2/2)$ and $I_2 = (a_2^2/2)$. The phase of the oscillatory component, at the difference frequency $(v_1 - v_2)$, gives the phase difference between the interfering waves at *P*, directly. [15]

2.4 LDV

Laser Doppler Velocimetry, as the name indicates is a method for measuring the velocity of, for example, moving objects or particles. [18]

The laser Doppler technique uses monochromatic laser light as a light source. The interference of two beams crossing in the measurement volume or the interference of two scattering waves on the detector creates a fringe pattern. The velocity information for moving scattering centers is contained in the scattered field due to the Doppler Effect. The laser Doppler technique is an indirect measuring technique, since it measures the velocity of inhomogeneities in the flow, typically tracer particles. This represents the flow velocity only if no appreciable slip velocity is present. Otherwise the slip velocity must also be determined.

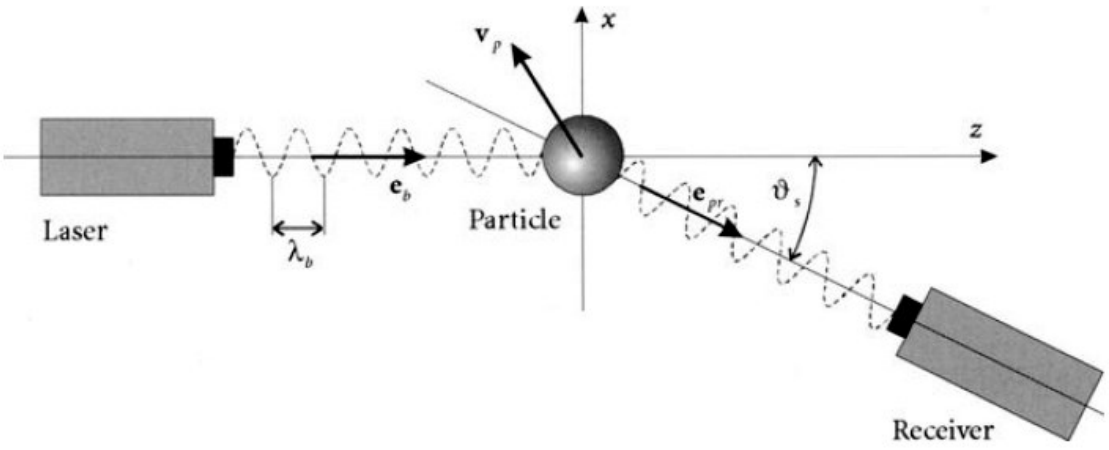

Figure 2.20 – Basic principle of the laser Doppler technique [9]

The basic principle of the laser Doppler technique is illustrated in Figure 2.20. The Doppler effect (in section 2.1) is invoked twice, once when the incident laser light of the transmitter system, characterized by the wavelength λ_b and frequency f_b (subscript b for beam), impinges on the moving target, and once when light with a frequency f_p (subscript p for particle) is scattered from the moving target particle and received by stationary detector with the frequency f_r (subscript r for receiver).

$$
\begin{aligned}
f_r &= f_p \frac{1}{1-\frac{\mathrm{e}_{pr}\cdot \mathrm{v}_p}{c}} = f_b \frac{1-\frac{\mathrm{e}_b\cdot \mathrm{v}_p}{\mathrm{c}}}{1-\frac{\mathrm{e}_{pr}\cdot \mathrm{v}_p}{c}} \\
&\approx f_b + f_b \frac{\mathrm{v}_p\cdot\left(\mathrm{e}_{pr}-\mathrm{e}_b\right)}{c} = f_b + \frac{\mathrm{v}_p\cdot\left(\mathrm{e}_{pr}-\mathrm{e}_b\right)}{\lambda_b} \\
&\left(\left|\mathrm{v}_p\right| << c,\ \ c = f_b\lambda_b\right)
\end{aligned}
\tag{2.55}
$$

Where c is the speed of light in the medium surrounding the particle.

The second term in the second line of equation (2.55) contains the Doppler shift of the incident wave frequency. The difference of the normal vectors appears when the direction of the propagation of the incident and scattered wave differs. The Doppler shift is directly proportional to this difference and to the velocity of the particle. For typical flow systems the Doppler shift is of the order 1 … 100 MHz, which compared to the frequency of laser light of approximately 10^{14} Hz is very small and thus virtually impossible to resolve directly. One exception is a direct detection with the help of an interferometer or through the use of frequency dependent absorption cells, the latter leading to the Doppler global velocimeter (DGV). However, conventional optical arrangements work with two scattered waves, each exhibiting a different Doppler shift. Alternatively one laser beam can act as a reference beam and be mixed with a scattered wave. The two waves are mixed on the detector surface

in a process known as optical heterodyning, yielding the beat frequency, which typically lies in a much more manageable frequency range for signal processing.

There are several alternatives to practically realize such systems using one incident beam, such as, a dual-scattered wave system, Figure 2.21 (a) and one-reference beam, Figure 2.21 (b).

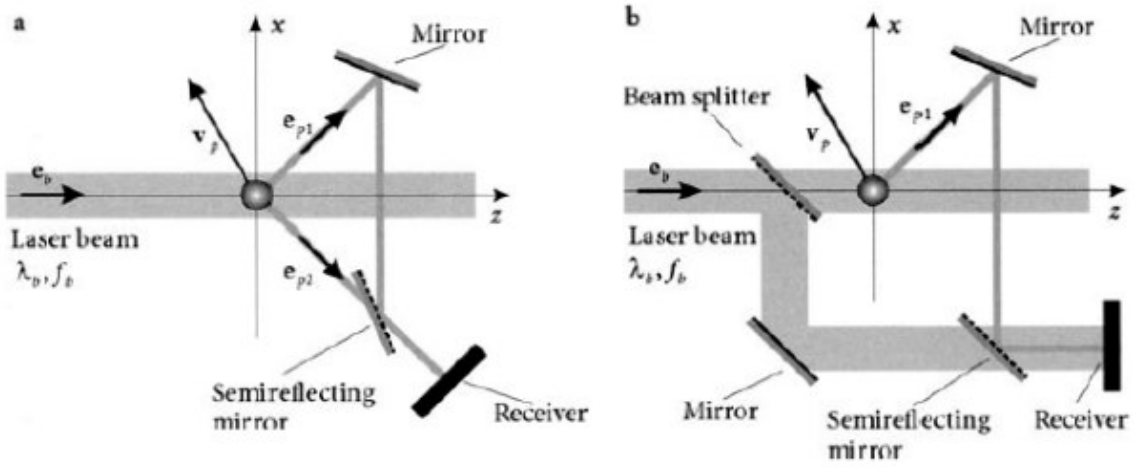

Figure 2.21 – System using one incident beam; (a) Dual-beam scattering configuration; (b) Reference-beam configuration [9]

In both cases the difference (beat) frequency f_d is obtained through the optical mixing of waves with frequencies f_1 and f_2 on the detector. For the one-beam configurations these frequencies are given as

- Dual-scattered-wave configuration (Figure 2.21 (a)):

$$f_1 = f_b + \frac{\mathrm{v}_p \cdot \left(\mathrm{e}_{p1} - \mathrm{e}_b\right)}{\lambda_b}, \qquad f_2 = f_b + \frac{\mathrm{v}_p \cdot \left(\mathrm{e}_{p2} - \mathrm{e}_b\right)}{\lambda_b} \tag{2.56}$$

$$f_D = f_2 - f_1 = \frac{\mathrm{v}_p \cdot \left(\mathrm{e}_{p2} - \mathrm{e}_{p1}\right)}{\lambda_b} \tag{2.57}$$

- Reference-beam configuration (Figure 2.21 (b)):

$$f_1 = f_b + \frac{\mathrm{v}_p \cdot \left(\mathrm{e}_{p1} - \mathrm{e}_b\right)}{\lambda_b}, \qquad f_2 = f_b \tag{2.58}$$

$$f_D = f_2 - f_1 = \frac{\mathrm{v}_p \cdot \left(\mathrm{e}_b - \mathrm{e}_{p1}\right)}{\lambda_b} \tag{2.59}$$

The measurement volume is defined in both cases using an aperture on the detector, thus a virtual measurement volume is realized.

The more widely used optical configuration is based on two incident waves, as illustrated in Figure 2.22.

- In the dual-beam configuration (Figure 2.22 (a)), a real measurement volume is formed at the intersection of the two incident waves and the scattered waves are detected with a single detector:

$$f_1 = f_b + \frac{\mathrm{v}_p \cdot \left(\mathrm{e}_{pr} - \mathrm{e}_1\right)}{\lambda_b}, \qquad f_2 = f_b + \frac{\mathrm{v}_p \cdot \left(\mathrm{e}_{pr} - \mathrm{e}_2\right)}{\lambda_b} \tag{2.60}$$

$$f_D = f_2 - f_1 = \frac{\mathrm{v}_p \cdot \left(\mathrm{e}_1 - \mathrm{e}_2\right)}{\lambda_b} \tag{2.61}$$

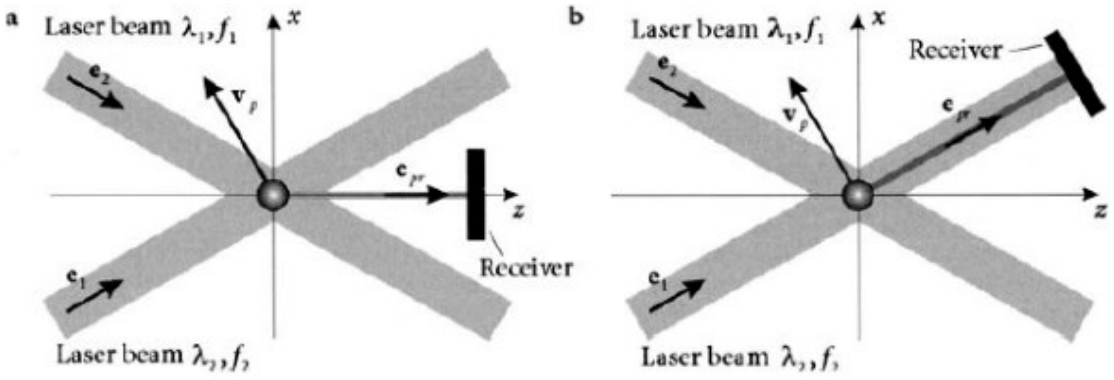

Figure 2.22 – Optical configuration for two incident waves; (a) dual-beam configuration; (b) reference-beam configuration [9]

- In the reference-beam configuration (Figure 2.22 (b)), the detector is positioned directly in the path of one of the beams $\left(e_{pr} = e_2\right)$. Typically the incident reference beam is much lower in intensity than the incident scattering beam. This configuration is seldom used; however, it does show some advantages for measurements in highly absorbing media.

$$f_1 = f_b, \qquad f_2 = f_b + \frac{\mathrm{v}_p \cdot \left(\mathrm{e}_{pr} - \mathrm{e}_2\right)}{\lambda_b}, \qquad \mathrm{e}_{pr} = \mathrm{e}_1 \tag{2.62}$$

$$f_D = f_2 - f_1 = \frac{\mathrm{v}_p \cdot \left(\mathrm{e}_1 - \mathrm{e}_2\right)}{\lambda_b} \tag{2.63}$$

The difference frequency is independent of the receiver position for the dual-beam configurations in Figure 2.22.

The flow direction α is measured with respect to the perpendicular of the beam bisector. Thus the frequency difference is linearly proportional to the velocity component in the x direction, denoted by $v_{p\perp}$ or v_{px}.

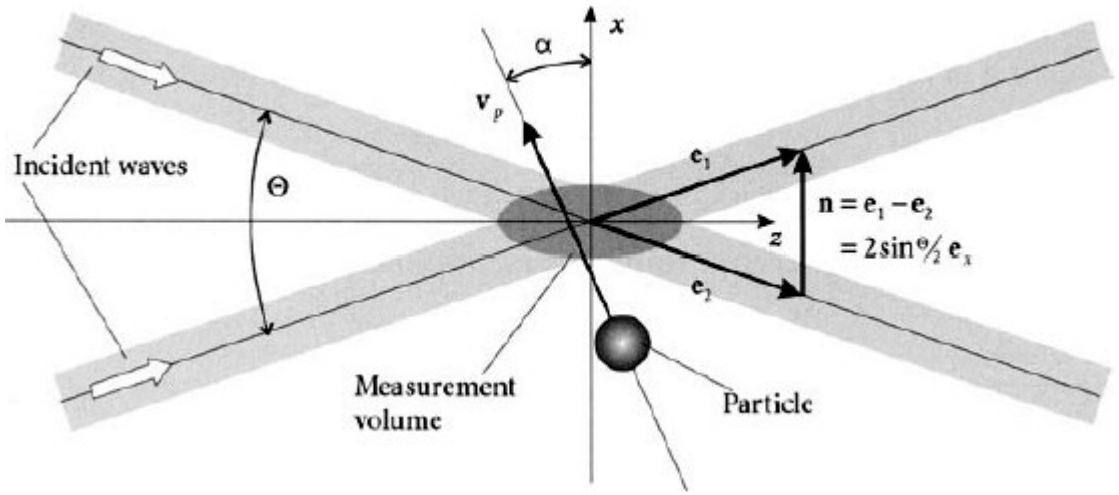

Figure 2.23 – Vector relations relevant to determining the Doppler frequency [9]

For very small tracer particles, the very illustrative fringe model can be used to explain the measurement principle of the laser Doppler technique. This model is based on the spatial energy density in the measurement volume.

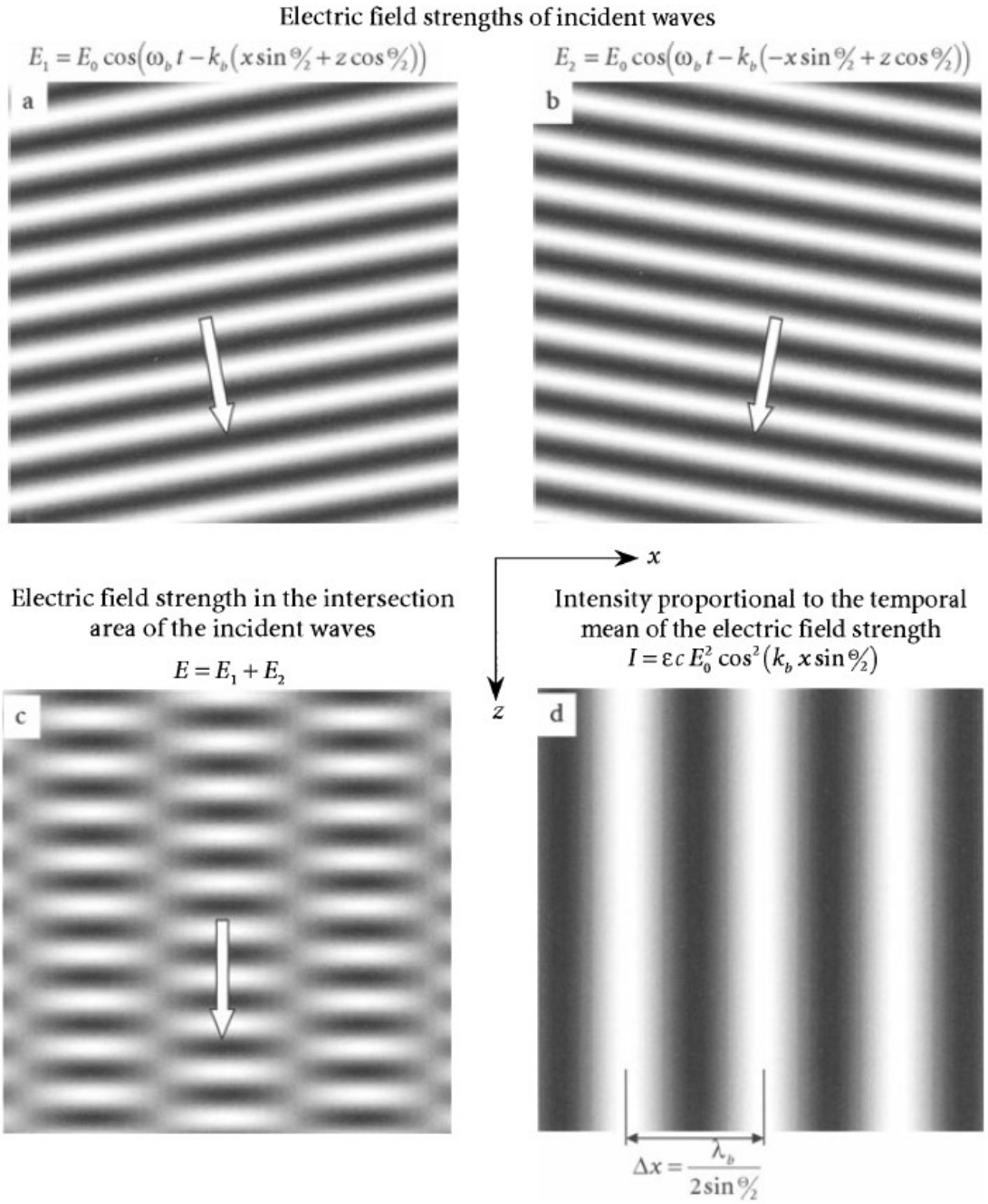

Figure 2.24 – Generation of the interference structure of two homogenous waves. (a) (b) Electric field strength of incident waves; (c) Superposition of electric fields; (d) Intensity [9]

The spatial dependence of the intensity in the intersection volume can be interpreted as an interference field with fringes parallel to the y-z plane (Figure 2.24). The fringe spacing is given by:

$$\Delta x = \frac{\lambda_b}{2 \sin \Theta/2} \tag{2.64}$$

This interference or fringe model of the laser Doppler technique is strictly only valid for very small particles fulfilling the condition $d_p \ll \lambda_b$, since only then can the amplitude and phase, or intensity of the field be considered constant over the particle diameter.

For particles larger than the wavelength of light this model fails. Both the amplitude and phase of the incident waves vary across the diameter of the particle.

Only certain areas of the particle surface are involved in defining signal properties. The position and size of the receiving aperture define the position and size of these interaction areas. The area of the first interaction with the field is known as the "incident point" and the source area of the scattered wave is called "glare point", Figure 2.25. The size of the incident areas/"points" and glare areas/"points" is proportional to the size of the detection aperture.

The scattered waves detected by the receiver each have an amplitude, which depends on the position of their glare points.

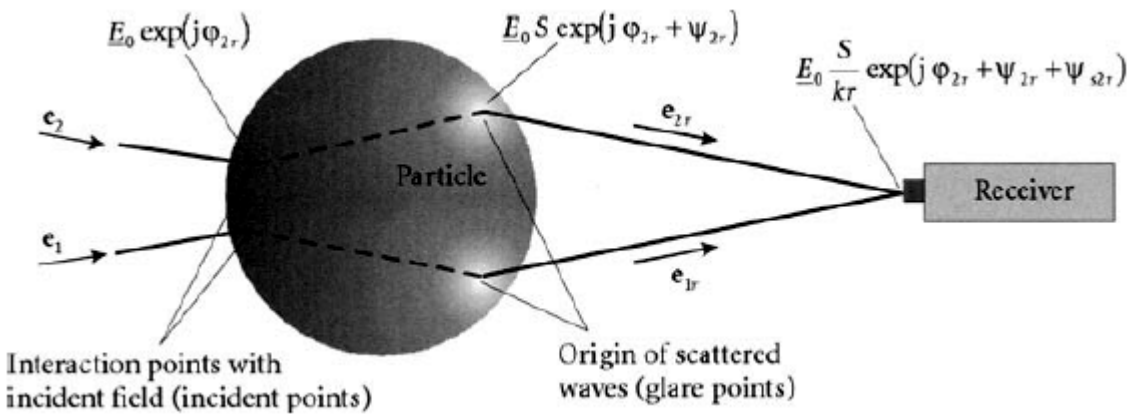

Figure 2.25 – Signal origin for large particles [9]

A conventional laser Doppler optical arrangement is summarized in Figure 2.26. The laser beam is split into two beams of equal intensity and polarization using a beam splitter and brought to intersection with a lens. A collimator is used for adjusting the beam properties in the measurement volume and the Bragg cell provides a frequency shift used for directional sensitivity. The Doppler frequency is determined using a signal processor and the data analysis for computing flow properties is performed in a computer.

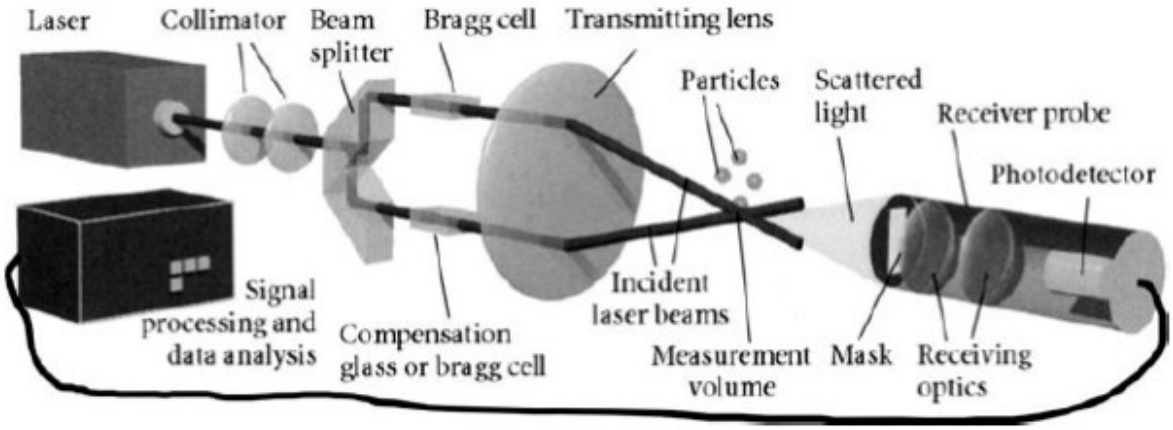

Figure 2.26 – Dual-beam laser Doppler Velocimetry [9]

The laser Doppler technique samples the flow velocity at discrete times corresponding to the passage of a particle through the intersection volume. [9]

2.5 PDV

Photon Doppler Velocimetry is a heterodyne velocimeter technique based on the the LDV, where the frequency of the Doppler-shifted light provides a direct measure of the instantaneous velocity of a moving target illuminated by a laser. With the developments in telecommunications technologies, the Lawrence Livermore National Laboratory (LLNL) developed a novel fiber-optic approach LDV as a diagnostic for high explosive tests. This technique is able to measure surface velocities ranging from centimeters per second to kilometers per second.

The technique uses multi-mode fiber optics operating at 1550 nm, along with many high-bandwidth electrical components. The choice of a wavelength which is popular in telecommunications, serves both the necessity of working with a rather large wavelength and the low cost of the required components. As a Michelson interferometer counts fringes for measuring distances with $\Delta x = n\lambda/2$, the measured velocities obey the relation $V = F\lambda/2$. As such, an object moving at 1 km/s will exhibit a frequency of approximately 1.29 GHz, already rather high. Smaller wavelengths would require even higher frequency detection bandwidths, and necessarily more expensive detection equipment. Figure 2.27 shows the basics of the photonic Doppler Velocimetry system.

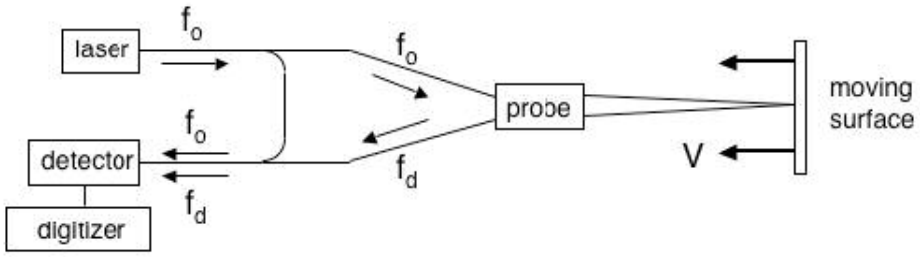

Figure 2.27 – Basic block diagram of the photonic Doppler Velocimetry system [30]

A laser-generated optical carrier propagates through a multi-mode fiber to a probe lens. The probe illuminates the target with the optical carrier. As the target moves towards the lens, the reflected light is Doppler-shifted. The probe lens collects a portion of the Doppler-shifted light and the light propagates back through the multi-mode fiber. The Doppler-shifted light is mixed with a fraction of the original optical carrier in a fiber-optic coupler as is detected by an optical detector. The detector generates as electrical current proportional to the square of the optical fields that, for the Doppler-shifted light, corresponds to a beat frequency proportional to the instantaneous velocity of the target.

According to Figure 2.27, the frequency of the light emitted by the laser is f_0, and the frequency of the Doppler-shifted light is f_d. The beat signal is generated at the detector with a frequency f_b equal to the difference between the Doppler-shifted frequency f_d and the un-shifted frequency f_0, and it's given by:

$$f_b = f_d - f_0 = 2(v/c)f_0 \tag{2.65}$$

With the speed of light $c = f_0\lambda_0$ where λ_0 is the wavelength emitted by the laser and the velocity is given by:

$$V = f_b \cdot \frac{\lambda_0}{2} \tag{2.66}$$

David B. Holtkamp, from Los Alamos National Laboratory, describes a PDV as a very fast Michelson interferometer, as shown in Figure 2.28. In this new configuration of PDV, instead of using a beam splitter like in Michelson interferometer, PDV uses a fiber optical circulator.

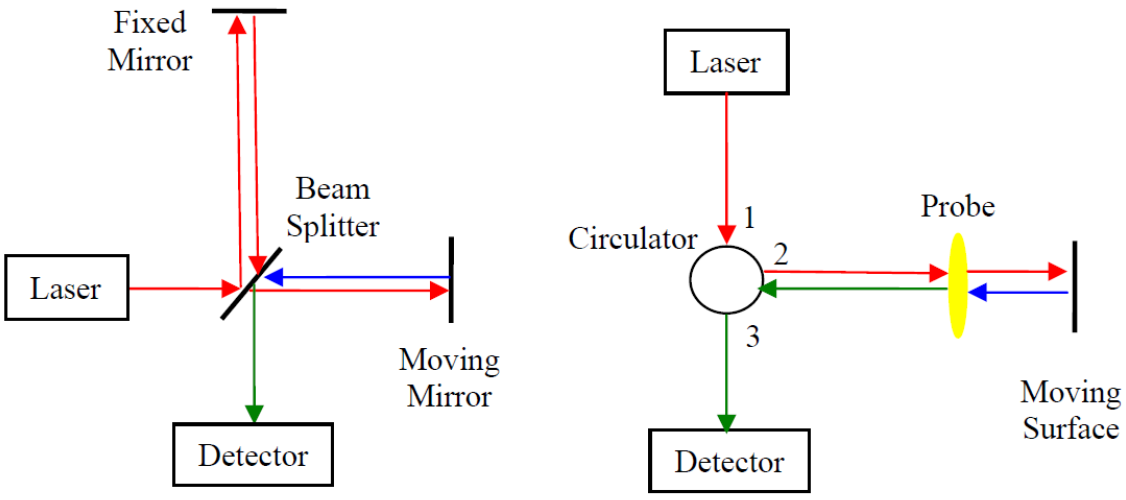

Figure 2.28 – Michelson interferometer VS simplified schematic of PDV [31]

Both the Michelson as in PDV, there are produced fringes that track the motion of the moving mirror. In the case of the Michelson interferometer, the displacement, Δx, is proportional to the number of fringes, n, and the wavelength of the laser using the expression $\Delta x = n \cdot \lambda/2$.

For PDV, the interest is on the velocity of the moving surface that is given by equation (2.66)

According to Oliver T. Strand from LLNL and also Holtkamp [31], the heart of both designs of PDV is the 3-port circulator. The operating principle of the circulator is simple to understand. Basically, the light injected in port 1 will be emitted out port 2, and the light that comes back into port 2 will be emitted out port 3. The fiber connects the laser, the probe and the detector to the circulator, respectively.

Although not as obvious as in the Michelson interferometer, the light that goes out through port 2 is recombined or interferes with the back-reflection at the optical probe, after having travelled to the moving object. Therefore, the light that comes back into port 2 bears a Doppler Shift relative to the incoming laser light and it is this frequency-shifted radiation that finally exits through port 3 into the photo-detector.

The other two main components from telecommunication industry are the fiber laser and a digitizing oscilloscope. These lasers are simple to operate, compact and emit cw radiation. The new class of digitizing scopes also presents very large bandwidths, very high sampling rates and large amounts of memory. The PDV developed by LLNL is shown in Figure 2.29, with all its the components.

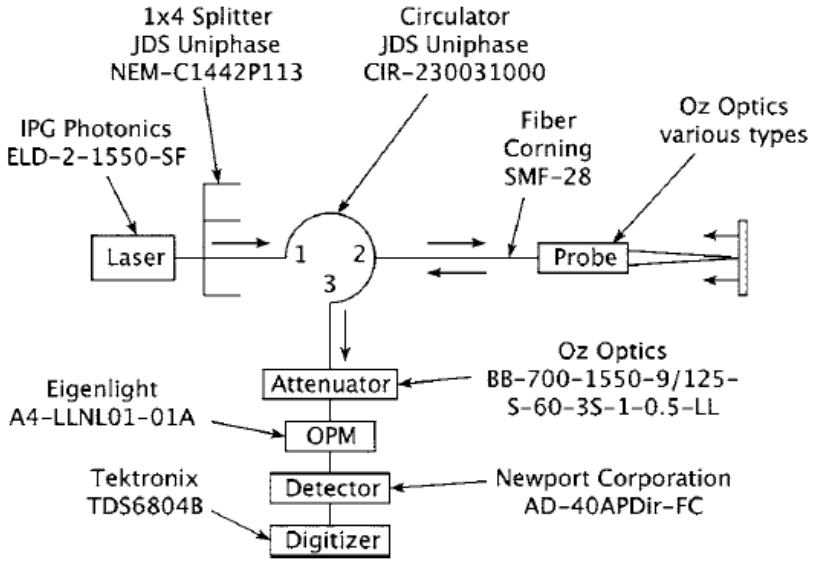

Figure 2.29 – Components used in PDV [24]

This equipment is durable, relatively inexpensive and easy to use, and data analysis can be performed rapidly. The maximum velocity is limited by the bandwidth of the electronics and the sampling rate of the digitizers.

The heterodyne system responds to the absolute value of the beat frequency, and it can't make the difference between a surface moving toward or away from the probe, what can make this method less useful in applications where the absolute position of the surface must be followed.

There are advantages and disadvantages on using this technique, the advantages significantly out-weighting the disadvantages. One of the main advantages is the fact that the beat frequency is lower for a given velocity than it would be using visible light lasers, and one chief disadvantage of operating this king of lasers (1550 nm) is the fact that the laser radiation cannot be seen with the unaided eye therefore, some practical issues of performing probe alignments with respect to the target surface are difficult to circumvent. [5, 6, 24, 30-32]

2.6 Fourier transform

A very large class of important computational problems falls under the general rubric *Fourier transform methods* or *spectral methods*. For some of the problems, the Fourier transform is just an efficient computational tool for accomplishing certain common manipulations of data. In other cases, there are problems for which the Fourier transform is itself of intrinsic interest.

A physical process can be described either in the *time domain*, by the values of some quantity *h* as a function of time *t*, e.g., *h(t)*, or else in the *frequency domain*, where the process is specified by giving

its amplitude *H* as a function of frequency *f*, that is, *H(f)*, with $-\infty < f < \infty$. For many purposes it is useful to think of *h(t)* and *H(f)* as being two different *representations* of the same function. One goes back and forth between these two representations by means of the *Fourier transform* equations,

$$H(f) = \int_{-\infty}^{\infty} h(t) e^{2\pi i f t} dt$$
$$h(t) = \int_{-\infty}^{\infty} H(f) e^{-2\pi i f t} df \quad \textbf{(2.67)}$$

If *t* is measured in seconds, then *f* in Eq. (2.67) is measured in cycles per second, or Hertz. However, the equations work with other units, too. If *h* is a function of position *x* (in meters), *H* will be a function representing inverse wavelength or spatial frequency, in cycles per meter, and so on.

From Eq. (2.67) it is evident at once that Fourier transformation is a *linear* operation. The transform of the sum of two functions is equal to the sum of the transforms. The transform of a constant times a function is that same constant times the transform of the function.

In the time domain, the function *h(t)* may happen to have one or more special symmetries. It might be *purely real* or *purely imaginary* or it might be *even*, $h(t) = h(-t)$, or *odd*, $h(t) = -h(-t)$. In the frequency domain, these symmetries lead to relationships between *H(f)* and *H(-f)*.

Some other elementary properties of the Fourier transform are shown below, where the "↔" symbol indicates transform pairs. Some of the most common pairs are:

$$h(t) \leftrightarrow H(f) \quad \textbf{(2.68)}$$

$$h(at) \leftrightarrow \frac{1}{|a|} H\left(\frac{f}{a}\right) \quad \text{Time scaling} \quad \textbf{(2.69)}$$

$$\frac{1}{|b|} h\left(\frac{t}{b}\right) \leftrightarrow H(bf) \quad \text{Frequency scaling} \quad \textbf{(2.70)}$$

$$h(t - t_0) \leftrightarrow H(f) e^{2\pi i f t_0} \quad \text{Time shifting} \quad \textbf{(2.71)}$$

$$h(t) e^{-2\pi i f_0 t} \leftrightarrow H(f - f_0) \quad \text{Frequency shifting} \quad \textbf{(2.72)}$$

With two functions *h(t)* and *g(t)*, and their corresponding Fourier transforms *H(f)* and *G(f)*, it is possible to form combinations of special interest. The *convolution* of the two functions, denoted $g * h$, is defined by

$$g * h \equiv \int_{-\infty}^{\infty} g(t) h(t - \tau) d\tau \quad \textbf{(2.73)}$$

A special result called the *convolution theorem*, states that the Fourier transform of the convolution is just the product of the individual Fourier transforms.

The *correlation* of two functions, denoted Corr(*g*, *h*), is defined by

$$\mathrm{Corr}(g,h) \equiv \int_{-\infty}^{\infty} g(\tau + t)h(\tau)d\tau \tag{2.74}$$

The correlation is a function of *t*, which is called the *lag*. It therefore lies in the time domain, and it turns out to be one member of the transform pair:

$$\mathrm{Corr}(g,h) \leftrightarrow G(f)H*(f) \tag{2.75}$$

This result shows that multiplying the Fourier transform of one function by the complex conjugate of the Fourier transform of the other gives the Fourier transform of their correlation.

The *total power* in a signal is the same whether is computed in time or in frequency domain. This result is known as *Parseval's theorem*:

$$total\ \ power \equiv \int_{-\infty}^{\infty} |h(t)|^2 dt = \int_{-\infty}^{\infty} |H(f)|^2 df \tag{2.76}$$

The Fourier Transform therefore is the tool used in spectral analysis. Several examples of its application to signals acquired in the course of the experimental work can be seen in Chapter 4 on Data Analysis. [33]

2.7 Split Hopkinson Pressure Bar

Nowadays there are several engineering applications where the impact velocity is important, so, it is important to proper understand the materials behavior under dynamic deformations.

For a dynamic characterization of materials, there are several methods currently available.[4]

The Split Hopkinson Pressure Bar or Kolsky bar is the most convenient system for characterizing high strain-rate behavior of materials. This technique was developed by Hopkinson and later by Kolsky, originally for compression tests, now adapted to tensile tests. [34]

The Hopkinson bar used in the project has been applied to perform high speed tensile tests. As the scheme in Figure 2.30 shows, this configuration is composed by two bars, an input and output bar, an impactor that is struck in one end of the input bar and finally the specimen, which is positioned between the input and the output bars.

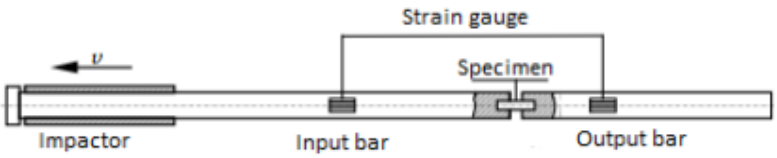

Figure 2.30 – Scheme of a split Hopkinson pressure bar for tensile tests [35]

The impact caused at the far end of the input bar generates a stress-wave that propagates along the bar. When this wave reaches the specimen its deformation starts and afterwards, the transmitted wave propagates into the output bar while the reflected wave propagates back into the input bar. These three waves are measured using strain gages that are placed in the bars on a specific place. Assuming then that force equilibrium exists between the two sides of the specimen, the stress, strain and strain rate can be calculated.[35, 36]

2.8 Electromagnetic forming

Electromagnetic forming is one of the High Speed Metal Forming techniques. The process basically consists of a capacitor bank, a forming coil and a workpiece to be deformed, preferably made of a material with high electrical conductivity, and it is based on the discharge of a significant quantity of energy in an extremely short time.

This technique uses pulsed magnetic fields to apply forces to the metal workpiece.

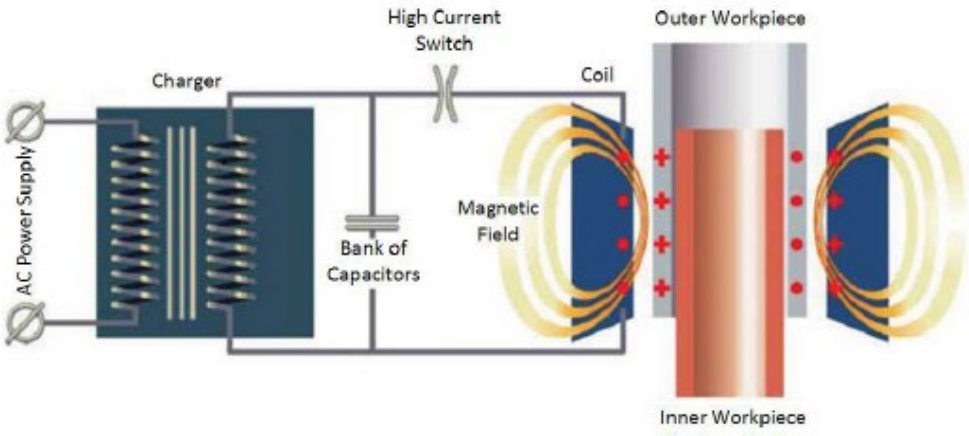

Figure 2.31 – Scheme of Electromagnetic Forming process [7]

The energy required to the deformation of the workpiece is secured by the capacitor bank that is connected to the process actuator. When the main switch is closed, a high current pulse is discharged by the capacitor bank into the forming coil. This results in a strong transient magnetic field developed

in the coil, which induces a current into the workpiece with the opposite direction to the current that creates it. This induced current inside the workpiece is responsible for the creation of the workpiece magnetic field. As two opposite magnetic fields repel each other, it leads to the workpiece movement and quick deformation.[37].

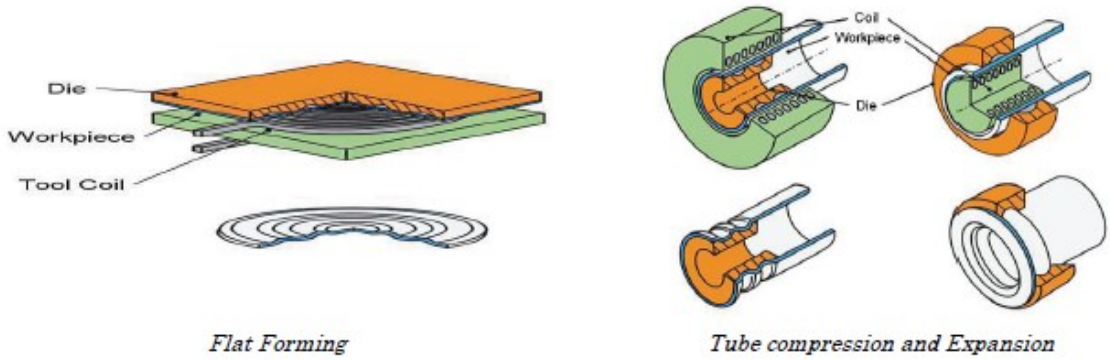

Figure 2.32 – Example of coil types commonly used on electromagnetic forming [7]

Different applications of electromagnetic forming can be conceived, depending on the setup and geometry of the coil and workpiece. Also, with some arrangement parameters adaptations, this magnetic pulse technology can have other applications like welding, joining, crimping or cutting. This process involves strain rates of 3500 s^{-1} and velocities of 250-300 m/s.

This process has many advantages that make it an attractive alternative to the conventional forming processes. Some of the advantages are high productivity, increase on formability, environmentally friendliness, springback and wrinkling reduction, among many others. Such as the other processes, electromagnetic forming also has some disadvantages or limitations, such as, the necessity of high safety precautions, the limitation on the suitable materials, the application limitation to simple shapes and so on. [7]

3 EXPERIMENTAL WORK

In this section, all steps taken in support of the objective of measuring velocities with a laser will be described. The initial work served essentially the purpose of getting acquainted with the equipment available in LOME and grasping the rationale behind the world of Optics and Optical Metrology.

The experimental work therefore began by building a Mach-Zehnder interferometer. This configuration is important for obtaining interference fringes rapidly and introducing the researcher to the data analysis of the acquired fringes.

After obtaining the first interference fringes, a Michelson interferometer was assembled, as it basically works according to the principle of the LDV and after PDV that were envisioned for later deployment. With a Michelson interferometer it is already possible to measure object velocities, starting with slow velocities with the Michelson configuration deployed on an active stability control Optical Table and then gradually increasing the velocities and the confidence on the configured interferometer up until being able to perform measurements on the Kolsky bar to measure the velocity of its input bar.

The laser used during this experimental work was a Nd:YVO4 laser with a wavelength of $\lambda = 532\ nm$ and approximate intensity of 100 mW.

3.1 The Mach-Zehnder Interferometer

The first configuration adopted for the Mach-Zehnder interferometer has the scheme shown in Figure 3.1. This configuration is composed by two mirrors, M1 and M2, and beamsplitters BS1 and BS2. This first configuration was assembled with the purpose of detecting the fringes created by the interference of the beams and therefore getting acquainted with the basic principles of interferometry. Interference is obtained when the beams, originally separated at BS1, are combined at a later stage on BS2, after travelling different paths.

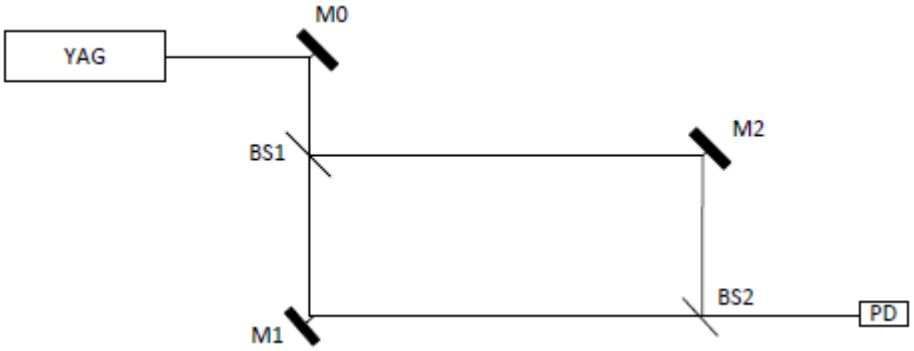

Figure 3.1 – Mach-Zehnder scheme 1

This configuration was assembled on an optical table inside LOME, to expedite component alignment and prevent vibration problems, which plague interferometer assemblies. Figure 3.2 shows the assembly of a Mach-Zehnder interferometer in LOME.

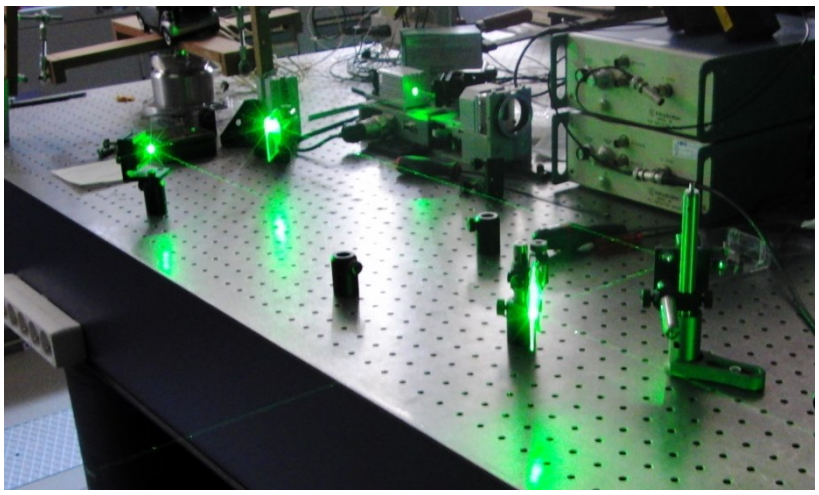

Figure 3.2 – Assembly of Mach-Zehnder scheme 1

Following assembly and alignment of the interferometer, it was readily possible to observe interference fringes movement whenever one of the light paths where changed, even by such small amounts as those obtained by slightly pushing against an optical component such as a mirror.

To control the frequency through the two different paths, one acousto-optic modulator (AOM) was introduced on each of the paths to impose different frequency shifts in each arm of the Mach-Zehnder. The AOMs used in this work are AOD-70 from IntraAction Corp and provide a frequency sweep from 50 to 90 MHz. The signal detected from the PD was sent to an oscilloscope with a bandwidth of 100MHz.

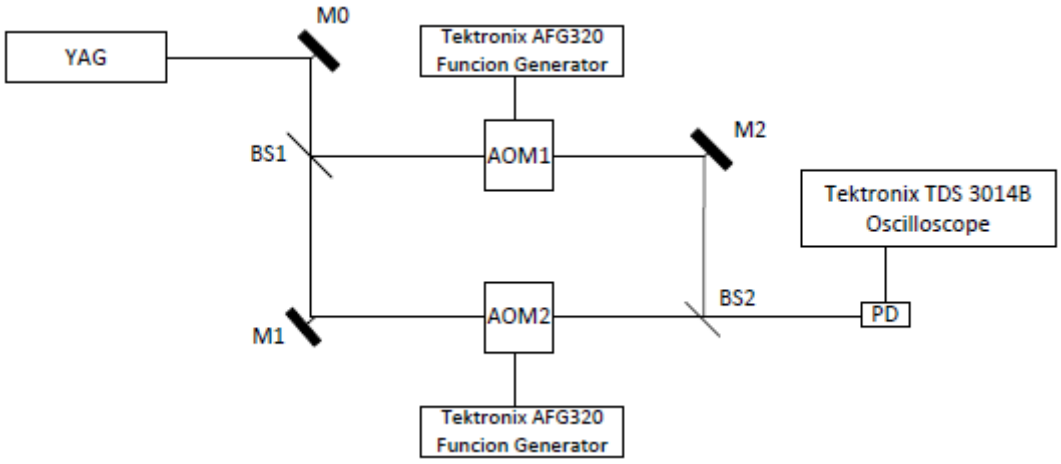

Figure 3.3 – Mach-Zehnder scheme 2

With the function generator coupled to the acousto-optic, it was possible to set the frequency to a specified value in order to simulate the shifted frequencies such that the signals faithfully resembled those obtained from objects moving at different velocities. In Figure 3.4, the assembly for this configuration can be seen.

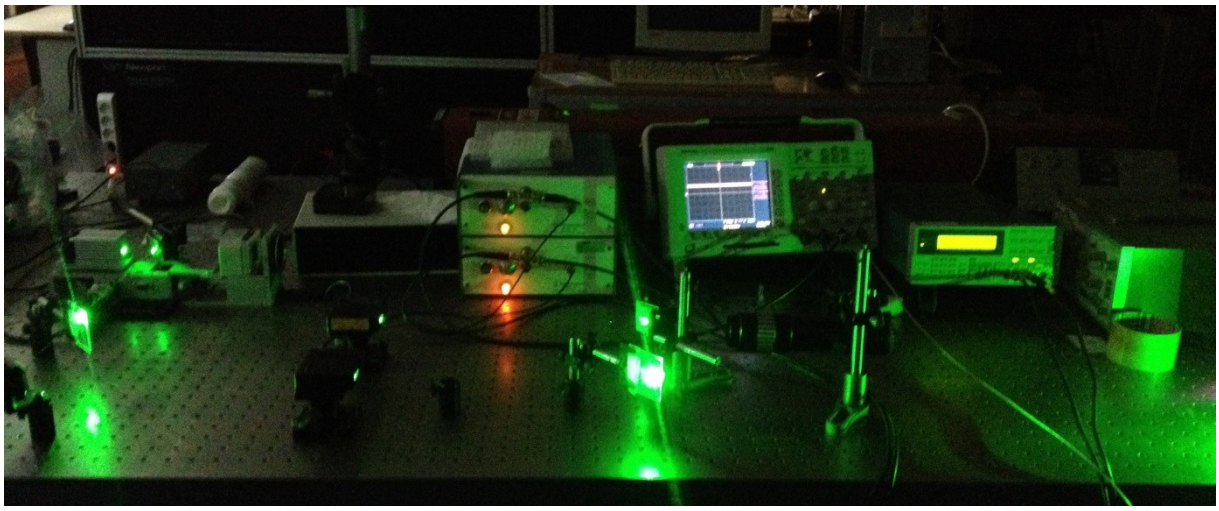

Figure 3.4 – Assembly of Mach-Zehnder scheme 2

Figure 3.5 shows the result obtained from the shifted light, where is possible to see the first and second order diffracted beams. The signal input to the PD was referred to the first diffracted order. In this figure it wasn't possible to verify the fringes on unaided eye, due to the very high intensity of the laser beam.

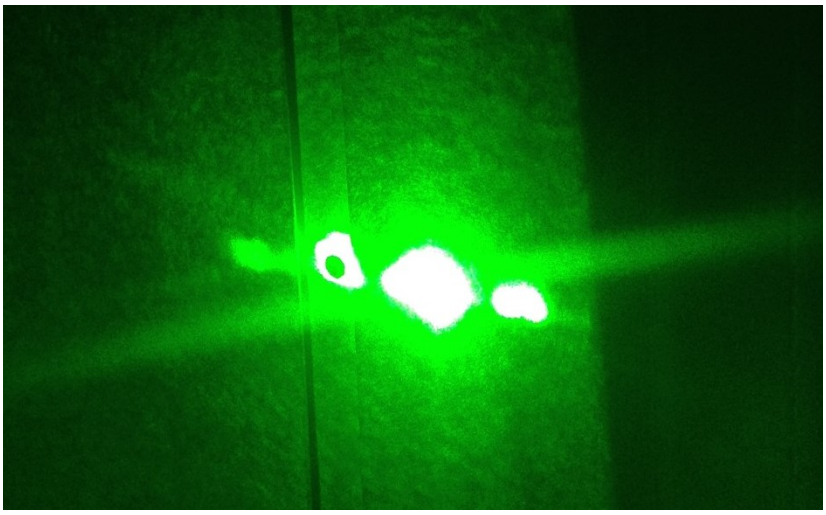

Figure 3.5 – Diffracted beams from Mach-Zehnder scheme 2

The output signal observed in the oscilloscope, that was obtained from the PD, presented too much noise and very was clearly inconstant. Due to such bad results, an analysis of the components was started to find out where the noise was originated and

It was concluded that it was due to a bad performance from the acousto-optic modulators that could not set the frequency input imposed by the function generator. The observed intensities of the beams coming out of the modulators were also appreciably different from each other.

The oscilloscope available in LOME was also not performant enough for detecting such high frequencies.

The experimental results from this initial interferometer assembly were therefore compromised by several equipment related problems and were not as satisfactory as expected, albeit the assemblies having been done and measurements taken, which were really the main purpose of this introductory stage of the experimental work.

3.2 LDV

The LDV built for this work was based on the Michelson interferometer. This configuration was composed by four mirrors, where two of them were used to direct the laser beam to BS1. The M2 is fixed and the M3 is set on a driver controlled by a micro-control and it moves forward and backward with different velocities.

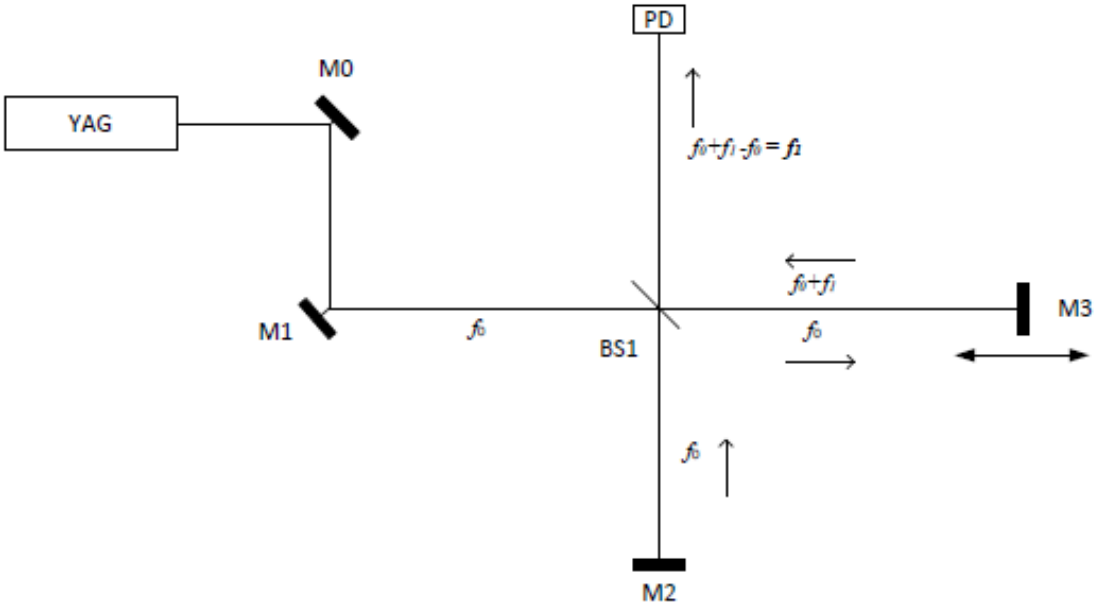

Figure 3.6 – LDV scheme 1

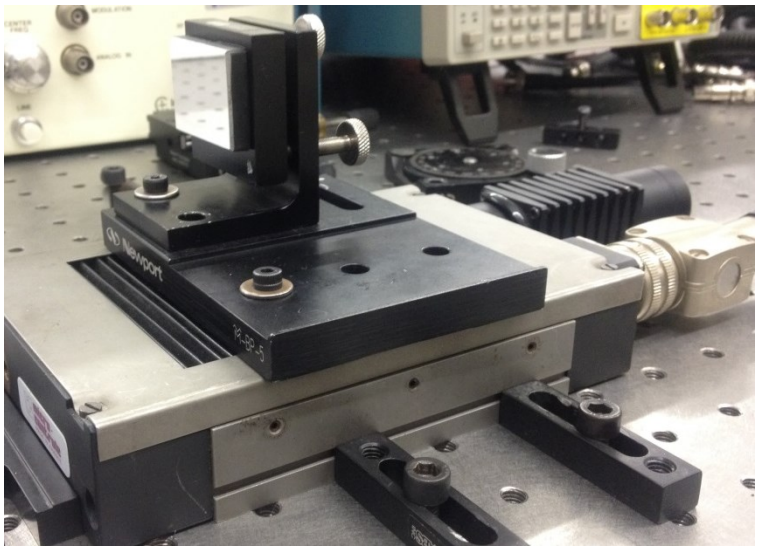

Figure 3.7 – M3 and driver from micro-positioner

After the alignment of the interferometer, it was possible to see some fringes of interference. These fringes were detected by the PD with a signal output very clean and constant. Then it were tested the different velocities of the micro-controller.

The micro-controller positioner used in this work was one from Micro-Controle Electronique model TL 78-3. This positioner has three different velocities. To determine the different velocities, it was measured the time that the controller take to travel a specific length for each one, and ten measurements forward and ten backward were made and the average velocity was therefore determined. In Annex C all the measurements made for each velocity are shown and in Table 3.1 is

the velocities of the micro-controller and the respective expected frequencies can be observed. The frequencies were obtained according to Equation (2.66).

Table 3.1 – Velocities from micro-positioner and respective expected frequency

	Forward	Backward	
Low Velocity			
Velocity Ave.	0.02800	0.02799	mm/s
Frequency	105.28	105.22	Hz
Normal Velocity			
Velocity Ave.	0.26000	0.26066	mm/s
Frequency	977.44	979.92	Hz
High Velocity			
Velocity Ave.	2.34836	2.37756	mm/s
Frequency	8828.44	8938.18	Hz

Figure 3.8 show the final assembly of the LDV with the configuration of a Michelson Interferometer where the beamsplitter in the middle, the fixed mirror, M2, the moving mirror, M3, and the PD on the left side of the picture can all be observed.

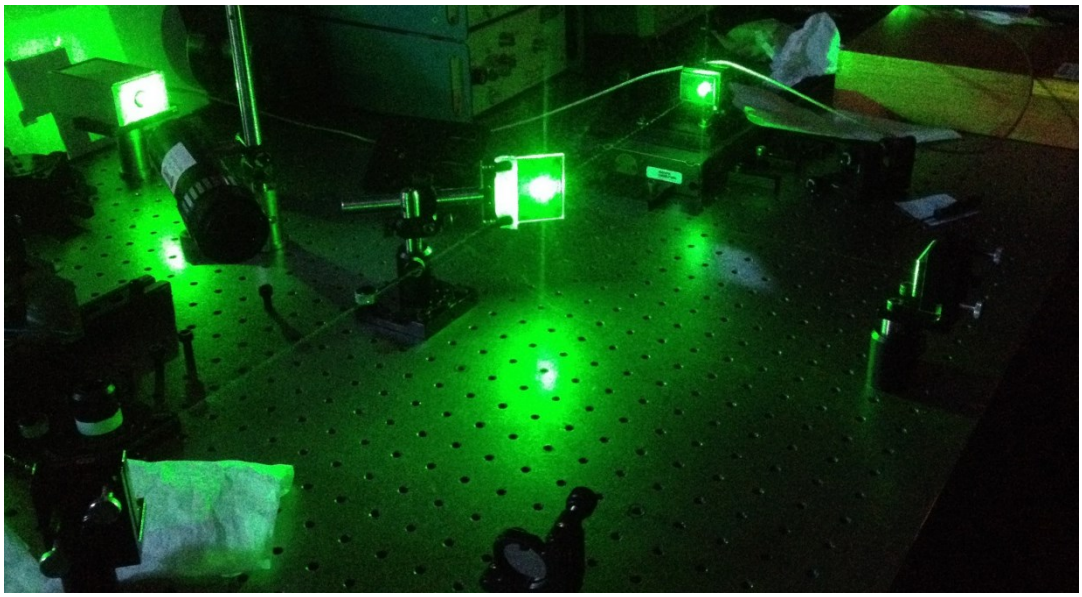

Figure 3.8 – Assembly of LDV scheme 1

Figure 3.9 shows the signal obtained from the PD equivalent of the normal speed on the Tektronix oscilloscope. The frequency for each speed could be measured at the oscilloscope directly.

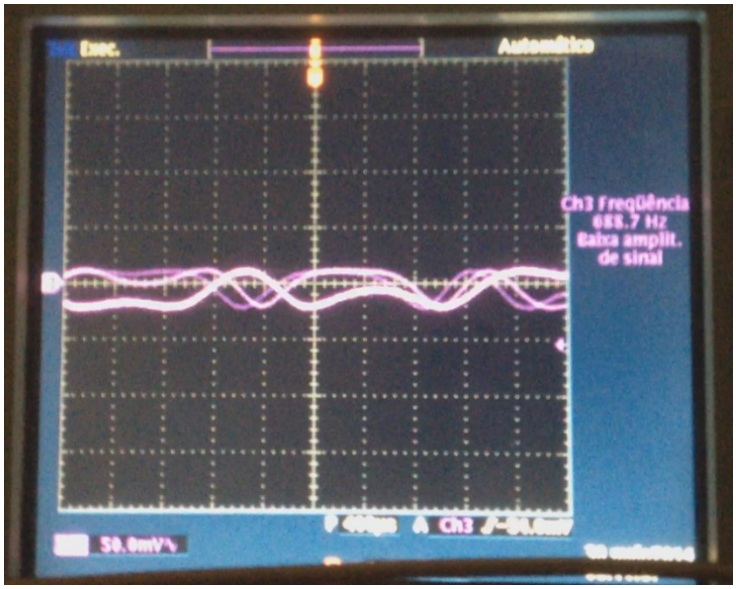

Figure 3.9 – Signal from the PD for normal speed

A slightly different configuration with an expanded beam for better fringe discrimination can be seen in Figure 3.10. The beam was expanded with a collimator, thoroughly described in Chapter 2, that enables observation of the quasi-circled fringes, shown in Figure 3.11.

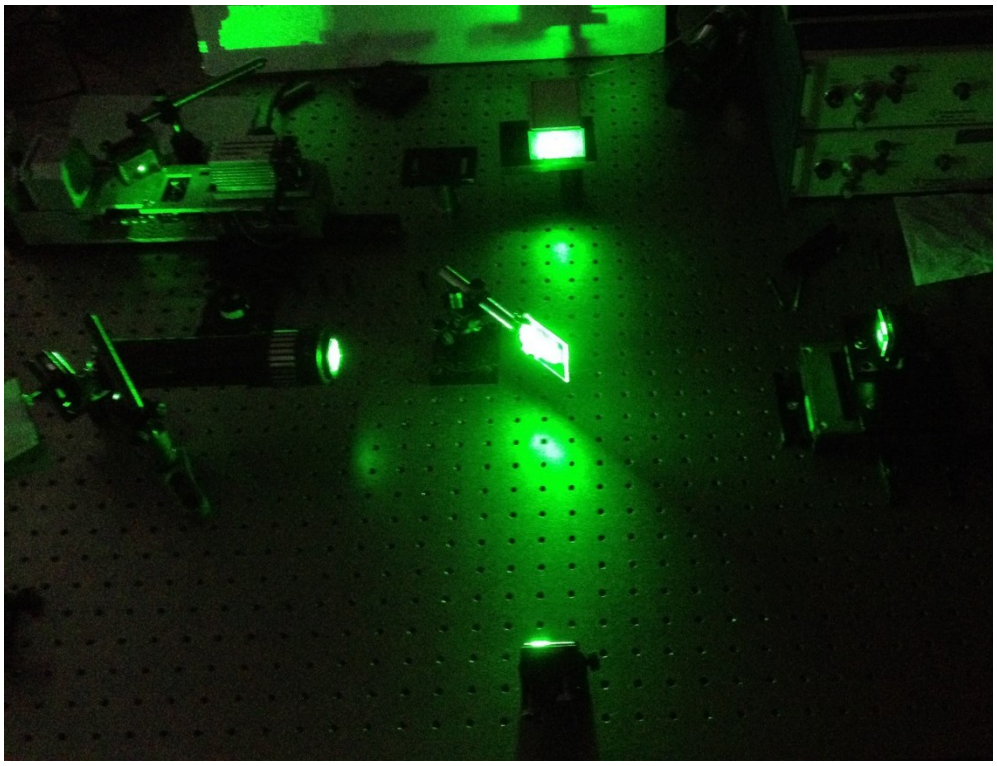

Figure 3.10 – Assembly of LDV scheme 2 with collimator

The fringes shown in Figure 3.11 appear in the center and according to the imposed velocity at the mirror, travel to the border until they disappear. The frequency of these fringes is therefore related to the velocity from M3 as expected.

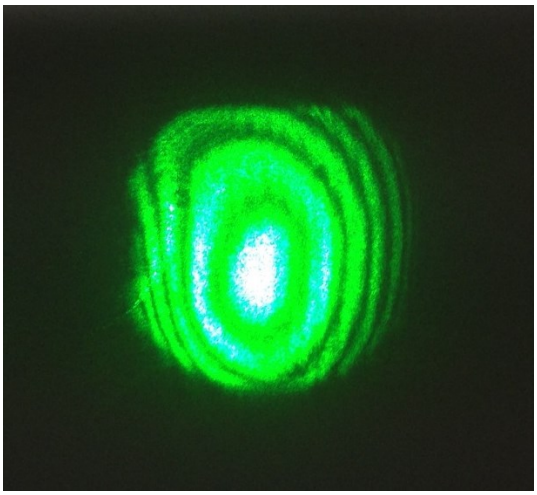

Figure 3.11 – Fringes obtained with the collimator

In Figure 3.12 is possible to understand how the PD detects the fringes.

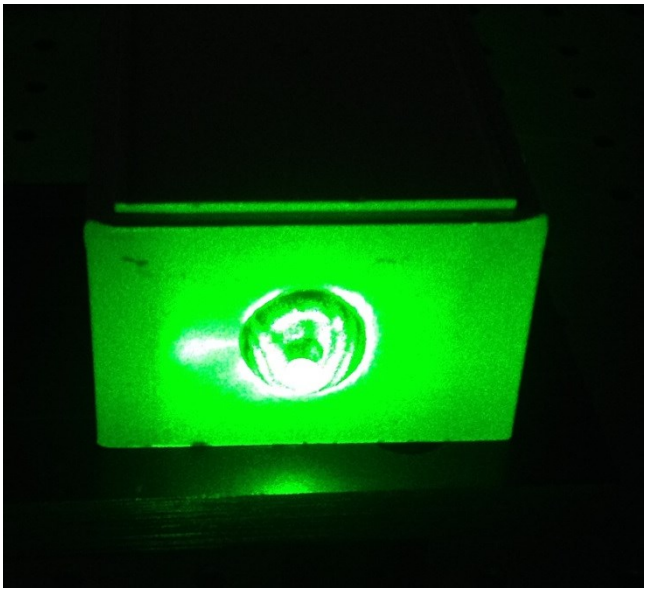

Figure 3.12 – Fringes observed by the PD

3.3 PDV

After making all the measurements with micro-positioner, a way to adapt a PDV to the Hopkinson Bar with the aim to measure velocities in the range of m/s, i.e. between 5 and 10 m/s, was finally devised.

As referred in the section 2.5, a PDV is composed by an optical fiber laser, a circulator, a probe, a detector, an amplifier and an oscilloscope. The components chosen for this scheme were dimensioned to measure velocities around 300 ms^{-1} during the ring expansion in electromagnetic forming. Since the PDV is only limited by the bandwidth of the electrical components, the first component to be dimensioned is the oscilloscope. Through Eq. (2.66) and for V=400 ms^{-1} it is necessary an oscilloscope that can acquire a range of frequencies up to 516 MHz. The chosen oscilloscope was a RIGOL DS6102 with a 1GHz bandwidth.

Table 3.2 – Specifications from oscilloscope

Specifications	RIGOL DS6102
Analog BW	1 GHz
Channels	2
Max. Sample Rate	5 GSa/s
Real time waveform Record	Max. 200000 frames

The fiber laser used is from QPHOTONICS with a wavelength of λ=1550 nm and is composed by the laser diode and it respective controller. The laser diode has the following specifications:

Table 3.3 – Specifications of laser diode driver

Laser diode driver unit with temperature controller	
Maximum operating current	300 mA
PD current range	0,01 – 5 mA
Supply voltage	110 VAC/ 230 VAC
Power consumption	< 40 W

Due to the fact that the laser diode has a very low power, there is a need to couple an amplifier module to amplify the signal from the laser beam that goes to the detector, in order to increase the range of the detection area. The amplifier selected is from NUPHOTON Technologies and was a C-band 0.5 W EDFA Module with the reference EDFA-CW-HP-C0-RS-27-20-FCA. Although the amplifier has been selected, it did not arrive in time to be used in this PDV assembly, so that it will not be taken into account for the results obtained. As such, the selection of the electrical components for the PDV assembly, is as shown in Figure 3.13.

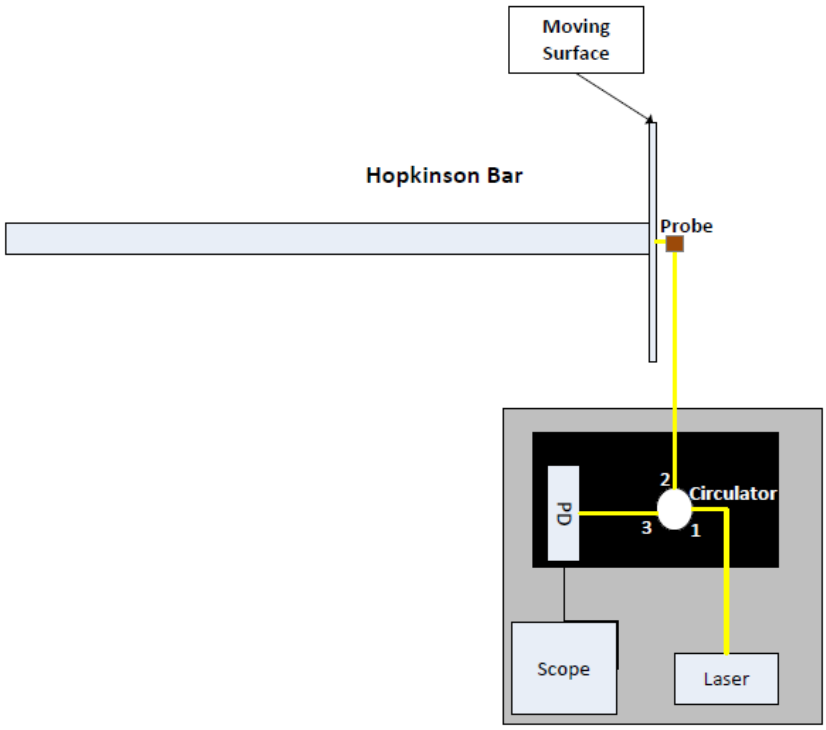

Figure 3.13 – Scheme of the PDV applied in Hopkinson bar

The optical components such as the optical fibers, connectors, circulator and detector were kindly offered by Geoffrey Taber from Ohio State University, who has a large experience in setting-up PDV's and was therefore involved in the choice of components. Table 3.4 shows the specifications of all components.

Table 3.4 – Specifications of the optical components

Optical Circulator	
Operating wavelength	1550 ± 30 nm
Connector	FC/APC
Probe	
Wavelength	1550 ± 30 nm
Working Distance	20 mm
Connection	LC/APC
Connector	
Connection	FC/APC – LC/APC
Detector	
Wavelength range	850 – 1700 nm
Bandwidth	5 GHz
Recommended Maximum Output (50 Ω)	1 V
Input	FC/PC Fiber Connector

The final assembly of the PDV is shown in Figure 3.14, where it is possible to identify the circulator and the respective input and output's, the probe and detector, and the connectors to adapt the circulator to the probe, since that it has different type connections.

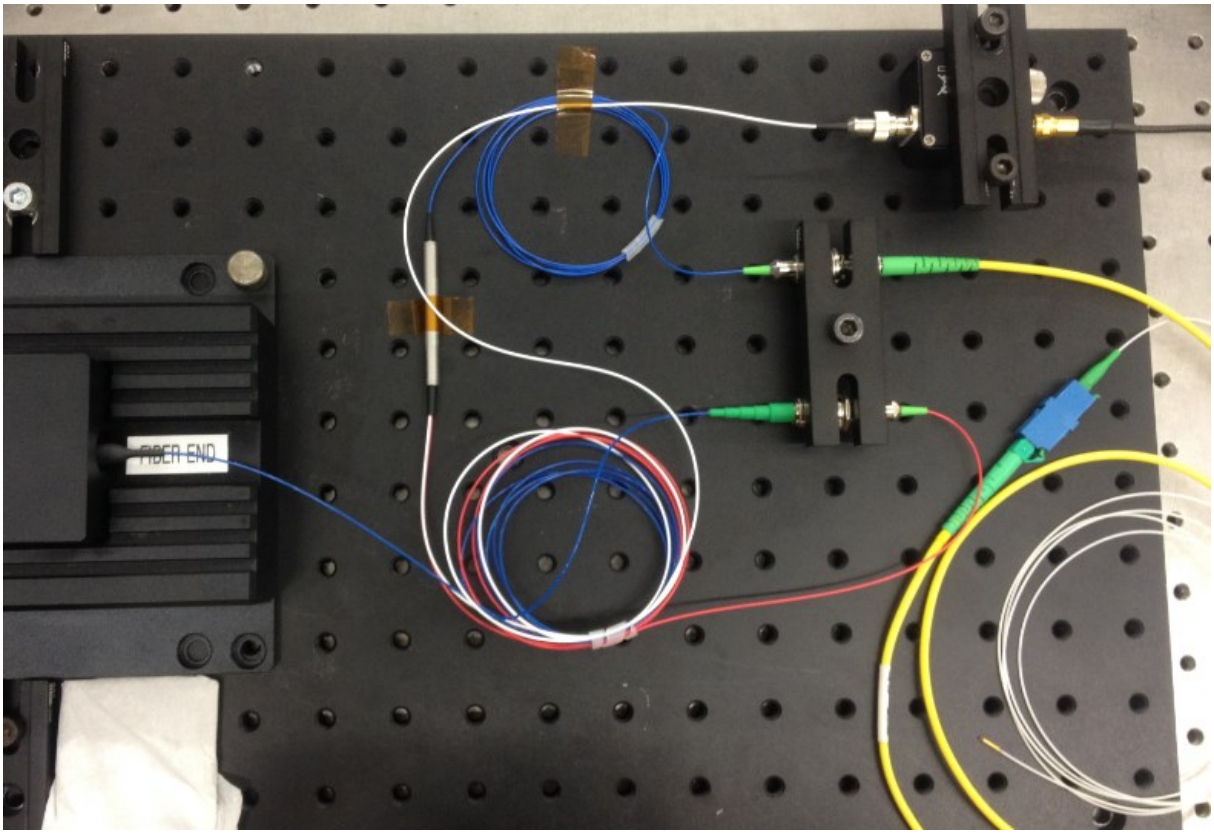

Figure 3.14 – Assembly of the PDV

In the following figures all the important components of the PDV are shown in detail.

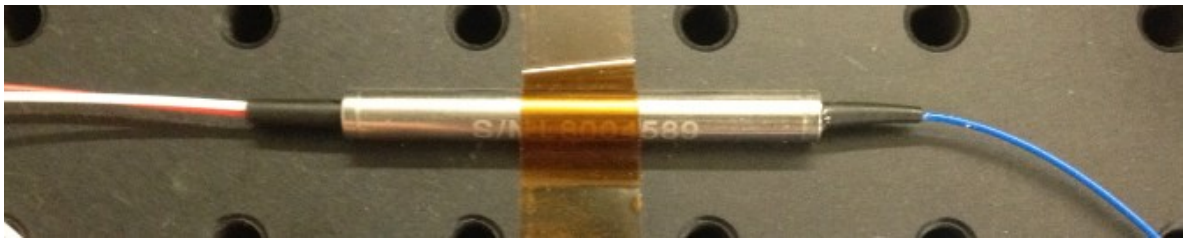

Figure 3.15 – Detail of the circulator

Figure 3.15 shows in detail the circulator used in the assembly. In this circulator, port 1 is the red fiber and is the input of the laser diode. Port 2 is the blue one and is where the signal comes out to the probe and comes back whit the shifted signal. Finally port 3 corresponds to the white fiber shown in the figure and connects to the detector.

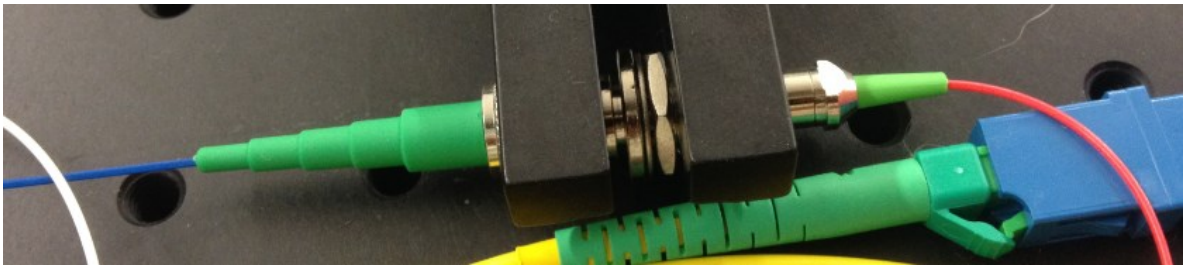

Figure 3.16 – Detail of the connection between laser diode and circulator

In Figure 3.16 it is possible to see the connection between the laser diode and the circulator where the blue fiber corresponds to the laser and the red corresponds to the port 1 of the circulator.

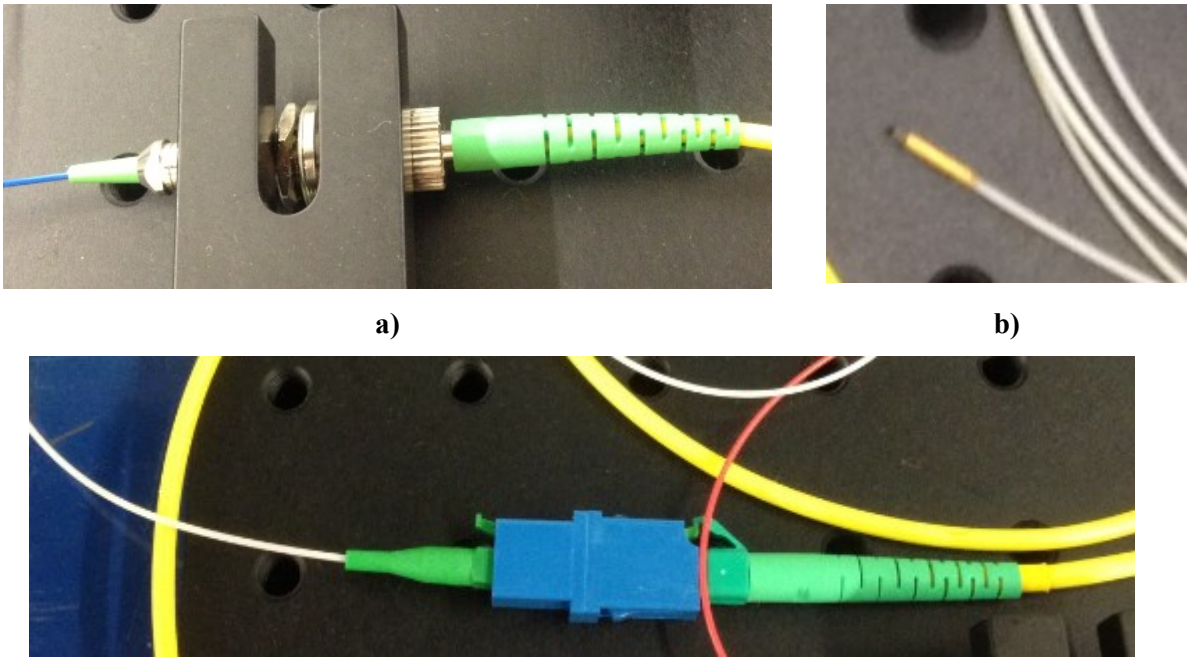

a) **b)**

c)

Figure 3.17 – Details of the probe and respective connections

Figure 3.17 shows all the connections and the used probe. According to Table 3.4, the probe uses a LC connector and the circulator use a FC connector, so there is the need to use a connector, in Figure 3.17 a) it is possible to understand the connection between the circulator, which corresponds to the blue fiber, and the connector which corresponds to the yellow wire. Figure 3.17 c) shows the connection between the connector and the probe, where the yellow wire is the connector and the white corresponds to the probe. Finally in Figure 3.17 b) a detail of the probe can be seen.

Figure 3.18 – Detail of the detector

Finally in the Figure 3.18 it is possible to observe the detector used in this PDV where the white fiber connects from port 3 from the circulator.

The PDV was then adapted to the Hopkinson bar. To do such, there was the need to make a reflective surface to measure the signal as it drove away from the probe with the input bar. The small plate adapted to the bar is shown in Figure 3.19 a).

a) **b)**

Figure 3.19 – Moving surface adapted for Hopkinson Bar

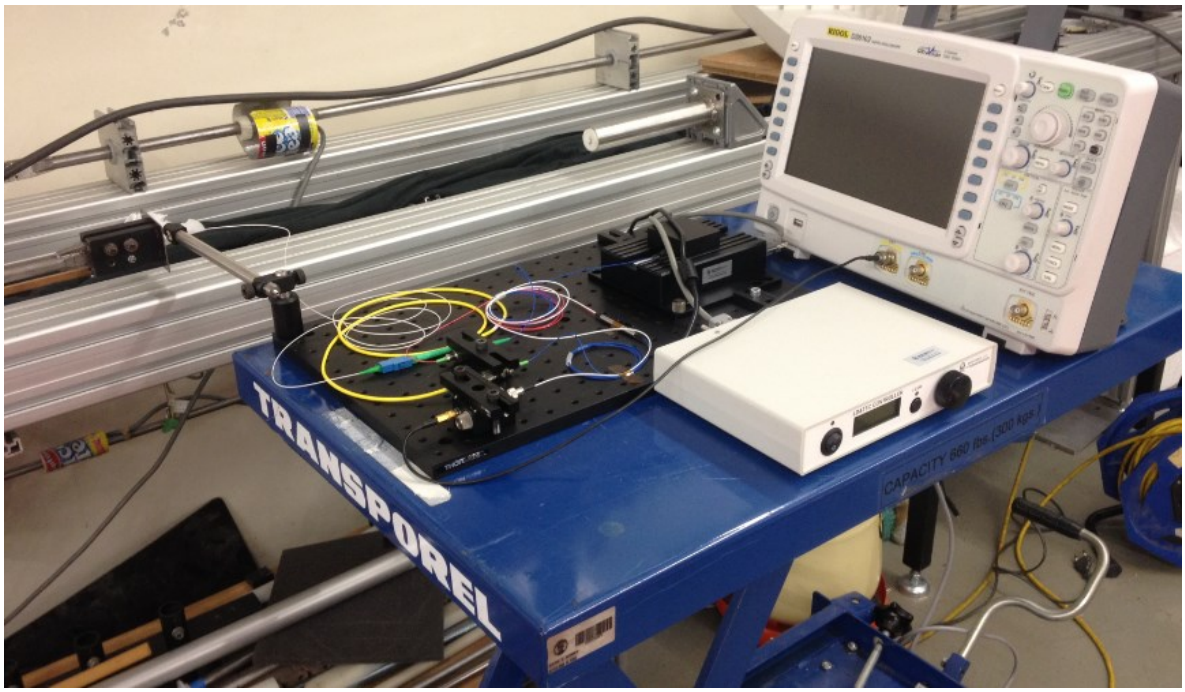

Figure 3.20 – Final assembly of PDV in the Hopkinson bar

In the Figure 3.20 it is possible to observe how the adaptation of the PDV was made in the Hopkinson. This assembly already shows the detector connected to the oscilloscope and the laser diode controller. There was the need to make a support for the probe to set and align it. The Figure 3.21 shows the detail of the support for the probe.

Figure 3.21 a) b) and d) show in detail different views of how the probe is set in the Hopkinson bar. While the measurement of the velocity of the bar, require the probe to lie much closer to the reflective plate, in the photos shown below the probe is distant from the bar to better understand the assembly. In Figure 3.21 c) the support made for the probe is shown in more detail.

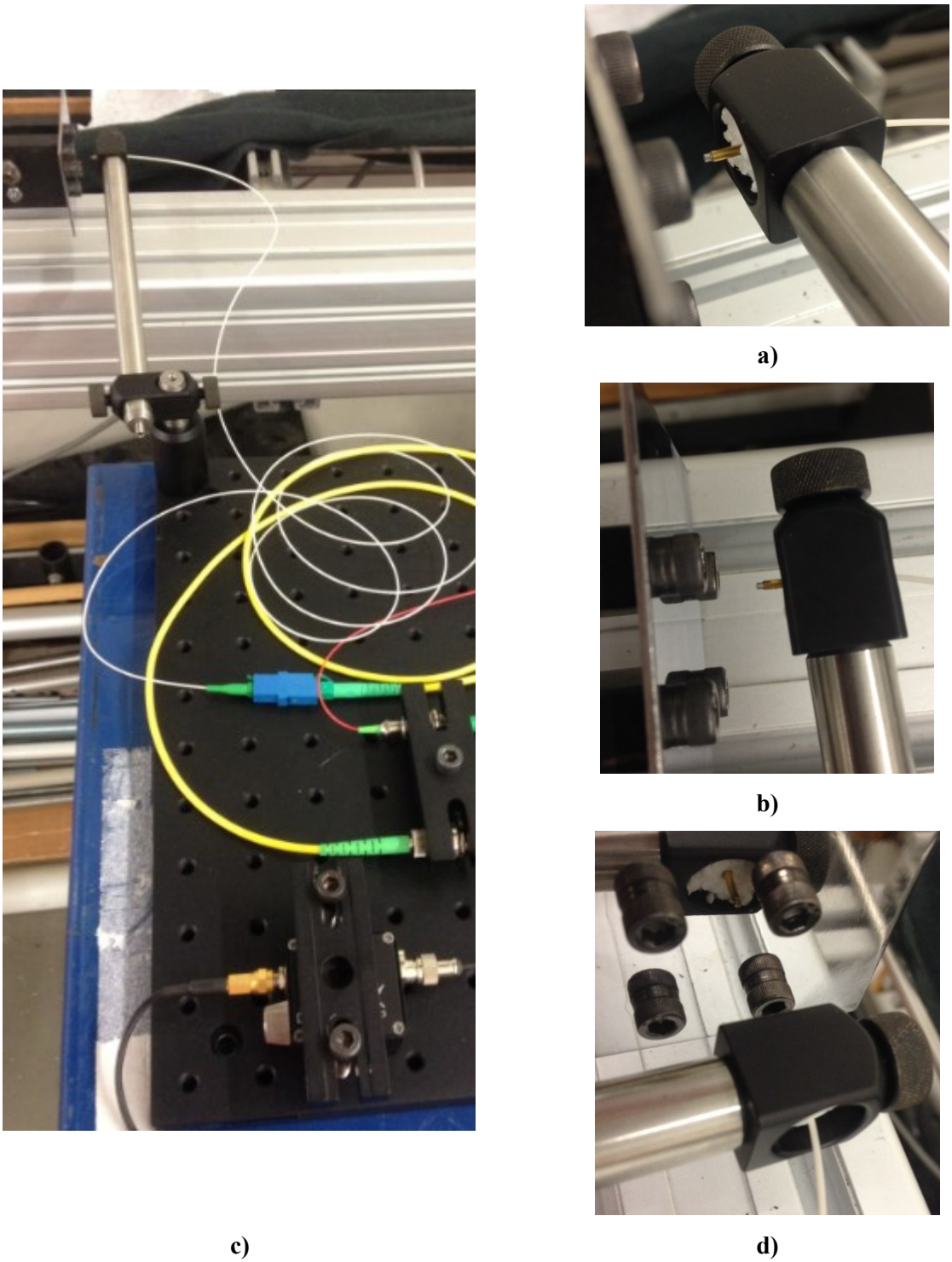

a)

b)

c)

d)

Figure 3.21 – Details of the adaptation of the PDV in the Hopkinson bar

4 DATA ANALYSIS

Data acquisition was made with two different devices, depending on each setup. For the setup assembled in the Optical Table, LDV, Figure 3.8, data acquisition was performed with an acquisition module from National Instruments, model NI 9234 and for the PDV assembled in the Hopkinson bar was used the two channel RIGOL oscilloscope DS6102.

a) **b)**

Figure 4.1 – a) Acquisition module NI 9234; b) Digital Oscilloscope Rigol DS6102

Is this chapter the data acquisition and analysis obtained from the LDV is discussed. A Matlab® code implementation of the Fast Fourier Transform (FFT) and spectral analysis with a Short Time Fourier Transform (STFT) was developed expressly for this analysis.

4.1 Matlab® Code

The output files from the acquisition module and oscilloscope are saved in TXT format, that contain the time and voltage values referred to the observed movement.

This program is able to open the TXT files and create a graphic from those values (V(t)), then calculate a FFT to show the range of frequencies that occur in the captured signal. It also calculates a STFT according to the respective V(t). In this STFT, a graphic is created where it is possible to observe the frequencies and velocities along the time axis, i.e., to observe when each different frequency occurred in the signal.

Although it's a simple program, it has some functionalities and parameters that have to be explained so to easy understand how it really works. In summary, it can be said that the program uses three main functions from Matlab® Toolbox, the FFT, the STFT and *spectrogram*. These functions use the referred Fourier Transform equations that can be analyzed in details in the book *Numerical Recipes [33]*

4.2 Results from LDV

In this part it will be analyzed and discussed the results obtained from the LDV scheme 1 and 2 and for the various velocities from the micro-positioner.

4.2.1 LDV results for Low speed

First the signals obtained from the forward and backward movement will be compared, without filters. According to these results the filters used for this velocity will be defined.

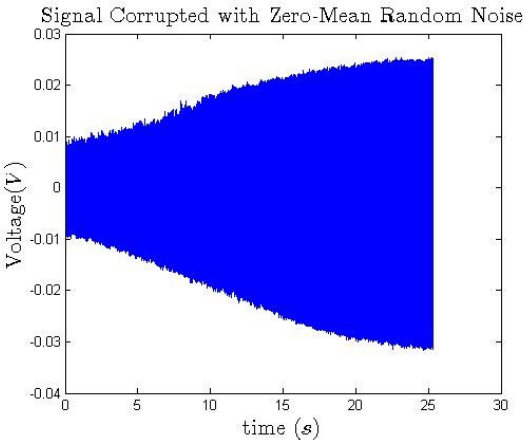

a1)

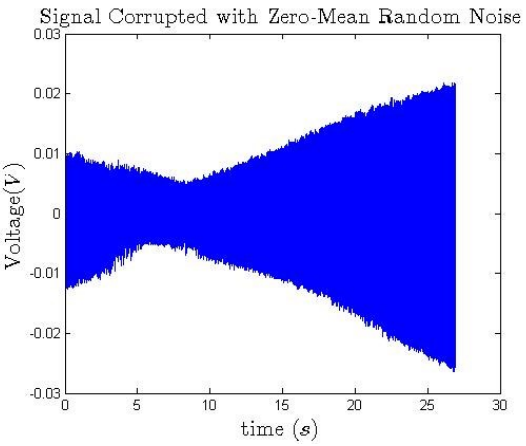

b1)

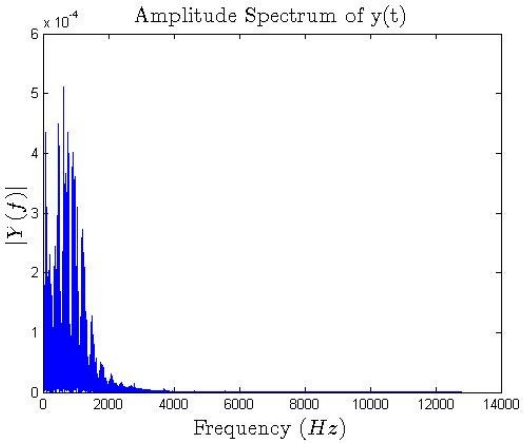

a2)

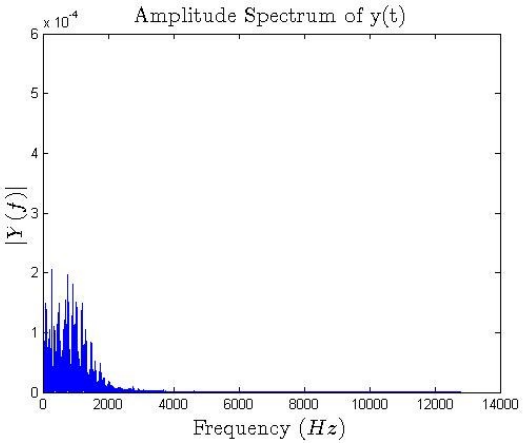

b2)

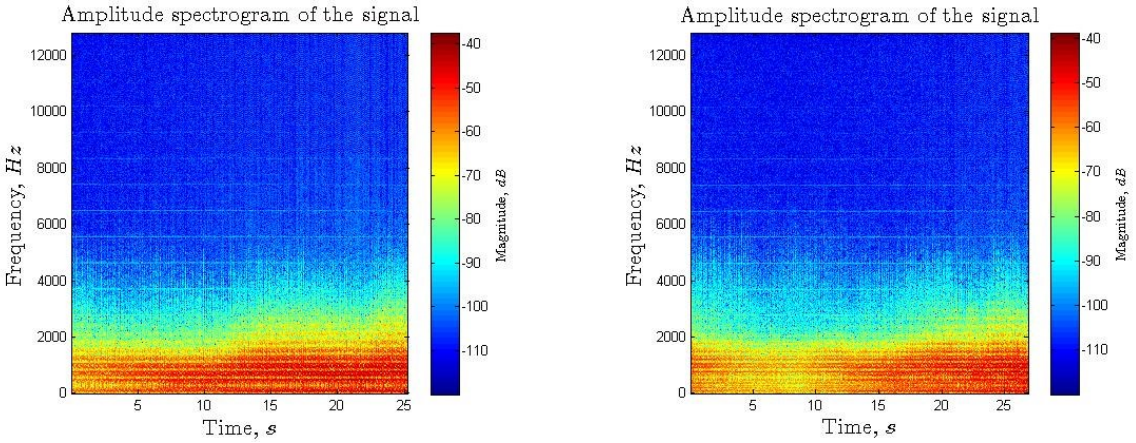

a3) **b3)**

Graphic 4.1 – Signal results from Low speed, (a) forward and (b) backward

Graphic 4.1 a1) and b1) show the raw signal from the PD, where it is possible to observe a difference between the amplitudes of the forward and backward movements. This difference is due to the fact that the measurements were made in different start and ending positions and is caused by the intensity of the laser and the inclination of the fringe pattern.

Graphic 4.1 a2) and b2) shows the FFT of the respective raw signal which displays the frequencies range directly related to the velocity. Since the low speed is 0,028 mm/s (approx.) and according to Table 3.1 the expected frequency is around 105 Hz, it can be seen that the values shown in these graphics are not as expected. The range of frequencies shown, are placed between 0 and 2000 Hz. These values could be easily justified due to the noise that results from the experiment. Some sources of that noise can be exposed, such as the PD, the daylight, the cables, the very high sensitivity of the Michelson, the temperature variations, etc. To decrease this unwanted noise, the option was made to create a band-pass filter, specific for this velocity, with a range between 50 and 150 Hz.

Graphic 4.1 a3) and b3) show the frequency range along the time axis, using a Gabor or STFT Transform. For this particular signal, and since this Transform uses the same raw signal values, the values will not be considered valid due to the presence of noise.

The results below from Graphic 4.2 were obtained with a band pass filter from 50 Hz to 150 Hz.

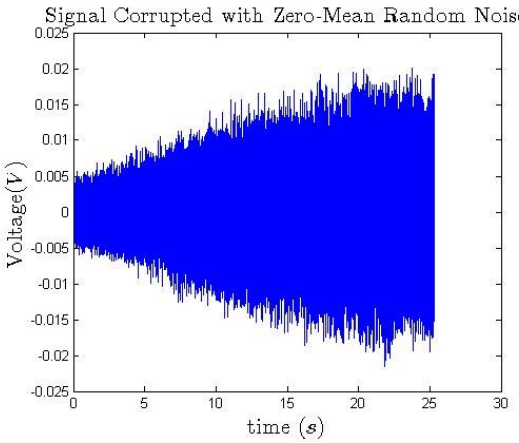

a1)

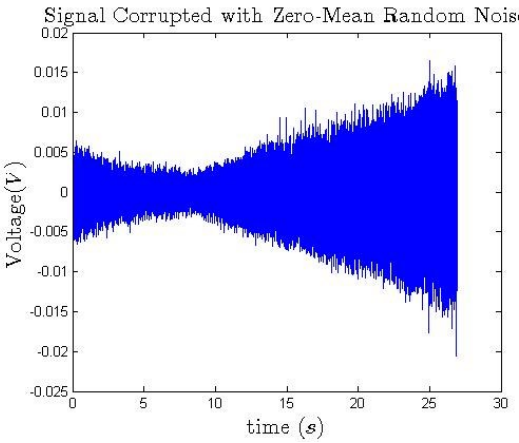

b1)

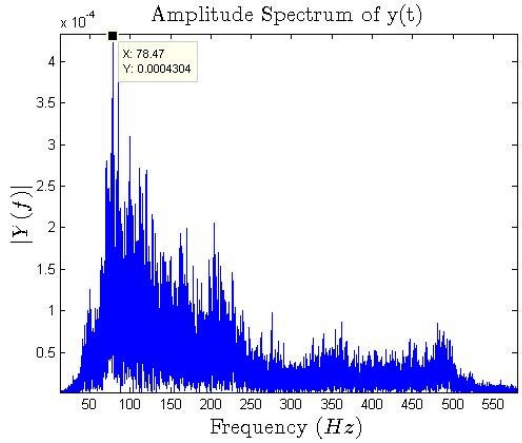

a2)

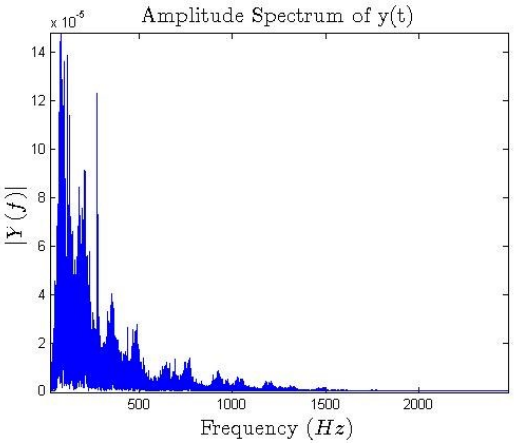

b2)

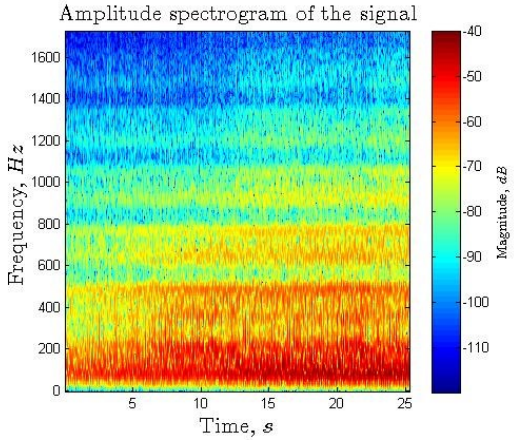

a3)

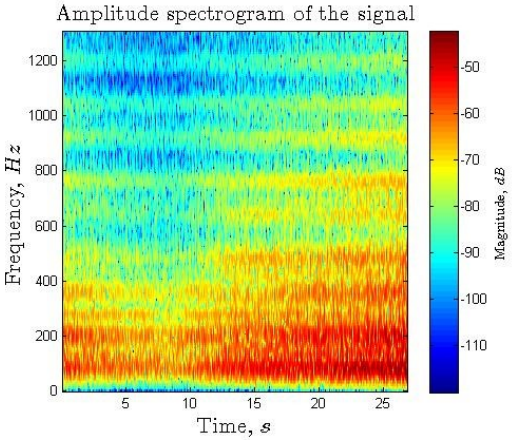

b3)

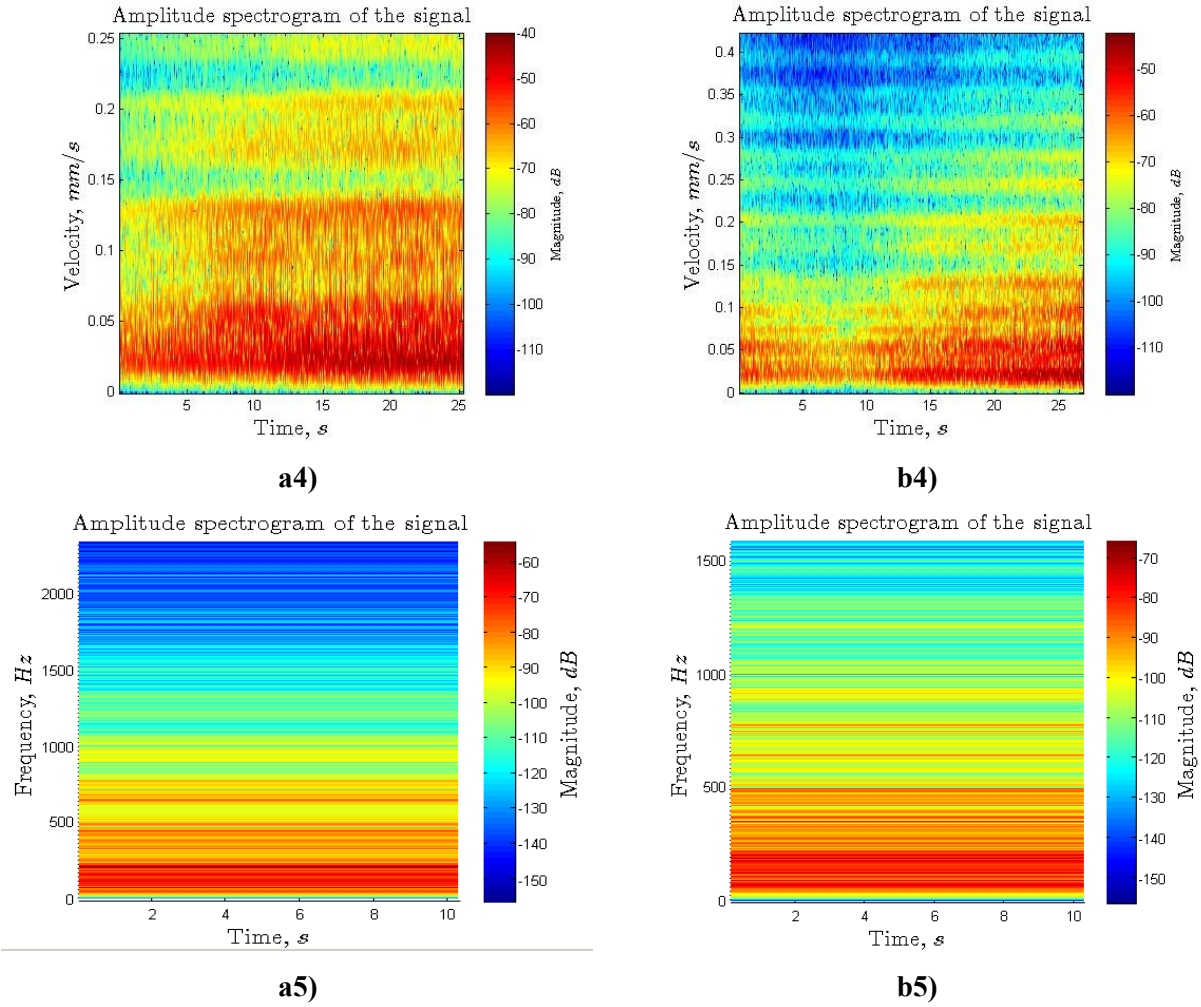

Graphic 4.2 – Signal results from Low speed, (a) forward and (b) backward with filter

Graphic 4.2 a1) and b1) show once again the raw signal from the PD. In these graphics, and comparing with Graphic 4.1 a1) and b1), it is possible to understand that the signal obtained has less frequencies, due to the filter used.

Graphic 4.2 a2) and b2) now show that it is possible to identify the expected frequency results around the 100Hz, both for the forward and backward movements.

Graphic 4.2 a3) and b3) readily show an intense area of red color in the average of 100 Hz. It is almost possible to draw a horizontal straight line in this value along the all-time of the movement, what means that the driver has a constant velocity and the movement has not changed along the time the signal was recorded.

According to the frequencies obtained in Graphic 4.2 a3) and b3) and to the relation between the frequency and velocity from equation (2.66) Graphic 4.2 a4) and b4) was drawn, where the velocity along the time is seen to be mostly constant as expected and in accordance with the theoretical values.

Graphic 4.2 a5) and b5) are obtained from the spectrogram function from Matlab® and concur to prove the results from Graphic 4.2 a3) and b3) are correct.

In conclusion, the results obtained for low speed, for both forward and backward movement, show a residual difference.

4.2.2 LDV results for Normal speed

The analysis at normal speed follow, which, according to Table 3.1, are expected to be, on average, around 0.23 mm/s.

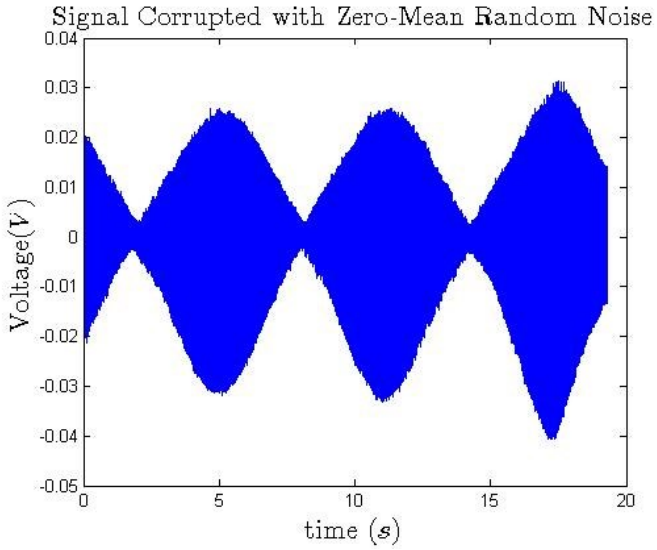

a1)

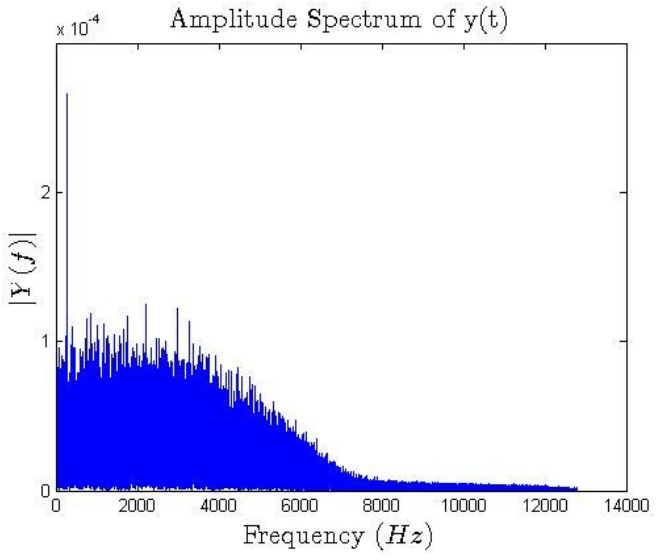

a2)

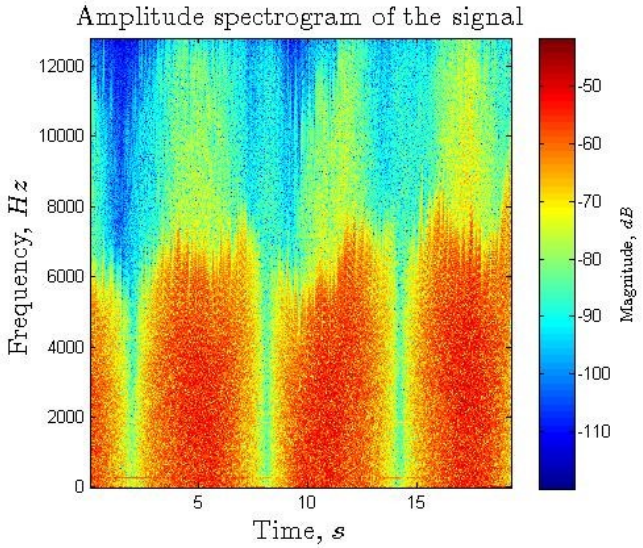

a3)

Graphic 4.3 – Signal results from Normal speed, (a) forward

Graphic 4.3 represents the raw signal of the velocity measurement.

According to Graphic 4.3 a2) it is possible to verify there exists a wide range of frequencies t between 0 and 5 kHz. This result is mostly due to the noise specified before, therefore, in accordance to the theoretical values from Table 3.1, the filter used for this velocity is also a band pass between 800 and 1100 Hz, since the expected frequency is around 970 Hz.

Graphic 4.3 a3) show the frequencies which are in accordance to the range from Graphic 4.3 a2). It also can be seen that the magnitude changes in accordance to the amplitudes verified in the Graphic 4.3 a1).

The results obtained with the chosen band pass filter and shown in Graphic 4.4 will be discussed next.

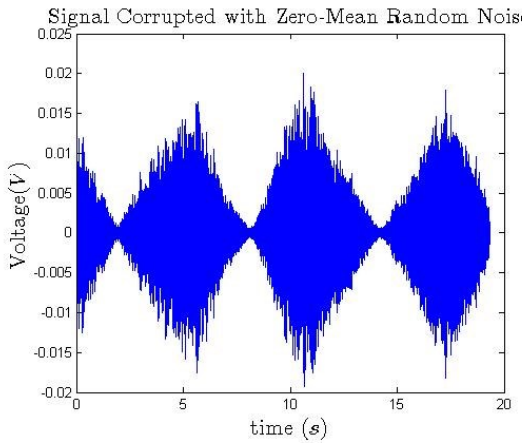

a1)

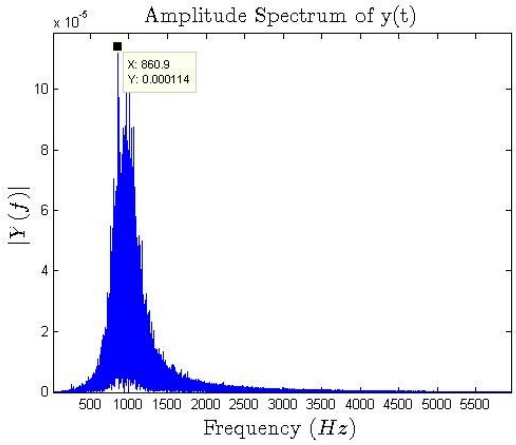

a2)

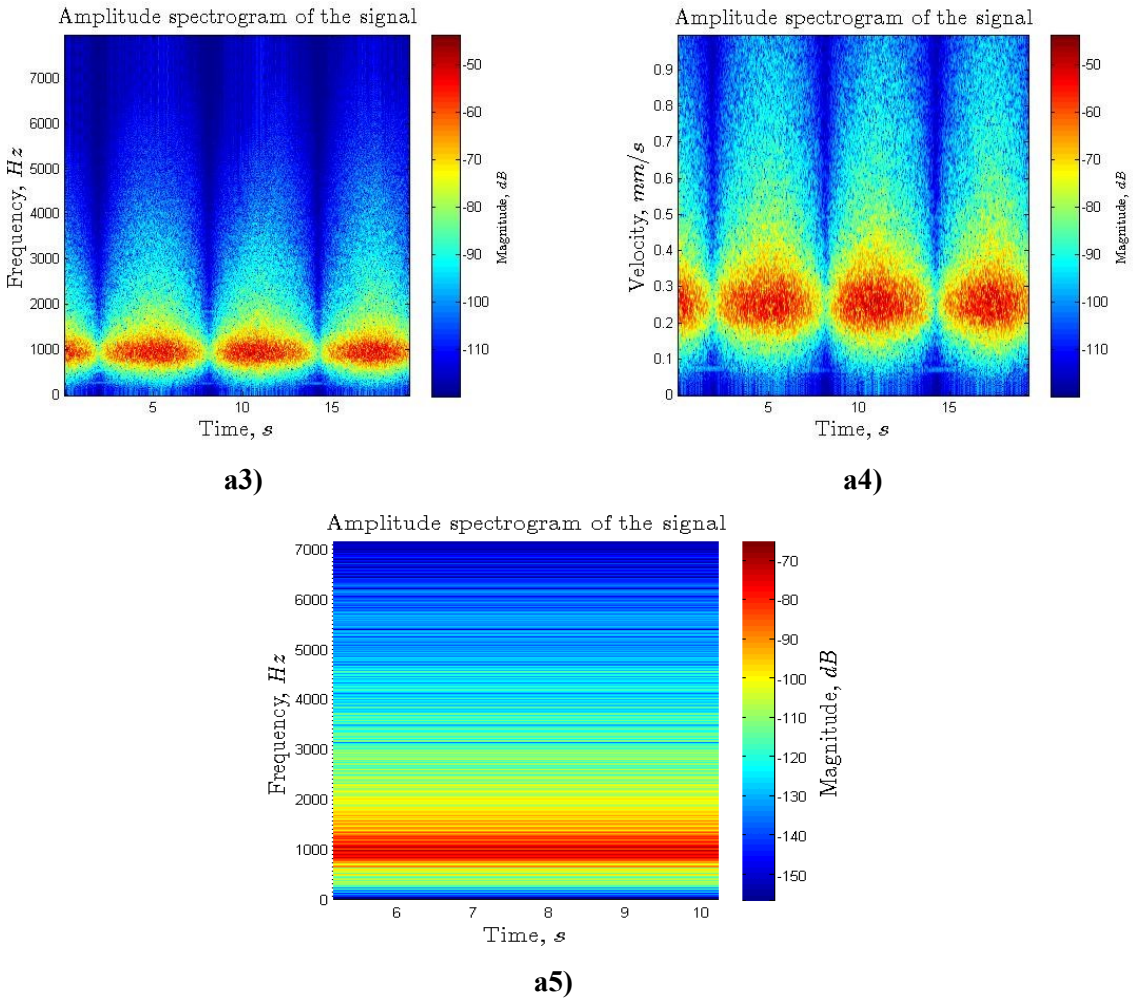

Graphic 4.4 – Signal results from Normal speed, (a) forward with filter

Graphic 4.4 a1) shows the raw signal from the PD. In this graphic, and comparing to Graphic 4.3 a1), it is possible to understand that the signal obtained has less frequency peaks, due to the used filter.

In Graphic 4.4 a2) unlike the previous results, is possible to identify the expected results, with a frequency around the 900 Hz, which is in accordance to the expected result.

An close look at Graphic 4.4 a3) shows that an intense area of red color in the average of 900 Hz is clearly noticeable. These values prove there is a larger signal intensity for the frequencies around this value, as expected. It is almost possible to draw a horizontal straight line in this value along the all-time of the movement, which means that the driver has a constant velocity and the movement hasn't changed appreciably during the time span the signal was recorded. It is easily noticed that in this imaginary horizontal line, there are some areas, in which the intensity decreases significantly.

Now, according to the frequencies obtained in Graphic 4.4 a3) and to the relation between the frequency and velocity from equation (2.66) it is possible to draw Graphic 4.4 a4) where it can be seen the velocity along the time axis, showing the velocity of the movement was nearly constant as expected.

Graphic 4.4 a5) is obtained once more from the spectrogram function from Matlab® and clearly shows the results from Graphic 4.4 a3) are correct.

4.2.3 LDV results for high speed

At high speed, according to Table 3.1, is the velocity is expected to be around 2.4 mm/s.

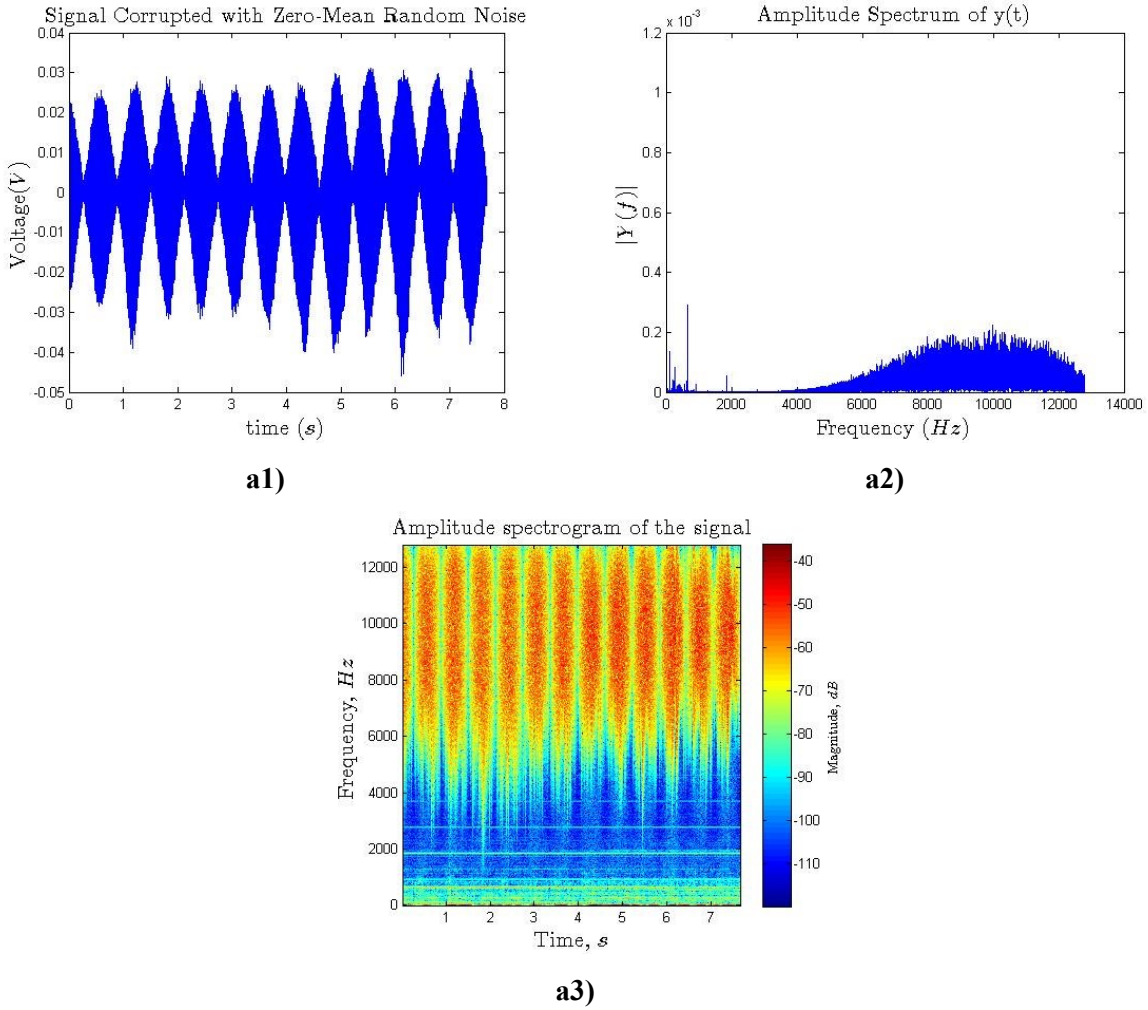

Graphic 4.5 – Signal results from High speed, (a) forward

Graphic 4.5 represents the raw signal of the velocity measurement.

According to Graphic 4.5 a2) it is possible to verify that exists a wide range of frequencies between 7 and 12 kHz. This result is mostly due to the noise alluded before, therefore, in accordance to the theoretical value from Table 3.1, the filter used for this velocity should be a band-pass between 7.5 k and 10 kHz, since the expected frequency is around 8.9 kHz.

In Graphic 4.5 a3) the frequencies are in accordance to the range of frequencies from Graphic 4.5 a2). It can also be seen that the magnitude changes according to the amplitudes verified in Graphic 4.5 a1).

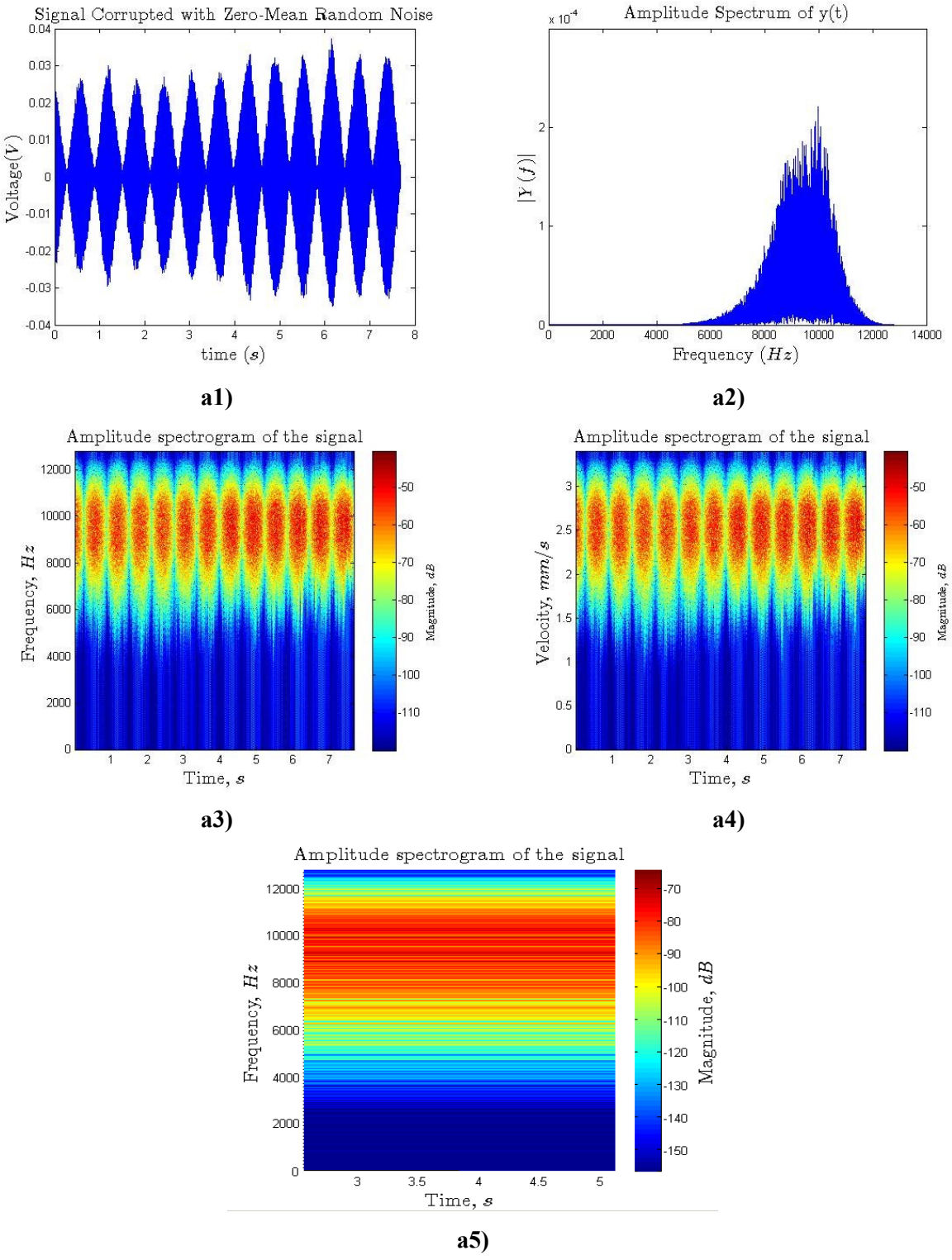

Graphic 4.6 – Signal results from High speed, (a) forward with filter

When using the proposed band-pass filter, the results shown in Graphic 4.6 a1) show the raw signal from the PD and comparing them to Graphic 4.5 a1), is can be seen that the signal obtained has less frequencies, due to the filter used.

In Graphic 4.6 a2) unlike the previous results, it is possible to identify the expected results, with a frequency around the 9.8 kHz, which is proximate to the expected.

Doing an analysis at Graphic 4.6 a3) it is possible to notice the intense area of red color in the average of 9.8 kHz. These values show a greater spectral power density of the frequencies around this value, as expected. It is almost possible to draw a horizontal straight line in this value during the time of the movement, which means that the driver has a constant velocity and the movement has not changed during the time the signal was recorded. It is easily noticed that in the imaginary horizontal line, there are some areas, in which the intensity decreases significantly. If analyzed in detail, these areas occur at the same time where Graphic 4.6 a1) has an amplitude decrease.

Now, according to the frequencies obtained in Graphic 4.6 a3) and using the relation between the frequency and velocity from equation (2.66) Graphic 4.6 a4) is calculated where it can be seen the velocity along the time is mostly constant as expected from the theoretical values.

Graphic 4.6 a5) is obtained from the spectrogram function from Matlab® and shows the results from Graphic 4.6 a3) are as expected.

Table 4.1 present the resume of all obtained values, with a comparison between the calculated frequencies from the measured velocities and the obtained frequencies from the data analysis. In this table are described all three measured velocities and the error between them. The error obtained it is acceptable once the measured velocity is an approximation and also due to the noise of the measurements.

Table 4.1 – Resume of the obtained values

	Measured Velocity [mm/s]	**Calculated Frequency [Hz]**	**Obtained Frequency [Hz]**	**Error %**
Low Speed	0.028	105.28	78	25
Normal Speed	0.26	977.44	860	12
High Speed	2.348	8828	9800	11

4.2.4 Validation of the data

In order to validate the program made in Matlab® and to check if the PD was working as expected frequency of the white fluorescent light in LOME was measured with the PD. This light is supposed to have a frequency around 100 Hz.

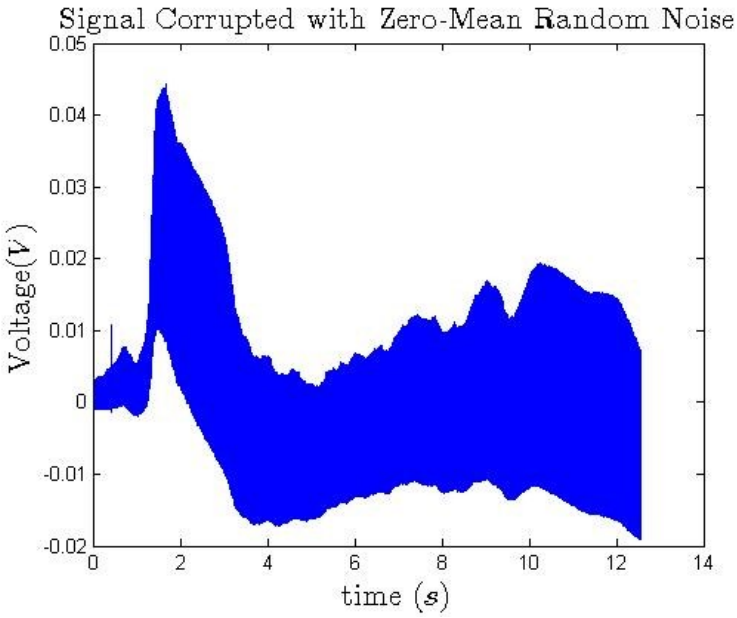
Signal Corrupted with Zero-Mean Random Noise
Voltage(V)
time (s)
0.05
0.04
0.03
0.02
0.01
0
-0.01
-0.02
0
2
4
6
8
10
12
14

a1)

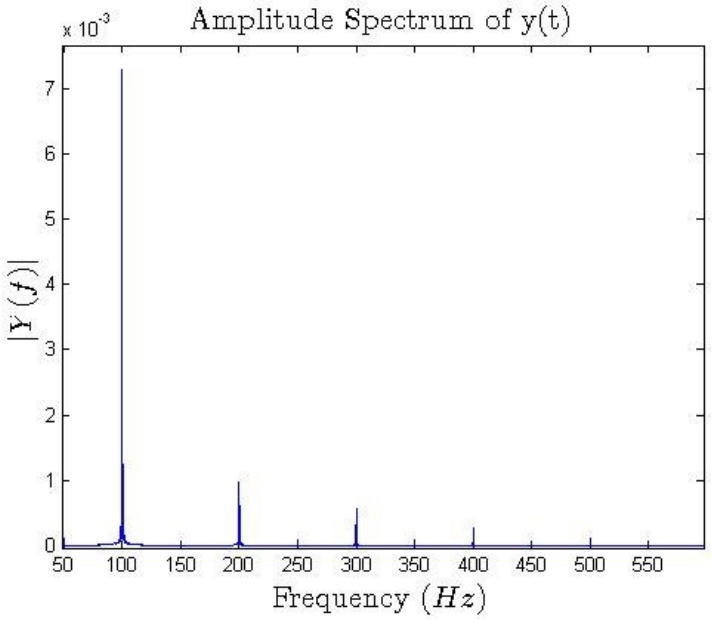
Amplitude Spectrum of y(t)
x 10^-3
|Y(f)|
Frequency (Hz)
7
6
5
4
3
2
1
0
50
100
150
200
250
300
350
400
450
500
550

a2)

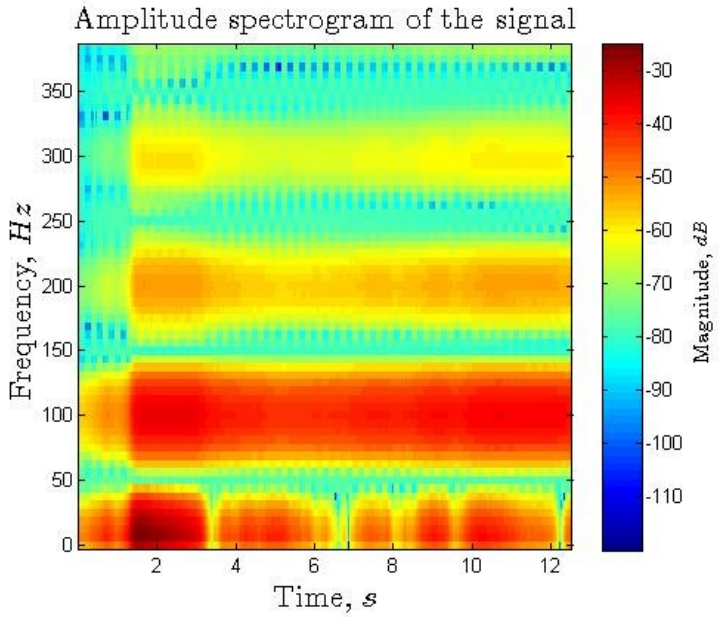

a3)

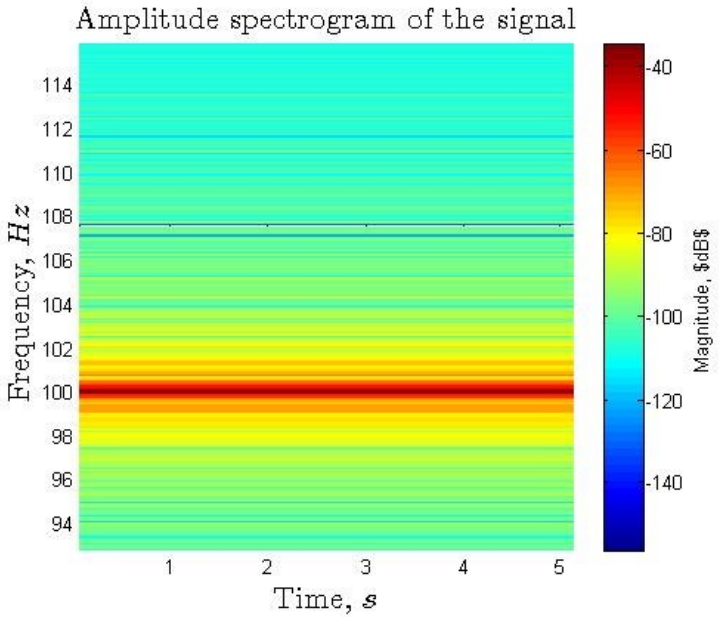

a5)

Graphic 4.7 – Frequency from the white light source

Graphics 4.7 clearly testify the capability of the software tool used in performing data analysis proved not only that the PD is collecting the right signal from the white light at the expected 100Hz, but also that the signal treatment choices were the correct ones, as can be checked on the frequency plots and the STFT spectrogram.

In Graphic 4.7 a2) the harmonics from this frequency happening in cycles of 100, i.e. 200 Hz, 300Hz, etc. are also noticed and the intensity of these harmonics decreases with as expected also.

The amplitude oscillation observed in the signal drawn in Graphic 4.7 a1) is due to the way that the signal was acquired, by turning the PD directly into the laboratory lamp and recording the signal, although this oscillation doesn't really influence the frequency calculations to be performed afterwards.

4.3 Results from PDV

In this section the data acquired with the RIGOL oscilloscope while measuring the velocity of the Hopkinson input bar is analyzed. The output data from the oscilloscope is a CSV file that contains the increments of the respective voltage values.

The parameters of the impact velocity measurements of the bar were established for a pressure of approximately 3 bar. For the acquisition of the signal from PDV, it was necessary to use an external trigger source, which was the signal from the strain gauges at the bar that is used to detect the sound wave that travels in the bar after the impact.

It should be stressed that the longitudinal sound wave travels at a speed of approximately 5 Km/s in the bar, a speed that is characteristic of the bar steel, whereas the bar itself moves at a pace of some 3 to 4 or 5 m/s, which is really the velocity that the PDV probe will measure as the reflector positioned at the bar end moves away from it.

The first measurements were made with an impedance of 1 MΩ, with a sample rate of 2.5 GSa/s and the voltage scale was 1 V per division, as shown in Figure 4.2.

The noisy strain gauge signal in blue shows the incident wave reaching the strain gauge at about 1ms and moving away after some 800 μs, at which time the signal from the PDV probe can be seen to start its readouts, as set by the trigger.

Figure 4.2 – Scope image from the first measurement

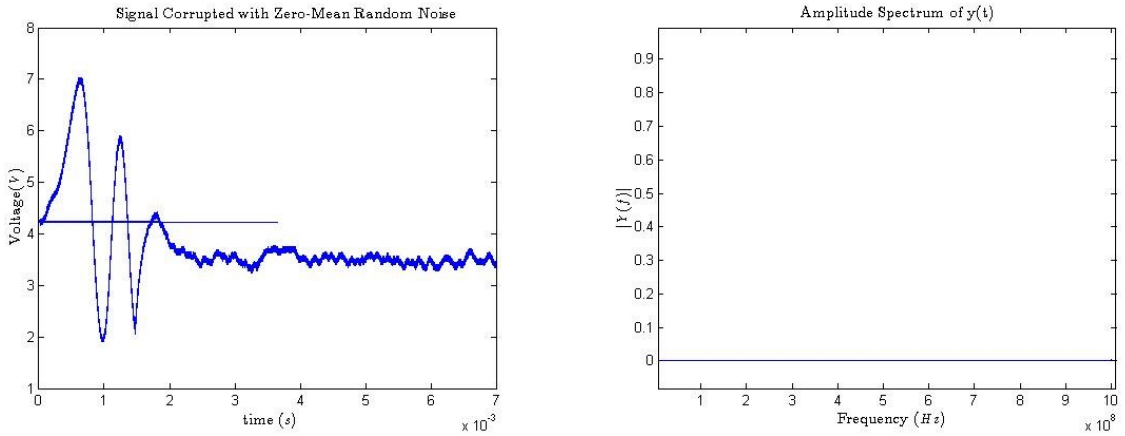

a) **b)**

Graphic 4.8 – Signal results from PDV for 1 MΩ

The signal in Graphic 4.8 a) is the output signal detected from the probe in yellow in yellow, where is possible to say that the movement of the bar starts at nearly 2 ms and the frequency obtained after this time is referred to the velocity of the bar.

To identify the velocity it is necessary to calculate the FFT of the signal and identify the main frequency. According to Graphic 4.8 b) the FFT of the signal does not show any frequency, which means that the oscilloscope could not detect any velocity during the measurement. The reason for this is related with the overload of the oscilloscope in voltage values. Accordingly, the movement detected in Graphic 4.8 a) is not the velocity of the bar but only noise detected by the probe.

Since no results were obtained with oscilloscope in 1 MΩ, now data acquisition was performed with an impedance of 50 Ω. The sample rate used was 50 MSa/s and the voltage scale was 2 mV per division.

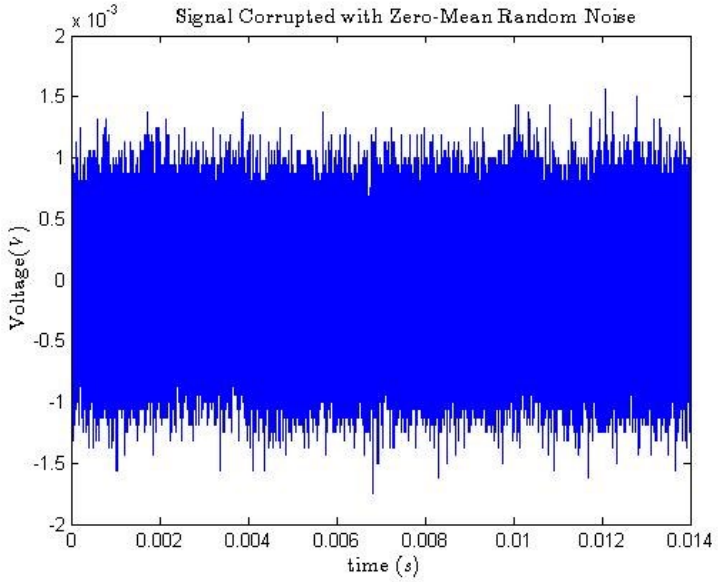

Graphic 4.9 – Signal results from PDV for 50 Ω

The Graphic 4.9 it is referred to the output signal detected from the probe.

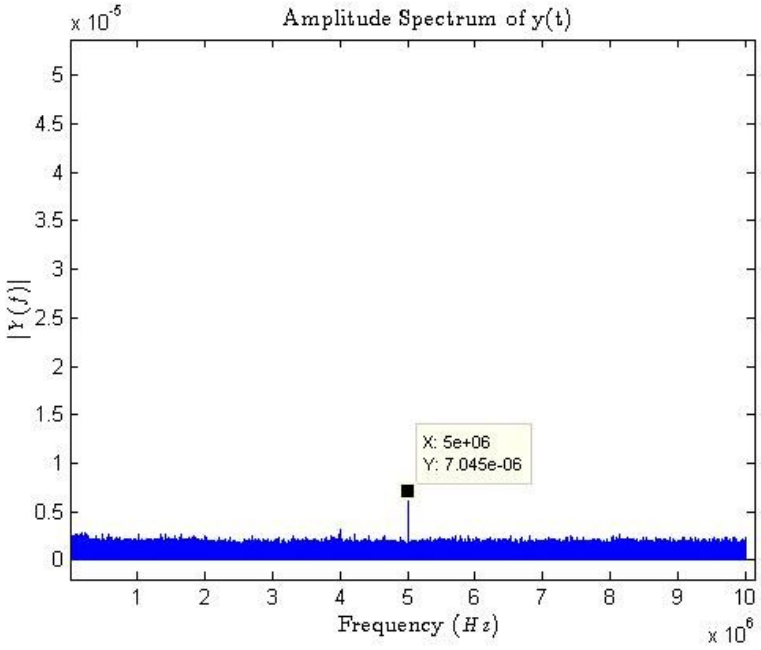

Graphic 4.10 – FFT of the signal from PDV

Graphic 4.10 represents the FFT of the signal obtained in Graphic 4.9. It is possible to identify the main frequency of the movement and this frequency corresponds to 5 MHz. According to Eq. (2.66), this frequency corresponds to a velocity of approximately 3.8 ms^{-1}which is found to agree with the expected velocity of the bar.

PDV data analysis spectrogram could not be performed due to the fact that the power of the laser was too low and the oscilloscope could not detect an effective frequency signal in time domain. The Erbium Doped Fiber Amplifier which was ordered will increase the 5mW of the fiber laser to some 2.75dB or 500mW output power, clearly improving the laser performance and enabling noise reducing strategies much more efficient.

5 FUTURE WORK

Since this thesis appear through a work in progress from a FCT project, the project still has several pending working subjects to go on. In this chapter it is described the future work that is still to be done until the end of this project.

Also, as this thesis was taken up in LOME, it arose the need to develop a prototype of the LDV to measure several velocities, from different applications and also the final PDV. Therefore, in this chapter, it is also presented a proposal for a portable LDV and a PDV, that will be deployed as soon as the LOME direction sees fit.

5.1 Future Work

The next step to do in this project is, as soon as the EDFA fiber amplifier arrives, is to insert it in the PDV assembly and try to obtain some results about the range of velocities that the Hopkinson bar is capable of.

The amplifier selected for the PDV was already referred in section 3.3 and is an EDFA Module from NUPHOTONICS Technologies with the following specifications.

Features:

- 1540 – 1565 nm wavelength range;
- +27 dBm output power provided for input power as low as +7 dBm;
- +5 VDC powered EDFA Module;

The full specifications of the EDFA Module with all the mechanical drawings can be found in Annex J.

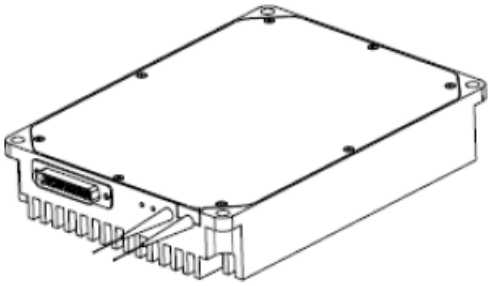

Figure 5.1 – EDFA Module Mechanical Drawing

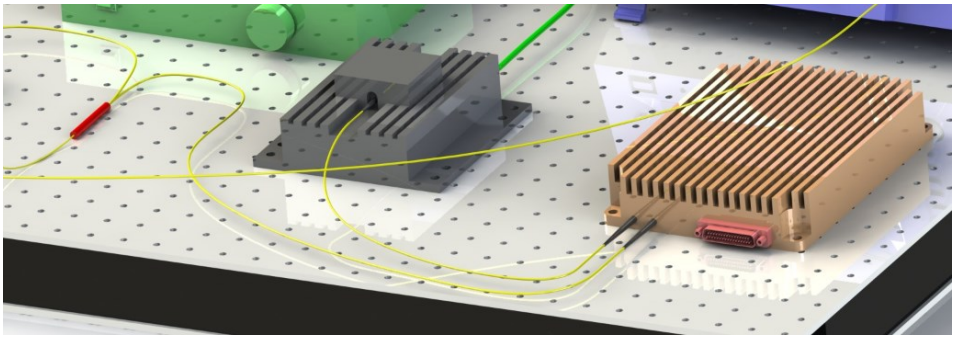

Figure 5.2 – Detail of the amplifier inserted in the PDV

This amplifier will be connected between the laser diode and the port 1 of the circulator, as shown in Figure 3.16 and in detail in Figure 5.2. With the amplifier setup, to have a PDV probe working distance of nearly 20 mm is expected that should be enough to perform low-noise measurements of the velocity at the Hopkinson bar.

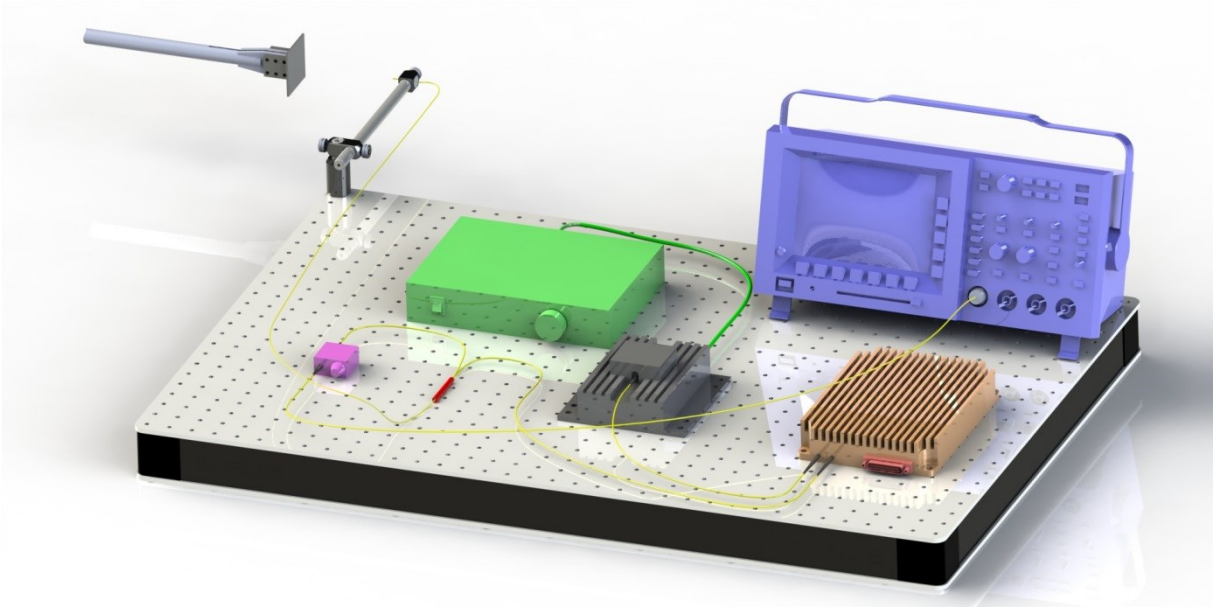

Figure 5.3 – Final Scheme of the PDV adapted in Hopkinson bar

After all the tests and acquisition of the data at the Hopkinson bar, the PDV will be adapted for the electromagnetic forming, to measure the velocities that materials can achieve during the expanding ring tests.

A second probe will be used to monitor deformation velocities in two directions.

In summary, a difficult ambitious project for the future awaits the conclusion of the first setup now accomplished. Some critical situations will need to be carefully planned and scrutinized that have a very short range for error accommodation. The aim of this future work is to create a clear link between the high speed analysis and the material deformations, and also figure out how the direction of measurement changes the frequencies, and how this relation is connected to the real speed of deformation. The proposed objectives have a lot of concerns that cannot be answered now, and there is still some uncertainty about the relation between the speed/frequencies measured in PDV and the material deformation. For all explained, this will certainly be a very interesting project to be done in a near future.

5.2 LDV Prototype

With the implementation of an LDV during the development of the current work, arouse the idea of developing a portable LDV. The need of a LDV instrument in LOME emerged due to the fact that there is no such equipment in the Laboratory, although the need to measure velocities is frequent.

The requirements for this LDV was to be portable and small and to be applied in different applications, therefore it was designed to be very compact as per the scheme presented in Figure 5.4

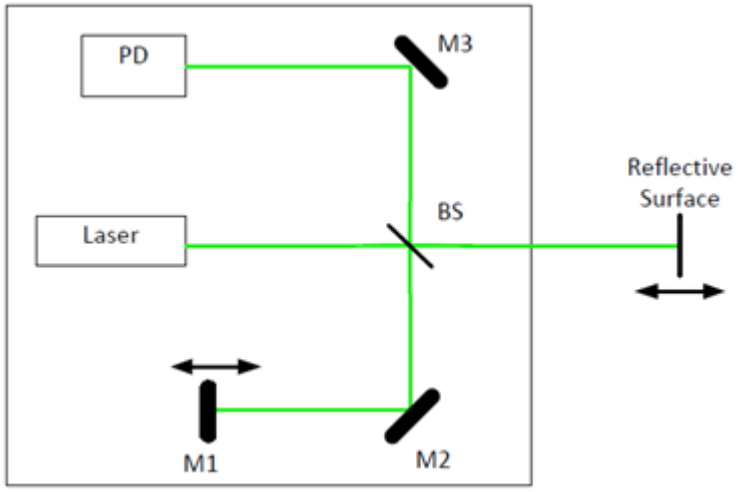

Figure 5.4 – Scheme of the portable LDV

The major difference between this portable LDV and the one developed in section 3.2 is the position of the PD and M1. In order to make it more compact, the PD can be placed near the laser and the M3 can send the laser beam to the PD with the shifted frequency. M1 can be also placed on the other side of the laser, once the path of the arms of the interferometer needs to be same, in the fixed arm is placed a mirror M2. The arms of the interferometer need to be approximately the same length, to maintain the coherence of the laser beam once the moving arm will increase or decrease the length of the respective arm according to the reflective surface. As one of the requirements was the LDV to be used in the most various applications, M1 can be adjusted so the length of the fixed arm is the same of the moving one.

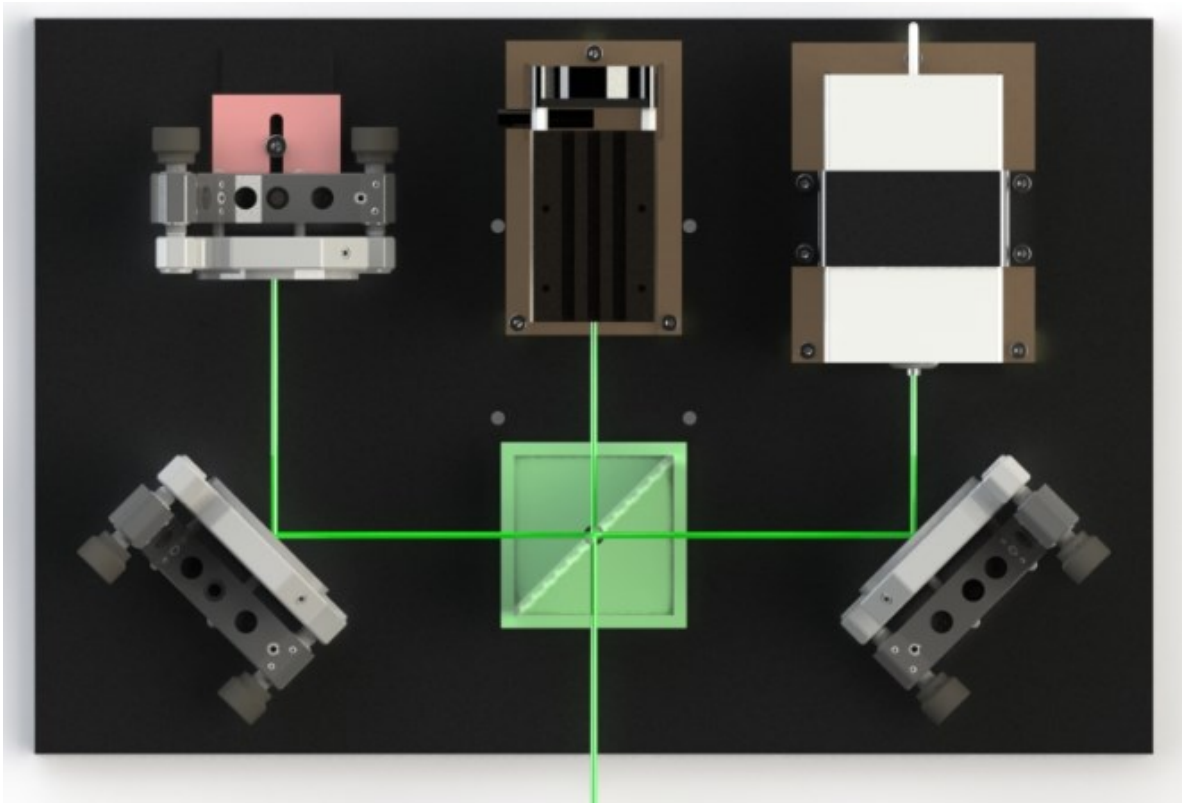

Figure 5.5 – Scheme of the portable LDV

The components of this LDV are the ones existing in LOME, the laser and the PD are the same used in the LDV developed for this thesis and are placed in a small breadboard. Since the Michelson interferometer is a very sensitive interferometer, the LDV needs to be placed inside a portable box.

This box, shown in Figure 5.6 has an aperture in the direction of the moving arm of the LDV. This gap is used to protect the LDV inside the box and it is only open when there is the need to measure velocities.

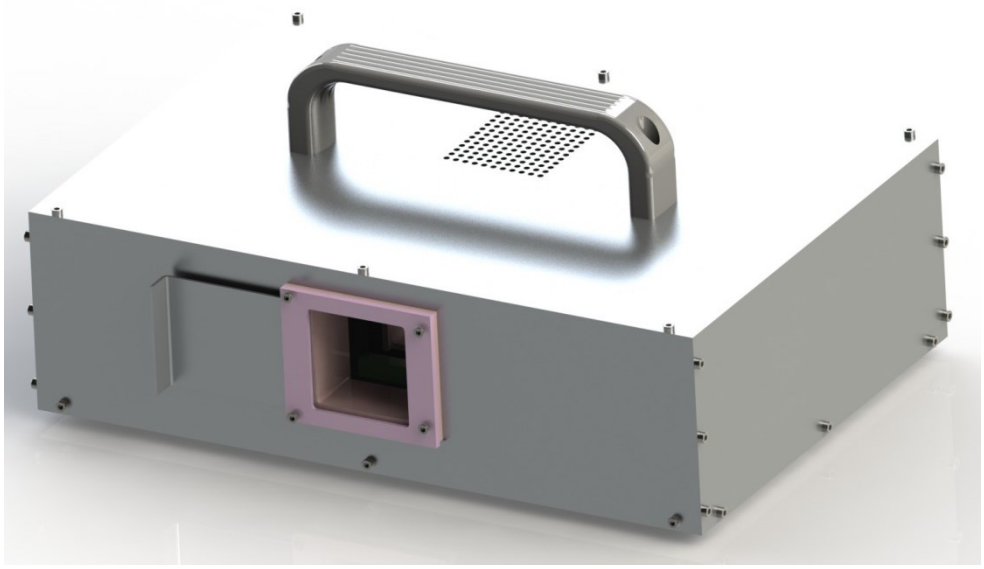

Figure 5.6 – External appearance of the LDV

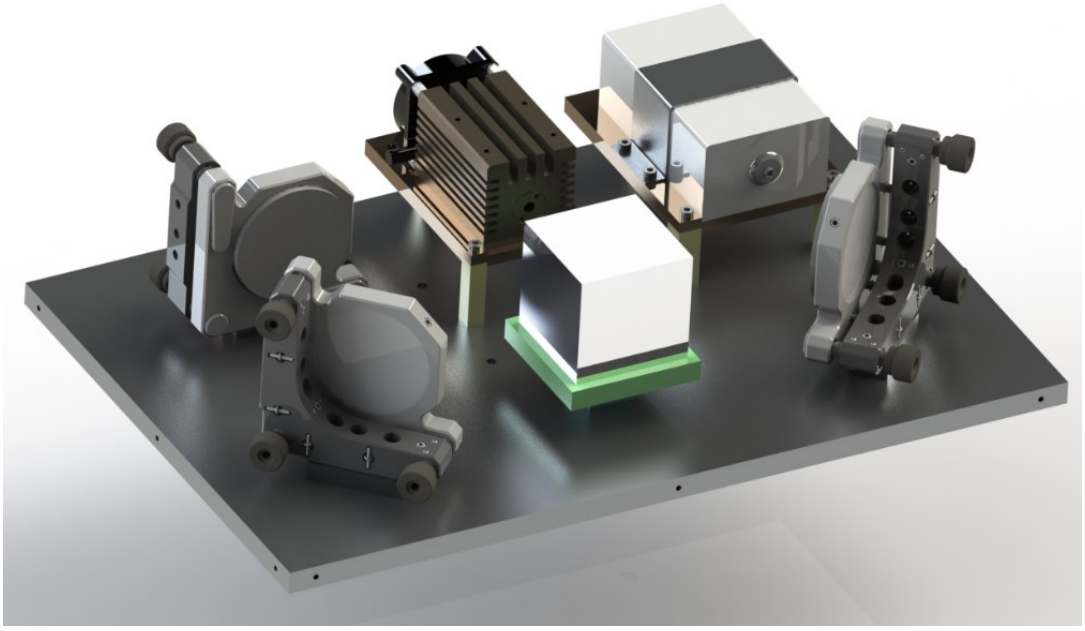

Figure 5.7 – Aspect of the LDV inside the box

6 CONCLUSIONS

This dissertation work presents the development of a LDV for plastic deformation monitoring. Under that assumption, the initial objectives were fulfilled, whereupon the implementation of a LDV was completed and enabled the measurement of velocities. A PDV was also developed for higher-order velocity measurements near to completion and already used for successfully measuring small speeds in the SHPB, which is only limited by the lack of the laser amplifier for adequately reducing the noise in the measurements. Finally a proposal for a portable LDV equipment was advanced and a prototype was developed that LOME will be able to build in the future.

The initial work on a LDV assembly with a Mach- Zehnder interferometer and two Acousto-Optic Modulators (AOM) served the instructive purpose of introducing the realm of the Doppler Effect and its applications, thereby being adequate as an exploratory challenge where the moving object would be replaced by the modulator and its artificially imposed Doppler shift. Inasmuch as the plethora of laboratorial instrumentation and the AOM itself had to be used and therefore known to an adequate extent, this initial work was in fact an opportunity for grasping the technicalities involved in such assemblies. The fact the equipment was out of order and the AOMs didn't modulate the input light as expected, prevented the achievement of conclusive results, although the importance of this initial setup really was to introduce the subject.

The following setup with a Michelson interferometer further extended the experience with laser interferometers and the Doppler Effect. Michelson interferometers are very sensible devices and even slight air movements could at times influence fringe stability. Further to that, setups with un-expanded laser beams are difficult to control and align, even if the obtained fringes were relatively stable and measurements could already be performed that were in full agreement with the theory, as expected. Some measurement noise, most likely due to uncoupled electronic noise at the Photodetector perturbed some of the measurements but still the discrepancy with the measured velocities was within acceptable ranges, between 2 and 10%.

A Matlab program for evaluating the LDV and PDV results that read the data files, performed a preliminary spectral analysis and thirdly performed a Power Spectral Density spectrogram analysis was fully developed within the context of this work. A check of the obtained analysis results from the

known values of ordinary fluorescent light in the laboratory was performed with excellent results. This software was really a necessity for analysing the signals from the photodetector and the PDV probe, as there is no other expedite way to perform that analysis.

The setup of the all-fibre PDV device was straightforward and the device performs very well even with a 5mW laser, showing a very good stability. The exploration of the device's capabilities at high and very high velocities with the fiber amplifier at nearly 500 mW laser output is greatly anticipated, as is the possibility of measuring velocity along independent directions and checking the results.

The portable instrument design and development involved the laboratory people in order to make it as compact as possible without losing the necessary flexibility to adapt to the requirements of complex situations wherefore velocity measurements are necessary, albeit technically demanding. One of the laboratory's greatly appraised capabilities is the development of its own equipment whenever it can't be found in the commerce. Several pieces of equipment have been devised and built over the years that fit into this reasoning, as does the proposed LDV.

In conclusion, the present work has been a rewarding one from different perspectives, because of both their quality and the importance of their impact, clearly testifying to the high degree of dedication and motivation along the entire work.

7 REFERENCES

1. Marciniak, Z., J.L. Duncan, and S.J. Hu, *Mechanics of Sheet Metal Forming*. 2002.
2. Nurcheshmeh, M., *NUMERICAL PREDICTION OF SHEET METAL FORMING LIMITS*, in *Electronic Theses and Dissertations*2011, University of Windsor.
3. Stoughton, T.B. and X. Zhu, *Review of theoretical models of the strain-based FLD and their relevance to the stress-based FLD.* International Journal of Plasticity, 2004. **20**(8–9): p. 1463-1486.
4. Oliveira, I., et al., *Study of strain-rate-dependent behavior of an aluminum alloy during high speed loading*, 2013: Germany.
5. Johnson, J.R., et al., *Coupling Experiment and Simulation in Electromagnetic Forming Using Photon Doppler Velocimetry.* steel research international, 2009. **80**(5): p. 359-365.
6. Sargis, P.D., et al., *Photonic Doppler Velocimetry*, 1999, Lawrence Livermore National Laboratory.
7. Oliveira, I.V.d., *Electromagnetic forming process numerical modelling and analysis of process parameters*. 2013, Porto: FEUP. XVIII, 121 p.-XVIII, 121 p.
8. Rocha, A.B.d. and J.F. Duarte, *Tecnologia da Embutidura*. 1992.
9. Albrecht, H.E., et al., *Laser Doppler and Phase Doppler Measurement Techniques*. 2003.
10. Pain, H.J., *The Physics of Vibrations and Waves*. 6th ed. 2005.
11. McMillan, C.F., et al., *Velocimetry of fast surfaces using Fabry–Perot interferometry.* Review of Scientific Instruments, 1988. **59**(1): p. 1-21.
12. Reed, E.J., M. Soljačić, and J.D. Joannopoulos, *Reversed Doppler Effect in Photonic Crystals.* Physical Review Letters, 2003. **91**(13): p. 133901.
13. Moore, J.H., et al., *Building Scientific Apparatus - A Practical Guide to Design and Construction*. Fourth Edition ed. 2009.
14. Hecht, E., *Optics*. Fourth Edition ed. 2002.
15. Hariharam, P., *Basics of Interferometry*. Second Edition ed. 2007.
16. Guenther, R.D., *Modern Optics*. 1990.
17. Sharma, K.K., *Optics, Principles and applications*. 2006.
18. Gasvik, K.J., *Optical Metrology*. Third Edition ed. 2002.
19. Sweatt, W.C., P.L. Stanton, and J.O.B. Crump. *Simplified VISAR system*. 1991.
20. Barker, L.M. and R.E. Hollenbach, *Laser interferometer for measuring high velocities of any reflecting surface.* Journal of Applied Physics, 1972. **43**(11): p. 4669-4675.
21. Dolan, D.H., *Foundations of VISAR analysis*, 2006, Sandia National Laboratories.
22. Buttler, W.T., et al., *Optical Velocimetry*. 2004.
23. Krauter, K. and S.O. Agbo, *Single-mode VISAR: A Thesis*. 2007: California Polytechnic State University.
24. Strand, O.T., et al., *Compact system for high-speed velocimetry using heterodyne techniques.* Review of Scientific Instruments, 2006. **77**(8): p. 083108-083108-8.

25. Weng, J., et al., *Optical-fiber interferometer for velocity measurements with picosecond resolution.* Applied Physics Letters, 2006. **89**(11): p. -.
26. Hemsing, W.F., *Velocity sensing interferometer (VISAR) modification.* Review of Scientific Instruments, 1979. **50**(1): p. 73-78.
27. Fleming, K.J. and T.A. Broyles, *Shock Analysis Using the Multi Point Velocimeter (VISAR)*, 2003, Sandia National Laboratories. p. 28.
28. Arrigoni, M., et al., *Laser Doppler interferometer based on a solid Fabry–Perot etalon for measurement of surface velocity in shock experiments.* Measurement Science and Technology, 2009. **20**(1): p. 015302.
29. Tavares, P.J.d.S., *Three-dimensional geometry characterization using structured light fields*. 2008, Porto: [s. n.]. XXX, 271, [2] p.-XXX, 271, [2] p.
30. Strand, O.T., et al. *Velocimetry using heterodyne techniques*. 2005.
31. Holtkamp, D.B. *Survey of Optical Velocimetry Experiments - Applications of PDV, A Heterodyne Velocimeter*. in *Megagauss magnetic field generation and related topics, 2006 ieee international conference on*. 2006.
32. Kuznetsov, V.A. and S.P. Bennetts, *Development of Photon Doppler Velocimeter for Explosives Research*, 2013, Australian Government Department of Defence - Defence Science and Technology Organisation.
33. Press, W.H., *Numerical recipes 3rd edition: The art of scientific computing*. 2007: Cambridge university press.
34. Casem, D.T. and M.B. Zellner, *Kolsky Bar Wave Separation Using a Photon Doppler Velocimeter.* Experimental Mechanics, 2013. **53**(8): p. 1467-1473.
35. Ferreira, F.J., *Análise do comportamento dinâmico de componentes estruturais sob solicitações generalizadas*. 2003, Porto: [s. n.]. IIII, 231, [24] p.-IIII, 231, [24] p.
36. Avinadav, C., Y. Ashuach, and R. Kreif, *Interferometry-based Kolsky bar apparatus.* Review of Scientific Instruments, 2011. **82**(7): p. -.
37. Hotz, W., et al., *Time Dependent FLC Determination Comparison of Different Algorithms to Detect the Onset of Unstable Necking before Fracture.* Key Engineering Materials, 2013. **Volume 549**(Sheet Metal 2013): p. 397-404.

8 ANNEXES

8.1 Annex A – Photo detector Data Sheet

MRD500 (SILICON)
MRD510

PIN SILICON PHOTO DIODE

. . . designed for application in *laser detection, light demodulation,* detection of visible and near infrared light-emitting diodes, shaft or position encoders, switching and logic circuits, or any design requiring radiation sensitivity, ultra high-speed, and stable characteristics.

- Ultra Fast Response – (<1.0 ns Typ)
- High Sensitivity – MRD500 (1.2 μA/mW/cm^2 Min) MRD510 (0.3 μA/mW/cm^2 Min)
- Available With Convex Lens (MRD500) or Flat Glass (MRD510) for Design Flexibility
- Popular TO-18 Type Package for Easy Handling and Mounting
- Sensitive Throughout Visible and Near Infrared Spectral Range for Wide Application
- Annular Passivated Structure for Stability and Reliability

100 VOLT
PHOTO DIODE
PIN SILICON

100 MILLIWATTS

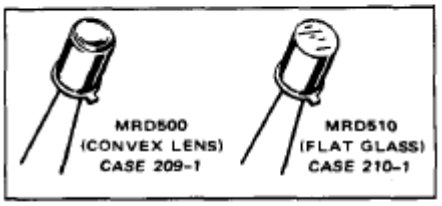

MAXIMUM RATINGS (T_A = 25°C unless otherwise noted)

Rating	Symbol	Value	Unit
Reverse Voltage	V_R	100	Volts
Total Device Dissipation @ T_A = 25°C Derate above 25°C	P_D	100 0.57	mW mW/°C
Operating and Storage Junction Temperature Range	T_J T_{stg}	-65 to +200	°C

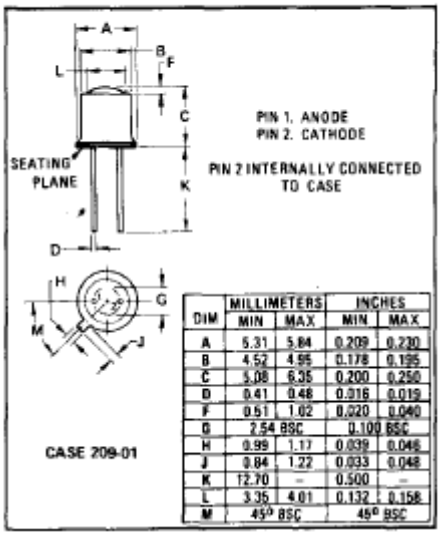

DIM	MILLIMETERS MIN	MILLIMETERS MAX	INCHES MIN	INCHES MAX
A	5.31	5.84	0.209	0.230
B	4.52	4.95	0.178	0.195
C	5.08	6.35	0.200	0.250
D	0.41	0.48	0.016	0.019
F	0.51	1.02	0.020	0.040
G	2.54 BSC		0.100 BSC	
H	0.99	1.17	0.039	0.046
J	0.84	1.22	0.033	0.048
K	12.70	–	0.500	–
L	3.35	4.01	0.132	0.158
M	45° BSC		45° BSC	

FIGURE 1 – TYPICAL OPERATING CIRCUIT

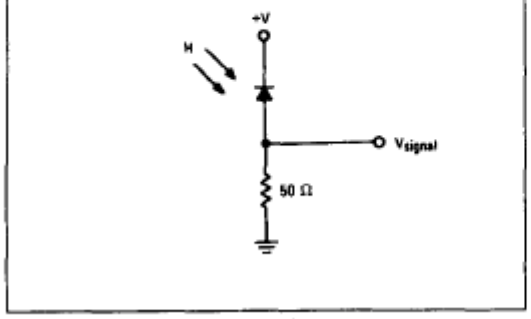

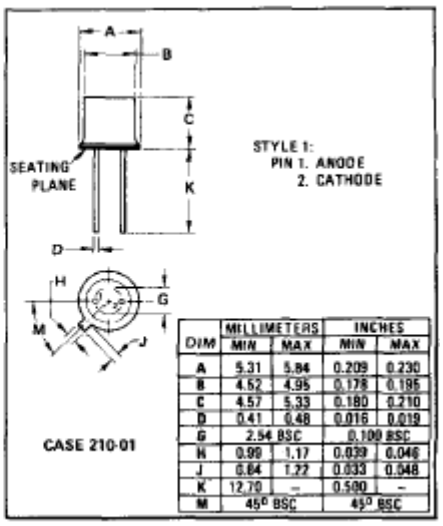

DIM	MILLIMETERS MIN	MILLIMETERS MAX	INCHES MIN	INCHES MAX
A	5.31	5.84	0.209	0.230
B	4.52	4.95	0.178	0.195
C	4.57	5.33	0.180	0.210
D	0.41	0.48	0.016	0.019
G	2.54 BSC		0.100 BSC	
H	0.99	1.17	0.039	0.046
J	0.84	1.22	0.033	0.048
K	12.70	–	0.500	–
M	45° BSC		45° BSC	

STATIC ELECTRICAL CHARACTERISTICS (T_A = 25°C unless otherwise noted)

Characteristic	Fig. No.	Symbol	Min	Typ	Max	Unit
Dark Current (V_R = 20 V, R_L = 1.0 megohm; Note 2)		I_D				nA
T_A = 25°C	4 and 5		–	–	2.0	
T_A = 100°C			–	14	–	
Reverse Breakdown Voltage (I_R = 10 μA)	–	BV_R	100	200	–	Volts
Forward Voltage (I_F = 50 mA)	–	V_F	–	–	1.1	Volts
Series Resistance (I_F = 50 mA)	–	R_s	–	–	10	ohms
Total Capacitance (V_R = 20 V; f = 1.0 MHz)	6	C_T	–	–	4	pF

OPTICAL CHARACTERISTICS (T_A = 25°C)

Characteristic		Fig. No.	Symbol	Min	Typ	Max	Unit
Radiation Sensitivity (V_R = 20 V, Note 1)			S_R				μA/mW/cm²
	MRD500	2 and 3		1.2	1.8	–	
	MRD510			0.3	0.42	–	
Sensitivity at 0.8 μm (V_R = 20 V, Note 3)			$S_{(\lambda = 0.8\ \mu m)}$				μA/mW/cm²
	MRD500	–		–	6.6	–	
	MRD510	–			1.5	–	
Response Time (V_R = 20 V, R_L = 50 ohms)		–	$t_{(resp)}$		1.0		ns
		–					
Wavelength of Peak Spectral Response		7	λ_s	–	0.8	–	μm

NOTES:

1. Radiation Flux Density (H) equal to 5.0 mW/cm² emitted from a tungsten source at a color temperature of 2870 K.
2. Measured under dark conditions. (H≈0).
3. Radiation Flux Density (H) equal to 0.5 mW/cm² at 0.8 μm.

TYPICAL ELECTRICAL CHARACTERISTICS

FIGURE 2 – IRRADIATED VOLTAGE – CURRENT CHARACTERISTIC FOR MRD500

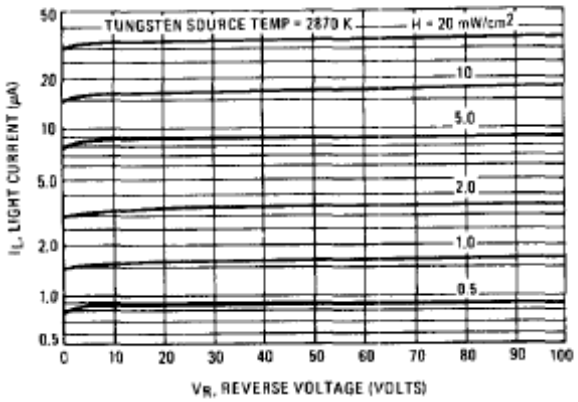

FIGURE 3 – IRRADIATED VOLTAGE – CURRENT CHARACTERISTIC FOR MRD 510

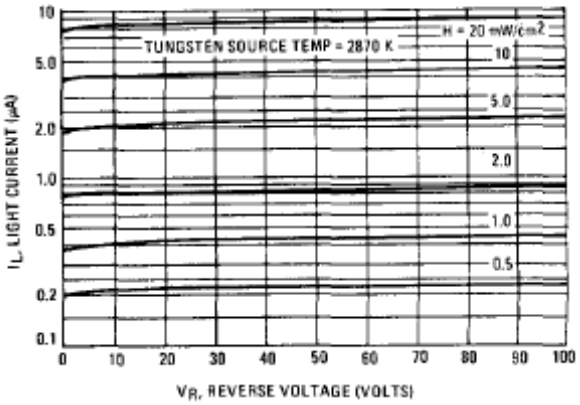

FIGURE 4 – DARK CURRENT versus TEMPERATURE

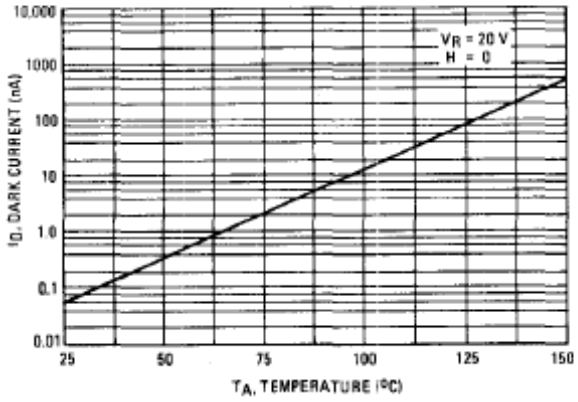

FIGURE 5 – DARK CURRENT versus REVERSE VOLTAGE

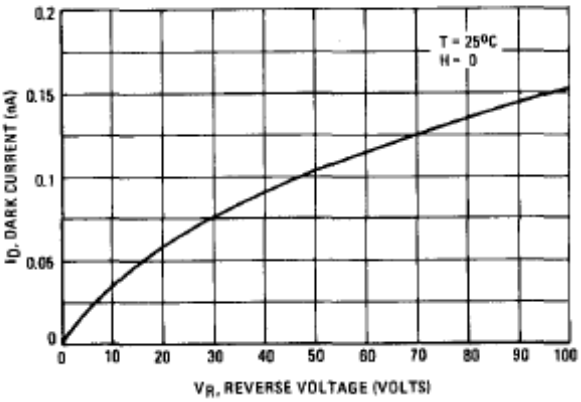

FIGURE 6 – CAPACITANCE versus VOLTAGE

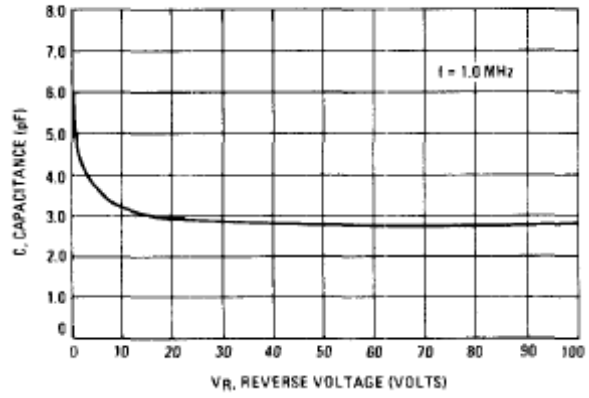

FIGURE 7 – RELATIVE SPECTRAL RESPONSE

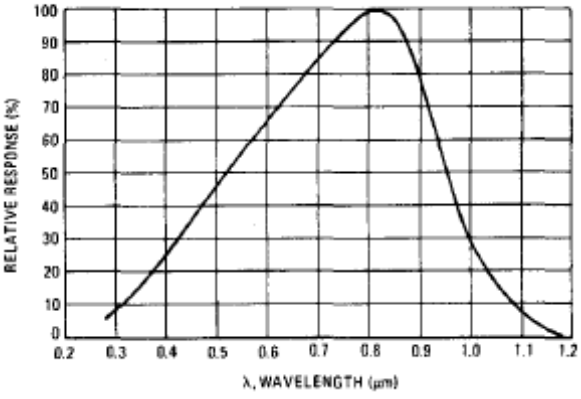

MRD500 AND MRD510
OPTOELECTRONIC DEFINITIONS, CHARACTERISTICS, AND RATINGS

BV_R Reverse Breakdown Voltage – The minimum dc reverse breakdown voltage at stated diode current and ambient temperature.

C_T Total Capacitance

H Radiation Flux Density (Irradiance) [mW/cm^2] – The total incident radiation energy measured in power per unit area.

I_D Dark Current – The maximum reverse leakage current through the device measured under dark conditions, ($H \approx 0$), with a stated reverse voltage, load resistance, and ambient temperature.

P_D Power Dissipation

R_s Series Resistance – The maximum dynamic series resistance measured at stated forward current and ambient temperature.

S_R Radiation Sensitivity ($\mu A/mW/cm^2$) – The ratio of photo-induced current to the incident radiant energy measured at the plane of the lens of the photo device under stated conditions of radiation flux density (H), reverse voltage, load resistance, and ambient temperature.

T_A Ambient Temperature

T_J Junction Temperature

T_{stg} Storage Temperature

V_F Forward Voltage – The maximum forward voltage drop across the diode at stated diode current and ambient temperature.

V_R Reverse Voltage – The maximum allowable value of dc reverse voltage which can be applied to the device at the rated temperature.

$\lambda_s(\mu m)$ Wavelength of peak spectral response in micro meters.

OPTO DEVICES

AN-440 – THEORY AND CHARACTERISTICS OF PHOTO TRANSISTORS

A brief history of the photoelectric effect is discussed, followed by a comprehensive analysis of the effect in bulk semiconductors, pn junctions and phototransistors. A model is presented for the phototransistor. Static and transient data for the MRD300 provide typical phototransistor characteristics. Appendices provide a discussion of the relationship of irradiation and illumination and define terms specifically related to phototransistors.

AN-508 Applications of Phototransistors in Electro-Optic Systems

This note reviews phototransistor theory, characteristics and terminology, then discusses the design of electro-optic systems using device information and geometric considerations. It also includes several circuit designs that are suited to dc, low-frequency and high-frequency applications.

8.2 Annex B – Determination of the velocities of the micro-positioner

Table 8.1 – Measurements of the velocity from the micro-positioner

Direction	Distance [mm]	Time [s]	Velocity [mm/s]		Distance [mm]	Time [s]	Velocity [mm/s]
Forward	10.0164	354.55	0.02825		10.0164	354.3	0.02827
	9.991	357	0.02799		9.991	356.6	0.02802
	9.9994	358.77	0.02787		9.9994	358.8	0.02787
	10.0053	357.85	0.02796		10.0053	357.6	0.02798
	10.0026	358.7	0.02789		10.0026	357.9	0.02795
Backward	10.0036	355.74	0.02812		10.0036	355.9	0.02811
	10.0291	357.75	0.02803		10.0291	357.9	0.02802
	10.0313	358.7	0.02797		10.0313	358.8	0.02796
	10.0261	358.75	0.02795		10.0261	359.1	0.02792
	10.0296	359.74	0.02788		10.0296	359.1	0.02793
Forward	10.075	38.73	0.26013		10.075	38.9	0.25900
	9.961	38.52	0.25859		9.961	38.1	0.26144
	10.1382	38.96	0.26022		10.1382	39	0.25995
	10.0436	38.59	0.26026		10.0436	38.7	0.25952
	10.1256	38.76	0.26124		10.1256	39	0.25963
Backward	10.089	38.8	0.26003		10.089	39	0.25869
	10.3399	39.61	0.26104		10.3399	39.9	0.25915
	9.988	38.27	0.26099		9.988	38.2	0.26147
	10.175	38.8	0.26224		10.175	38.5	0.26429
	10.1611	39.06	0.26014		10.1611	39.3	0.25855
Forward	10.3198	4.38	2.35612		10.3198	4.3	2.39995
	10.2759	4.46	2.30401		10.2759	4.5	2.28353
	10.9159	4.64	2.35256		10.9159	4.5	2.42576
	10.1747	4.5	2.26104		10.1747	4.2	2.42255
	10.8153	4.55	2.37699		10.8153	4.7	2.30113
Backward	10.2151	4.54	2.25002		10.2151	4.3	2.37560
	11.0667	4.51	2.45381		11.0667	4.4	2.51516
	10.2147	4.47	2.28517		10.2147	4.4	2.32152
	9.3677	3.96	2.36558		9.3677	4	2.34193
	10.342	4.11	2.51630		10.342	4.4	2.35045

Table 8.2 – Standard Deviation of values from Table 8.2

	Forward	Backward	
Low Velocity			
Average	0,02800	0,02799	mm/s
Stand. deviation	0,00013	0,00007	(+/-) mm/s
	104,79	104,95	Hz
Frequency Range	105,28	105,22	Hz
	105,77	105,49	Hz
Normal Velocity			
Average	0,26000	0,26066	mm/s
Stand. deviation	0,00080	0,00159	(+/-) mm/s
	974,42	973,94	Hz
Frequency Range	977,44	979,92	Hz
	980,46	985,90	Hz
High Velocity			
Average	2,34836	2,37756	mm/s
Stand. deviation	0,05315	0,08207	(+/-) mm/s
	8628,62	8629,64	Hz
Frequency Range	8828,44	8938,18	Hz
	9028,26	9246,71	Hz

8.3 Annex C – Matlab® Code for LDV

In this annex is presented the matlab code done to data analysis.

```
clear all
close all
clc
filename='HS_filter_frt_3.txt';
M=importdata(filename);
X=M(:,1);
Y=M(:,2);
%time management
Fs = 1/(X(2));                  % Sampling frequency
T = 1/Fs;                       % Sample time
L = length(X);                  % Length of signal
t = (0:L-1)*T;                  % Time vector
%Signal plot
figure(1)
plot(t,Y)
title('Signal Corrupted with Zero-Mean Random Noise','interpreter','latex')
xlabel('time ($s$)','interpreter','latex')
ylabel('Voltage($V$)','interpreter','latex')
figureHandle = gcf;
set(findall(figureHandle,'type','text'),'fontSize',16,'fontWeight','bold')
%%
%Spectrogram
figure(2)
NFFT = 2^nextpow2(L/2); % Next power of 2 from length of y
Y1 = fft(Y,NFFT)/L;
f = Fs/2*linspace(0,1,NFFT/2+1);

% Plot single-sided amplitude spectrum.
Yfit=2*abs(Y1(1:NFFT/2+1));
[a b]=max(Yfit);
L1=length(Yfit);
Wfit=b+L1/2;
plot(f,Yfit)
title('Amplitude Spectrum of y(t)','interpreter','latex')
xlabel('Frequency $(Hz)$','interpreter','latex')
ylabel('$|Y(f)|$','interpreter','latex')
figureHandle = gcf;
set(findall(figureHandle,'type','text'),'fontSize',16,'fontWeight','bold')
%%
%Instant Frequency
xlen = length(Y);               % length of the signal
wlen = 1024;                    % window length (recomended to be power of 2)
h = wlen/4;                     % hop size (recomended to be power of 2)
nfft = 4096;            % number of fft points (recomended to be power of 2)

% define the coherent amplification of the window
K = sum(hamming(wlen,'periodic'))/wlen;
[s, f, t] = stft(Y, wlen, h, nfft, Fs);
s = abs(s)/wlen/K;

% correction of the DC & Nyquist component
if rem(nfft, 2)                     % odd nfft excludes Nyquist point
    st(2:end, :) = s(2:end, :).*2;
else                                % even nfft includes Nyquist point
    s(2:end-1, :) = s(2:end-1, :).*2;
end
```

```
% convert amplitude spectrum to dB (min = -120 dB)
s = 20*log10(s + 1e-6);

% plot the spectrogram
figure(3)
imagesc(t, f, s);
set(gca,'YDir','normal')
% set(gca, 'FontName', 'Times New Roman', 'FontSize', 14)
xlabel('Time, $s$','interpreter','latex')
ylabel('Frequency, $Hz$','interpreter','latex')
title('Amplitude spectrogram of the signal','interpreter','latex')
figureHandle = gcf;
set(findall(figureHandle,'type','text'),'fontSize',16,'fontWeight','bold')
handl = colorbar;
ylabel(handl, 'Magnitude, $dB$','interpreter','latex')

%plot with velocity
v=(f*532E-6)/2;
figure(4)
imagesc(t, v, s);
set(gca,'YDir','normal')
xlabel('Time, $s$','interpreter','latex')
ylabel('Velocity, $mm/s$','interpreter','latex')
title('Amplitude spectrogram of the signal','interpreter','latex')
figureHandle = gcf;
set(findall(figureHandle,'type','text'),'fontSize',16,'fontWeight','bold')
handl = colorbar;
ylabel(handl, 'Magnitude, $dB$','interpreter','latex')

%Matlab spectogram
figure(5)
spectrogram(Y,hamming(NFFT),NFFT/2,NFFT,Fs,'yaxis')
xlabel('Time, $s$','interpreter','latex')
ylabel('Frequency, $Hz$','interpreter','latex')
title('Amplitude spectrogram of the signal','interpreter','latex')
handl = colorbar;
ylabel(handl, 'Magnitude, $dB$','interpreter','latex')
figureHandle = gcf;
set(findall(figureHandle,'type','text'),'fontSize',16,'fontWeight','bold')
```

8.4 Annex D – Results from LDV

In this annex will be presented more results obtained from LDV for different velocities.

For High Speed

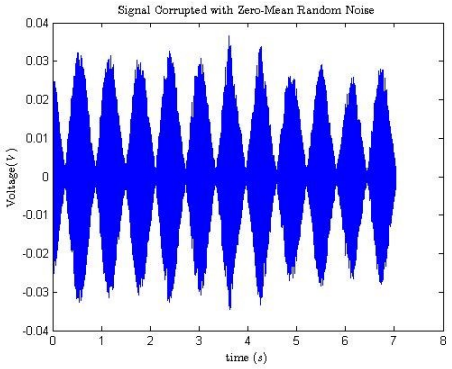

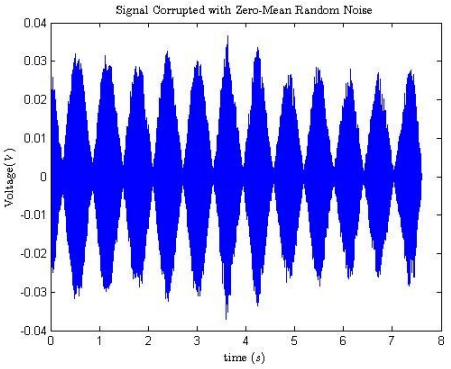

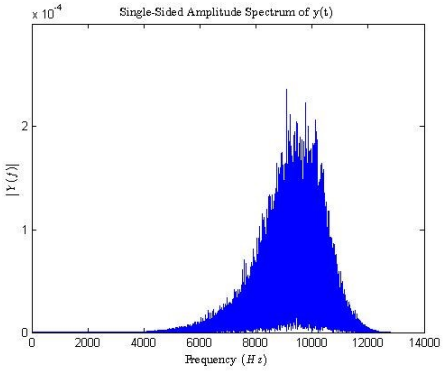

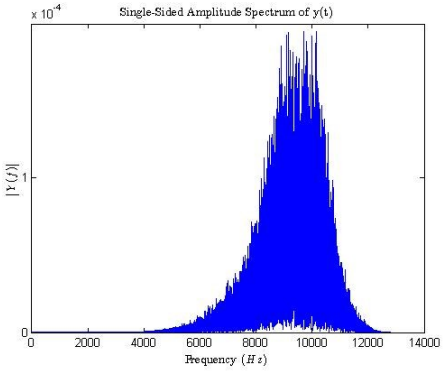

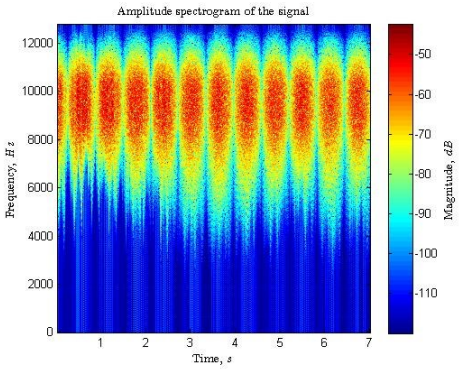

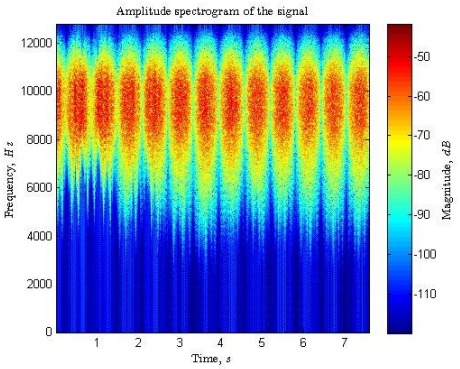

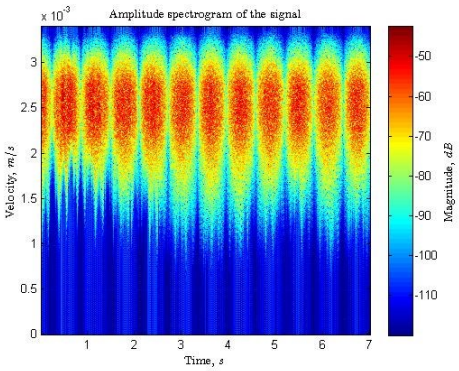

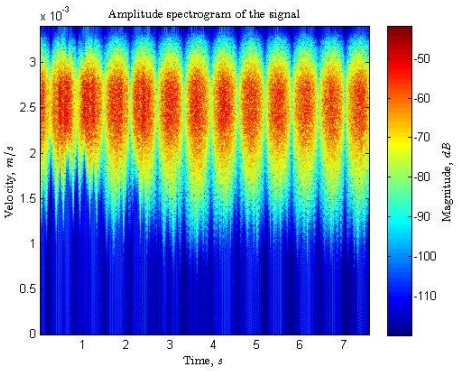

Normal Speed

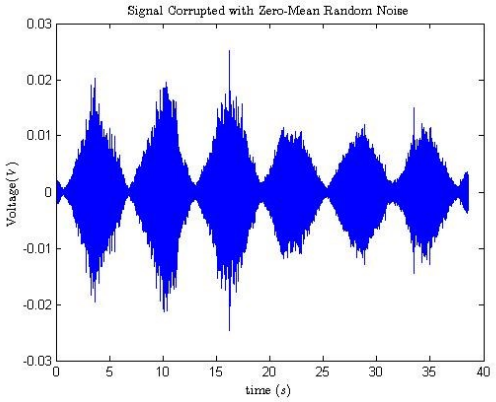

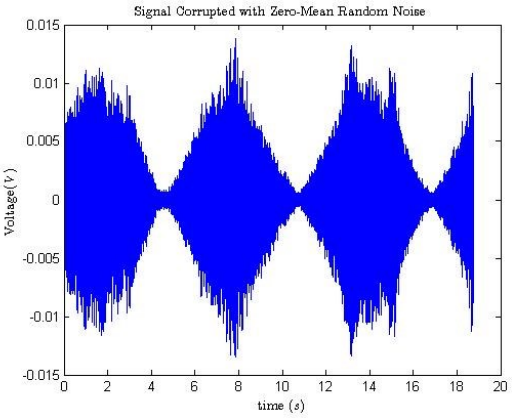

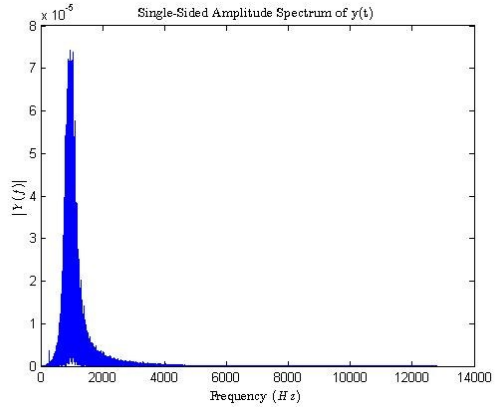

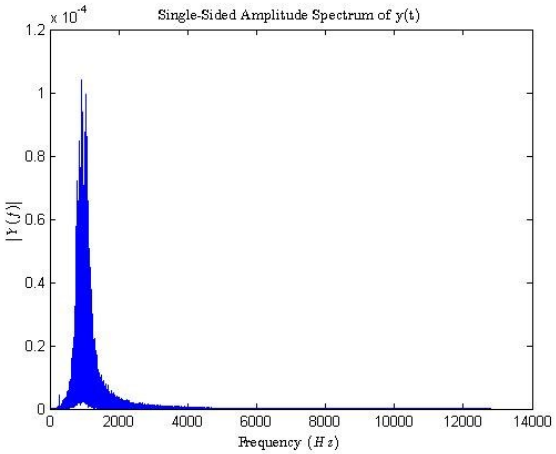

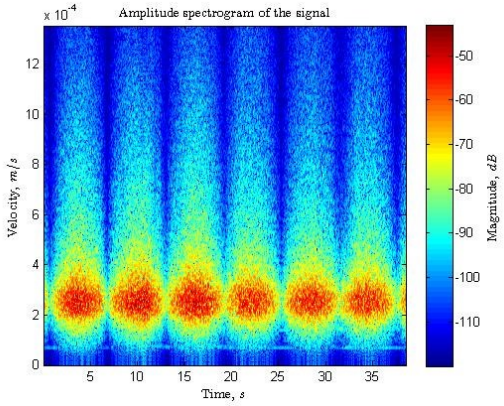

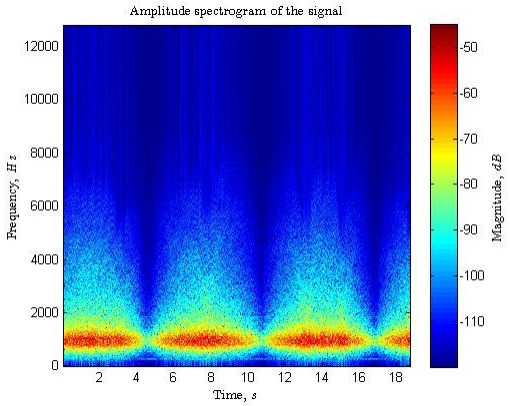

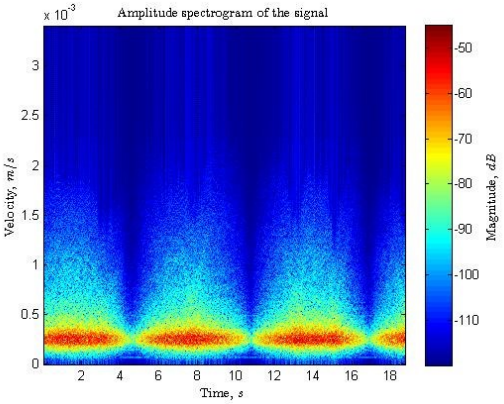

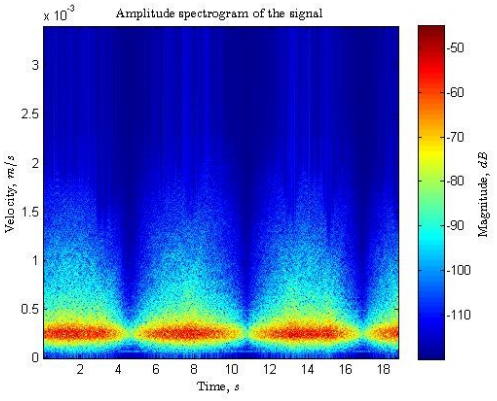

Low Speed

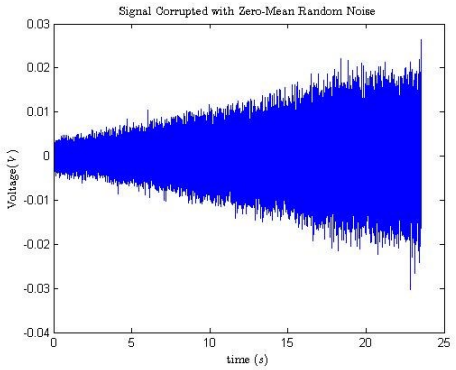
Signal Corrupted with Zero-Mean Random Noise
Voltage(v)
time (s)

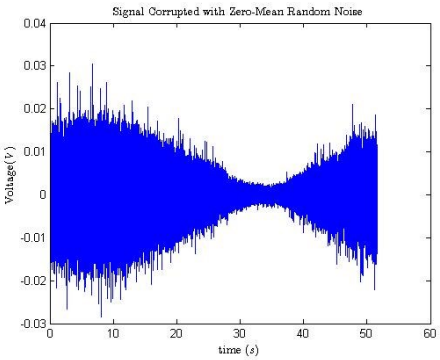
Signal Corrupted with Zero-Mean Random Noise
Voltage(v)
time (s)

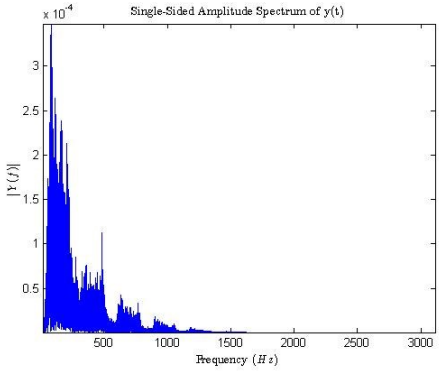
Single-Sided Amplitude Spectrum of y(t)
|Y(f)|
Frequency (Hz)

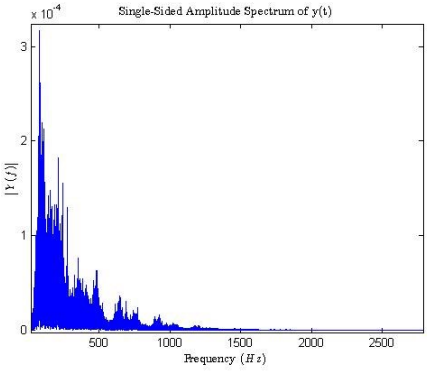
Single-Sided Amplitude Spectrum of y(t)
|Y(f)|
Frequency (Hz)

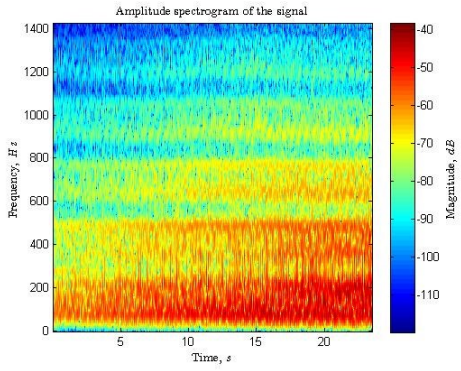
Amplitude spectrogram of the signal
Frequency, Hz
Time, s
Magnitude, dB

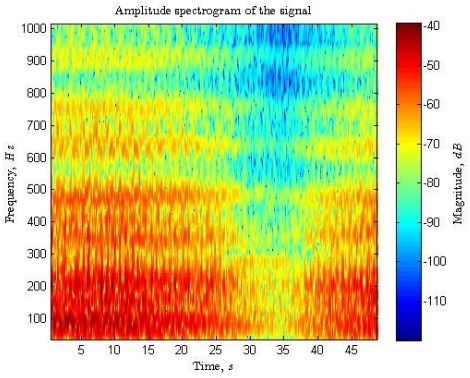
Amplitude spectrogram of the signal
Frequency, Hz
Time, s
Magnitude, dB

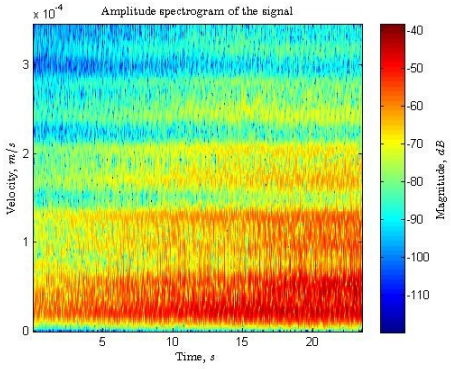
Amplitude spectrogram of the signal
Velocity, m/s
Time, s
Magnitude, dB

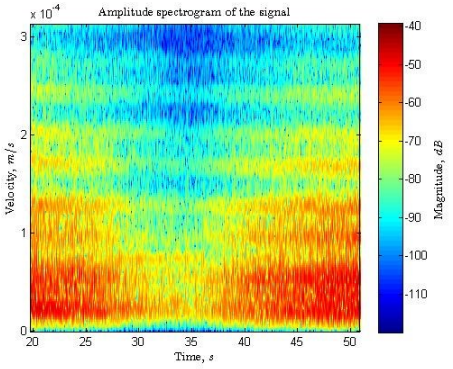
Amplitude spectrogram of the signal
Velocity, m/s
Time, s
Magnitude, dB

8.5 Annex E – Matlab ® code for PDV

```
clear all; clc;

[filename, pathname] = uigetfile('*.csv', 'Pick a csv-file');
if isequal(filename,0)
   return;
else
   File=fullfile(pathname, filename);
end
[pathstr, name, ext] = fileparts(File);

M = csvread(File,2,0);
t = M(:,1); V = M(:,2);
t = t.*2E-8;

Fs=2*10^abs(ceil(log10(t(2)-t(1))));
L=length(t);
Lsq=2^nextpow2(L); %Next power of 2 from lenght of time vector - 65536*4; %
f = Fs/2*linspace(0,1,Lsq/2+1);
plot(t,V);
% N = 12228;
TF=fft(V,Lsq)/L;
% ATF = fftshift(TF);
figure; plot(f,2*abs(TF(1:Lsq/2+1)));
xlabel('Freq (Hz)'); ylabel('|TF(f)|');
```

8.6 Annex F – Specifications from RIGOL

► Key Specifications

Model Number	DS6104	DS6102	DS6064	DS6062
Analog BW	1 GHz		600 MHz	
Channels	4	2	4	2
Max. Sample rate	5 GSa/s			
Max. Memory Depth	140 Mpts (Std.)			
Max. Waveform Capture rate	180,000 wfms/s			
Time Base Accuracy	≤ ±4 ppm			
Time Base Drift	≤ ±2 ppm/Year			
Timebase Scale	DS606X:1 ns/div to 1000 s/div			
	DS610X:500 ps/div to 1000 s/div			
Input Impedance	1MΩ,50 Ω			
Vertical Scale	2 mV/div to 5 V/div(1 MΩ)			
	2 mV/div to 1 V/div(50 Ω)			
DC Gain Accuracy	±2% full scale			
Bandwidth Limit	20 MHz or 250 MHz			
Real Time waveform Record, Replay and Analysis function	Max. 200,000 frames(Std.)			
Std, trigger functions	Edge,Pulse width,Slope,Video,HDTV,Pattern,			
	RS232/UART,I2C,SPI,CAN,USB,FlexRay			
Serial Bus decoding	RS232/UART,I2C,SPI,CAN,FlexRay			
Math functions	A+B,A-B,A×B,A/B,FFT,Advanced Math,Logic operation			
Auto Measurements	Vpp, Vamp, Vmax, Vmin, Vtop, Vbase, Vavg, Vrms, Overshoot, Preshoot, Area, Period Area,			
	Freq, Period, Rise Time, Fall Time, +Width, -Width, +Duty, -Duty, Delay A→B rising edge, Delay			
	A→B falling edge,Phase A→B rising edge,Phase A→B falling edge			
Connectivities	Dual USB HOST,USB DEVICE,LAN,VGA,10MHz Input/Output,			
	Aux Output(TrigOut, Quick Edge, PassFail, Calibration, GND)			
Display	10.1 inches (257 mm) TFT LCD display,800 Horizontal ×RGB×480 Vertical Pixel,			
	Multiple intensity grading			
Size (W×H×D)	399.0 mm× 255.3 mm×123.8 mm			
Weight	5.345 ± 0.2 kg (Without Package)			
Std. Probes	600MHz BW Passive Probe:4 sets for 4 channel models,2 sets for 2 channel models			
	1.5GHz BW Passive Probe:2 sets for DS6104,1 set for DS6102			

Figure 8.1 – Specifications from RIGOL DS6102

8.7 Annex G – Specifications from laser diode

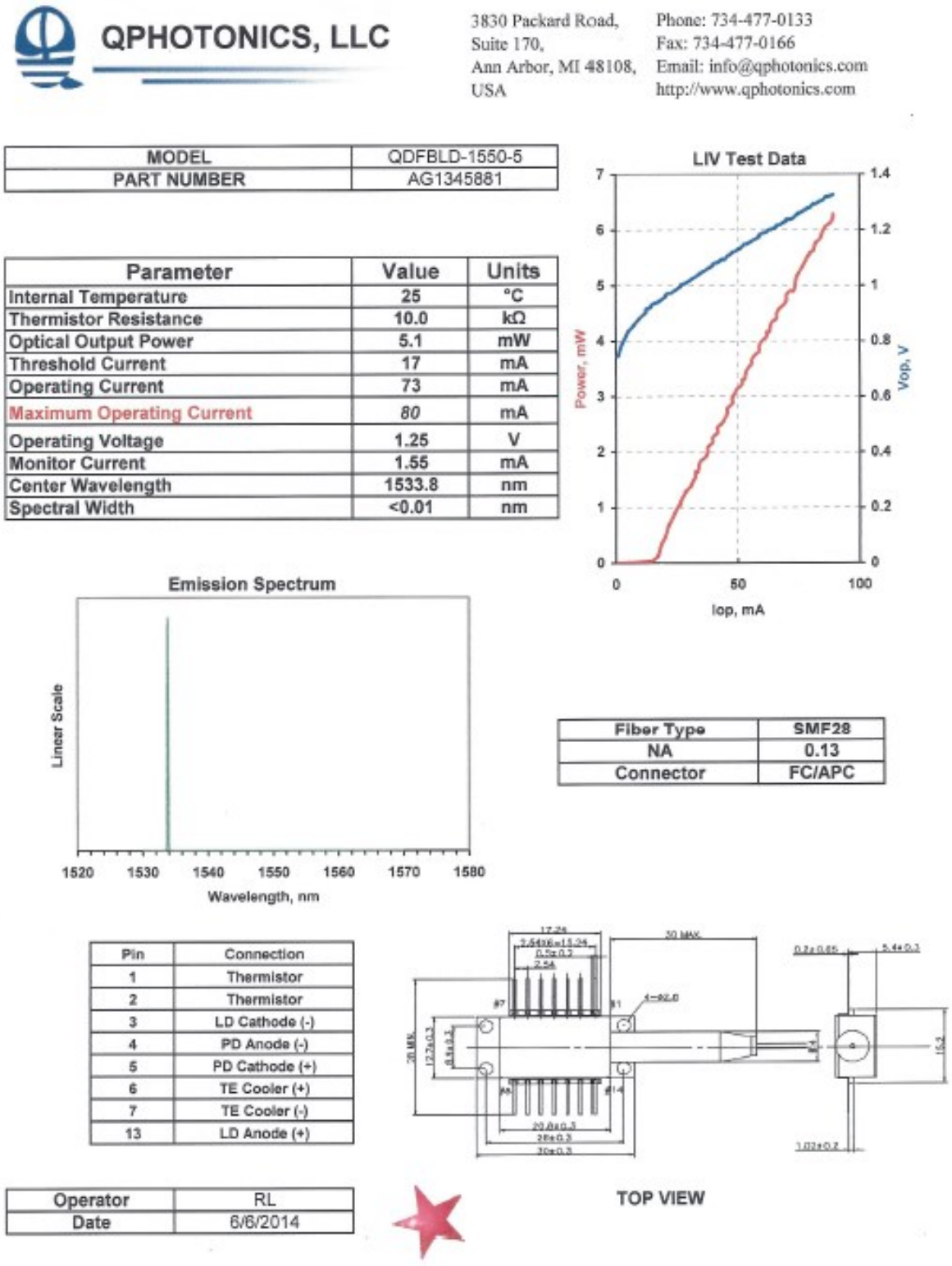

Figure 8.2 – Calibration sheet of the laser diode

Safety Instructions

Observe the following general safety instructions during all phases of operation of this instrument. Failure to comply with these instructions or with specific warnings elsewhere in this manual violates the safety standards of intended use of the instrument. QPhotonics assumes no liability for the customer's failure to comply with these requirements.

DO NOT SUBSTITUTE PARTS OR MODIFY INSTRUMENT

Do not install substitute parts or perform any unauthorized modification to the instrument. Return the instrument to QPhotonics for service and repair to ensure that all safety features are maintained.

KEEP AWAY FROM LASER BEAM

Semiconductor lasers emit infrared radiation that is invisible to the human eye. When in use, safety precautions should be taken to avoid the possibility of eye damage. Wear certified eye protection. Avoid direct exposure to beam. Do not stare directly at the laser connector or view an operating laser at close range. If viewing is required, the beam should only be observed by reflection from a matte surface utilizing an image converter or a suitable fluorescent screen.

SPECIFICATION	
Laser diode driver unit with temperature controller	
Maximum operating current, mA	300
Stability of current, better than, %	0.1
Maximum TEC current, A	1.5
Maximum TEC voltage, V	5
PD current range, mA	0.01-5
Supply voltage	110VAC/230VAC
Power consumption, W	< 40
Size, mm	225 x 165 x 40
Weight, lb	1.5

4. Pinout type 2

The included 14-Pin Butterfly mount is configured to work with laser diodes in 14-pin Butterfly package with pinout diagram as shown below.

Top View

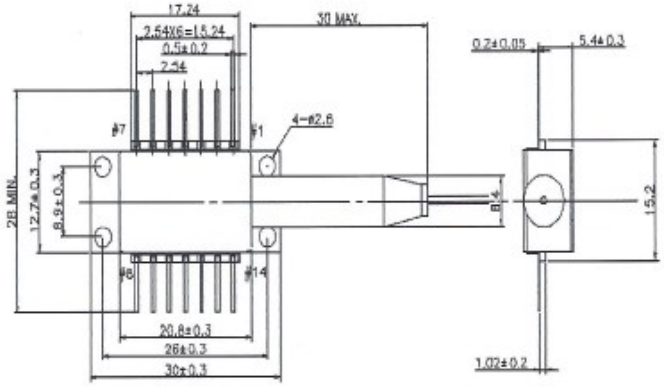

Pin	Connection
1	Thermistor
2	Thermistor
3	LD Cathode (-)
4	PD Anode (-)
5	PD Cathode (+)
6	TE Cooler (+)
7	TE Cooler (-)
13	LD Anode (+)

Pinout diagram for 14-pin Butterfly laser diode

The pin layout for DB9 type connector is as follows.

Pin	Connection
1	LD Cathode (-)
2	LD Anode (+)
3	TE Cooler (-)
4	TE Cooler (+)
5	Case
6	PD Anode (-)
7	Thermistor
8	Thermistor
9	PD Cathode (+)

Pin layout for DB9 type connector on QM14BTF 14-Pin Butterfly mount

8.8 Annex H – Specifications from detector

Electrical Specifications		
Detector		InGaAs PIN
Active Area Diameter		Ø80 um
Wavelength Range	λ	850 to 1700 nm
Peak Wavelength	λ_p	1550 nm
Peak Response[b]	$\Re(\lambda_p)$	0.90 A/W (Typ.)
Diode Capacitance	C_J	0.3 pF
Bandwidth (-3 dB)[b]		5 GHz
Rise Time (20/80%) @1538 nm		<70 ps
Rise Time (20/80%) @1538 nm		<70 ps
NEP (λ_p) @ 1550 nm		2×10^{-15} W/Hz$^{1/2}$
Recommended Maximum Output (50 Ω)[d]		1 V
After-Pulse Ringing		<20% of Maximum
Bias Voltage	V_R	12 V
Dark Current[b]	I_D	1.5 nA
Output Voltage	V_{OUT}	0 to 1 V (50 Ω)[c]
General		
Input		FC/PC Fiber Connector
Output		SMA (DC Coupled)
Package Size		2.21" x 1.40" x 0.80" (56.1 mm x 35.6 mm x 20.3 mm)
Ball Lens Diameter		0.059" (1.50 mm)
Ball Lens Clear Aperture		∅0.8 mm
Weight		0.18 kg
Storage Temp		0 to 40 °C
Operating Temp		0 to 40 °C
Battery		A23, 12 V_{DC}, 40 mAh
Replacement Battery		Energizer No. A23

6.1. Response Curve

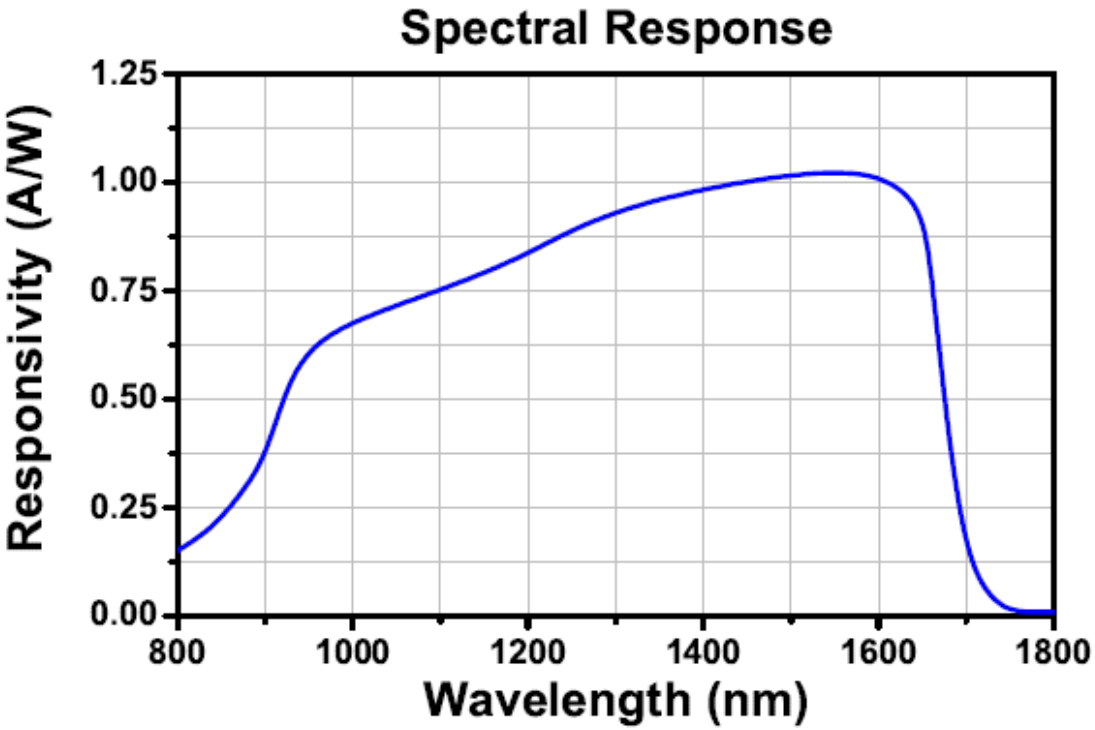

6.2. Typical Response

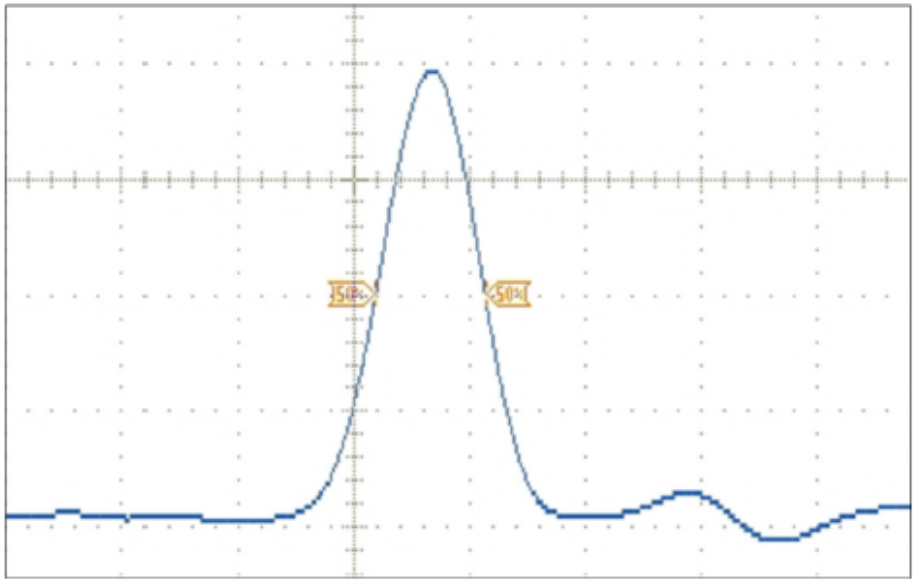

Figure 4 T_r = 55 ps, T_f = 52 ps@ 20/80%, T_p = 110 ps

6.3. Mechanical Drawing

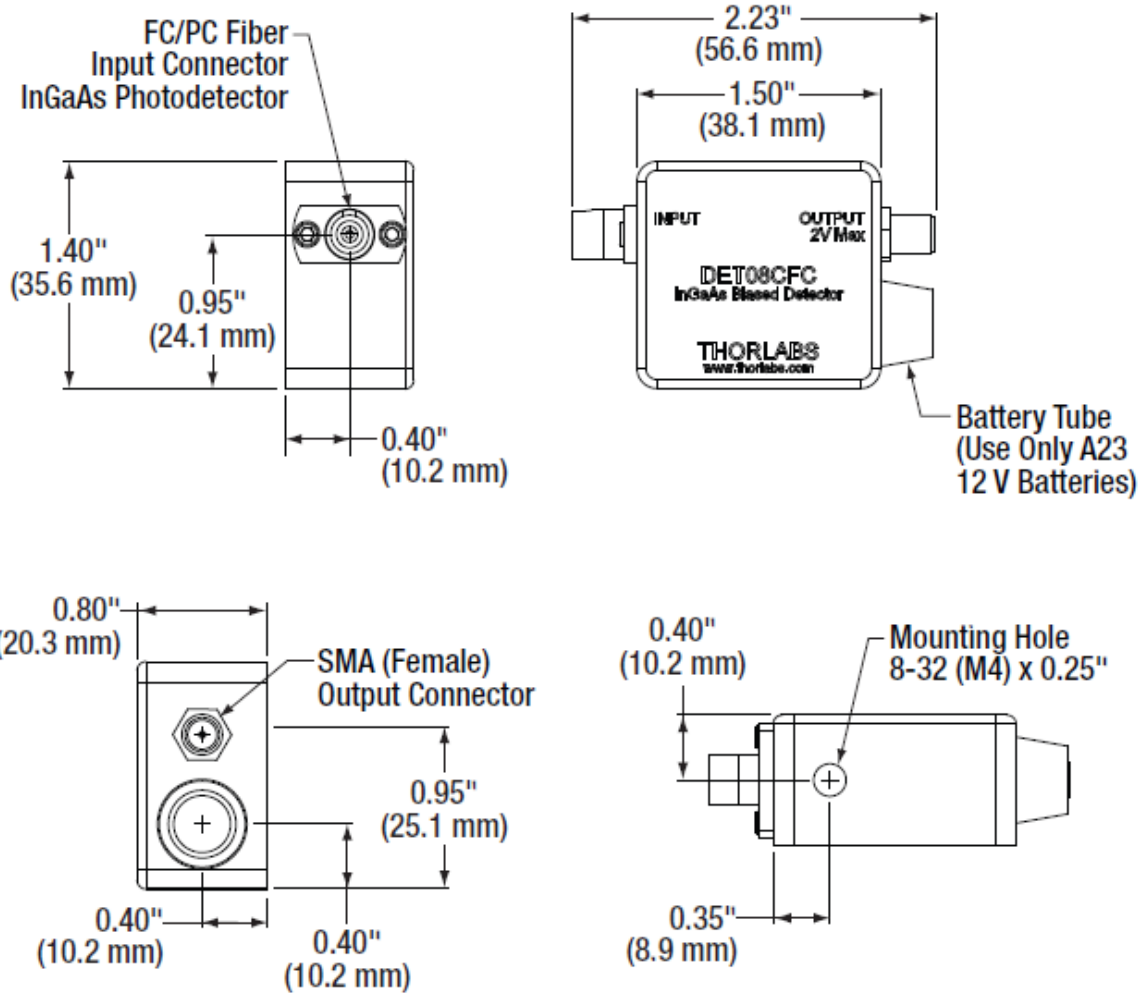

8.9 Annex I – Specifications from fiber optical components

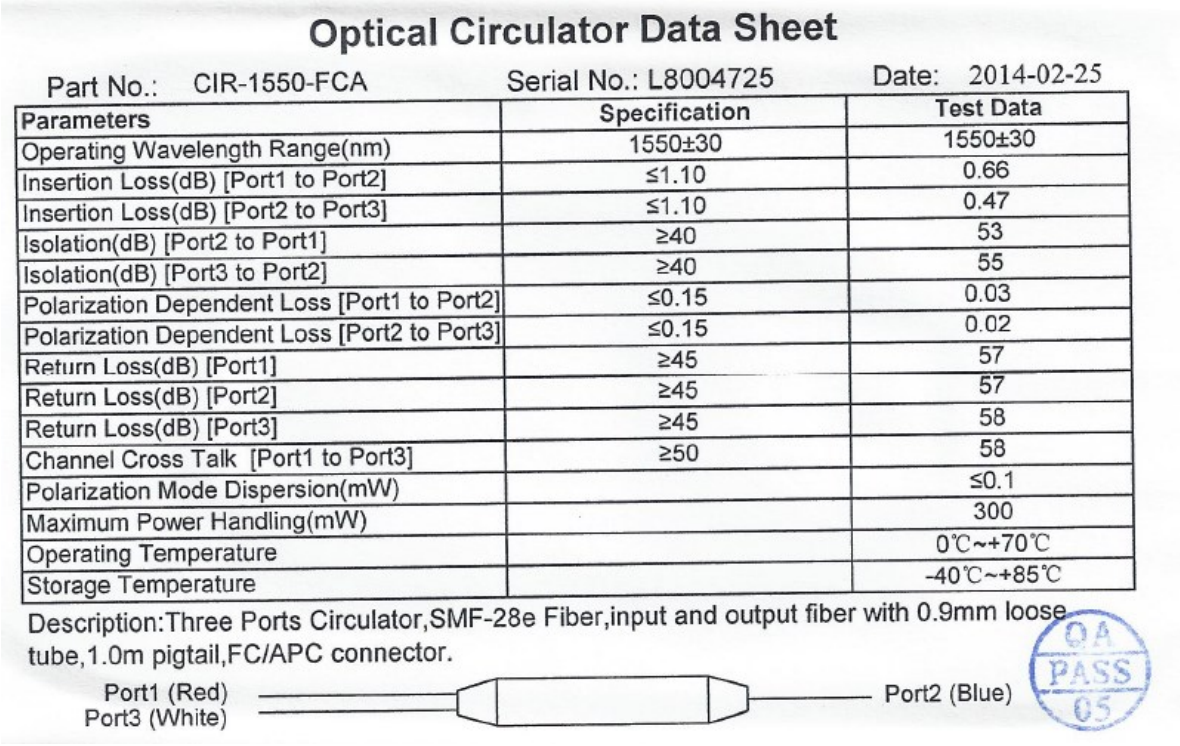

Optical Circulator Data Sheet

Part No.: CIR-1550-FCA Serial No.: L8004725 Date: 2014-02-25

Parameters	Specification	Test Data
Operating Wavelength Range(nm)	1550±30	1550±30
Insertion Loss(dB) [Port1 to Port2]	≤1.10	0.66
Insertion Loss(dB) [Port2 to Port3]	≤1.10	0.47
Isolation(dB) [Port2 to Port1]	≥40	53
Isolation(dB) [Port3 to Port2]	≥40	55
Polarization Dependent Loss [Port1 to Port2]	≤0.15	0.03
Polarization Dependent Loss [Port2 to Port3]	≤0.15	0.02
Return Loss(dB) [Port1]	≥45	57
Return Loss(dB) [Port2]	≥45	57
Return Loss(dB) [Port3]	≥45	58
Channel Cross Talk [Port1 to Port3]	≥50	58
Polarization Mode Dispersion(mW)		≤0.1
Maximum Power Handling(mW)		300
Operating Temperature		0℃~+70℃
Storage Temperature		-40℃~+85℃

Description:Three Ports Circulator,SMF-28e Fiber,input and output fiber with 0.9mm loose tube,1.0m pigtail,FC/APC connector.

Port1 (Red)
Port3 (White)

Port2 (Blue)

QA PASS 05

Figure 8.3 – Specifications of the Optical Circulator

timbercon

www.timbercon.com

20245 SW 95th Ave.
Tualatin. OR 97062

503.827.8141
800.221.6992

503.228.6747. fax
Info@timbercon.com

PRODUCT DESCRIPTION

9 SX RS 3mm FCAPC/LCAPC 1M

PART NUMBER

CA-905-044-084-001M

QUANTITY

1

Figure 8.4 – Specifications of the connector

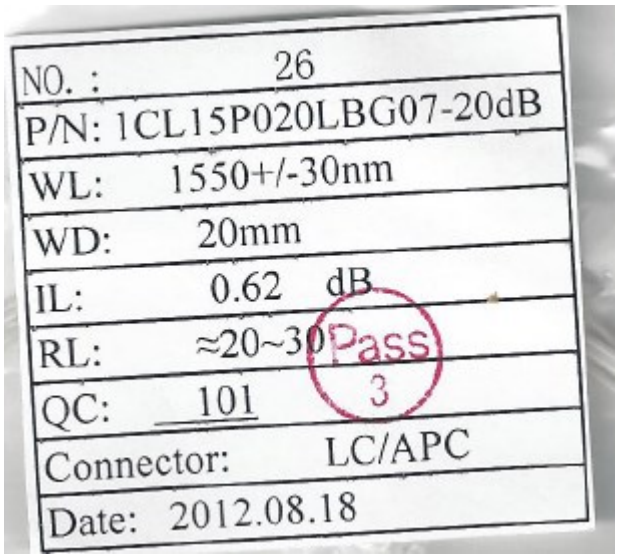

Figure 8.5 – Specifications of the probe

8.10 Annex J – Specifications from EDFA Module amplifier

2. Optical Specifications

Parameter	Value			Units	Note
	Min	Typ	Max		
Operation Wavelength	1540	1550	1565	nm	
Input Power	-10	0		dBm	
Saturated Output Power	+27	+27.5		dBm	For input power ≥ +7 dBm
Output Power Tunability	+17		+27.5	dBm	
Signal Gain	20			dB	For input power ≤ +7 dBm
Noise Figure		5.0	6.0	dB	For input power of +7 dBm, 1550 nm

3. Monitor Characteristics

Parameter	Value			Units / Notes
	Min	Typical	Max	
Pump Drive Current		3600		mA
Pump Temperature			70	ºC
Case Temperature		25	60	ºC
Input Power	-10	+7		dBm
Output Power	+14		+28	dBm

4. Electrical Specifications

Parameter	Value
Power Supply Input	4.75 – 5.25 VDC
DC Power Consumption	≤ 20 W

6. MECHANICAL SPECIFICATIONS

Parameter	Specifications	Units
Optical Input	0.8 meter long 0.9mm-jacket fiber cable with FC/APC termination	
Optical Output	0.8 meter long 0.9mm-jacket fiber cable with FC/APC termination	
Module Dimension	8 x 5.975 x 1.50	inch

EDFA Module Mechanical Drawing, in inch

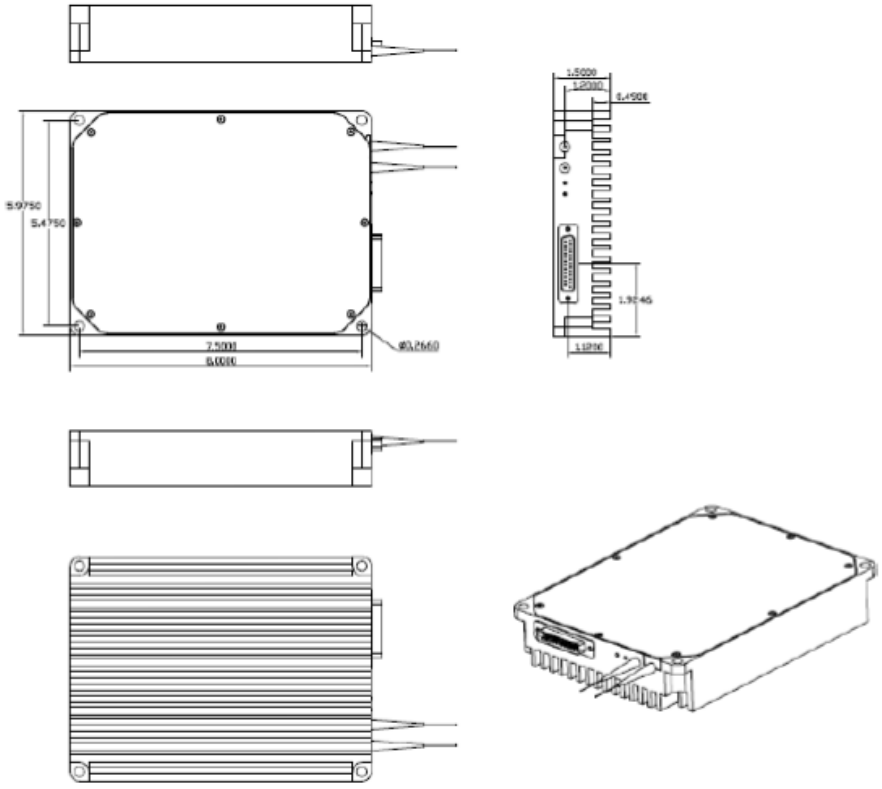

8.11 Annex K – LDV Prototype

In this annex are presented the different views of the Portable LVD protptype.